ΧΡΗΣΤΟΣ ΚΟΥΛΟΥΜΕΝΤΑΣ

Απεικόνιση δομών και διεργασιών του νηματοειδούς *C. elegans* με χρήση μη γραμμικής μικροσκοπίας

Μεταπτυχιακή Εργασία

Πανεπιστήμιο Κρήτης
Σχολή Θετικών Επιστημών
Τμήμα Φυσικής

Μεταπτυχιακό πρόγραμμα Μικροηλεκτρονικής – Οπτοηλεκτρονικής

Απεικόνιση δομών και διεργασιών του νηματοειδούς *C. elegans* με χρήση μη γραμμικής μικροσκοπίας

Χρήστος Κουλουμέντας

Μεταπτυχιακή Εργασία

Επιβλέπων: Καθ. Κ. Φωτάκης
Υπεύθυνος Εργασίας: Δρ. Γ. Φιλιππίδης

Ηράκλειο 2004

University of Crete
School of Sciences
Department of Physics

Postgraduate Course in Microelectronics and Optoelectronics

Imaging of structures and processes of the nematode *C. elegans* using nonlinear microscopy

Christos Kouloumentas

Master Thesis

Supervisor: Prof. C. Fotakis
Advisor: Dr. G. Filippidis

Heraklion 2004

Acknowledgements – Ευχαριστίες

Η εργασία αυτή είναι το αποτέλεσμα συνεργασίας πολλών ανθρώπων. Θα ήθελα αρχικά να ευχαριστήσω τον καθ. Κώστα Φωτάκη, πρόεδρο του Ι.Η.Δ.Λ. του Ι.Τ.Ε., ο οποίος με προέτρεψε να ασχοληθώ με τις βιοϊατρικές και βιολογικές εφαρμογές των Λέιζερ, μου παρείχε τη δυνατότητα να εργαστώ σε ένα άρτιο ερευνητικά περιβάλλον, και είχε τη γενικότερη επίβλεψη της εργασίας. Θα ήθελα επίσης να ευχαριστήσω τον Δρ. Θοδωρή Παπάζογλου, επικεφαλής του τμήματος βιοϊατρικών εφαρμογών του Ι.Η.Δ.Λ, για τη βοήθειά του στο σχεδιασμό και την οριοθέτηση των στόχων της εργασίας, καθώς και για τις πολύτιμες υποδείξεις του.

Ένα μεγάλο ευχαριστώ οφείλω στον Δρ. Νεκτάριο Ταβερναράκη, ερευνητή Γ' στο Ι.Μ.Β.Β. του Ι.Τ.Ε., καθώς έχει το συντονισμό της ερευνητικής προσπάθειας στα πλαίσια της οποίας εντάσσεται η παρούσα εργασία. Επιπλέον, θα ήθελα να ευχαριστήσω ιδιαίτερα τον συνεργάτη του, υποψήφιο διδάκτορα Γιάννη Βόγγλη, για τις πολύτιμες συμβουλές και διευκρινήσεις του, και για την βοήθεια που μου παρείχε στην επεξήγηση εννοιών και προβλημάτων της βιολογίας.

Ένα πολύ μεγάλο ευχαριστώ θέλω να πω στους άμεσους συνεργάτες μου, τον Δρ. Γιώργο Φιλιππίδη, τη Φωτεινή Ζαχαροπούλου και το Δημήτρη Καψοκαλύβα. Χωρίς την πολύτιμη καθοδήγηση του Γιώργου, ο οποίος ήταν και τυπικά ο υπεύθυνος της εργασίας μου, λίγα από αυτά που παρουσιάζονται θα είχαν επιτευχθεί. Ό,τι παρουσιάζεται είναι και δουλειά της Φωτεινής στα πλαίσια της διπλωματικής της εργασίας. Με το Δημήτρη συνεργαστήκαμε στο σχεδιασμό και την υλοποίηση των πειραμάτων που παρουσιάζονται στο παράρτημα της εργασίας. Θα ήθελα ακόμη να ευχαριστήσω το Γιώργο Βασιλάκη, πρώην μέλος του τμήματος βιοϊατρικών εφαρμογών, ο οποίος με βοήθησε να κάνω τα πρώτα μου πειραματικά βήματα στους χώρους του Ι.Τ.Ε.

Δεν πρέπει ακόμη να ξεχάσω τους καθηγητές και ερευνητές, οι οποίοι με μεγάλη προθυμία απαντούσαν στις ερωτήσεις μου και με καθοδηγούσαν βιβλιογραφικά κατά τη διάρκεια των πειραμάτων και της προετοιμασίας του κειμένου, και κυρίως τους Δημ. Χαραλαμπίδη, Νικ. Φλυτζάνη, Ιωαν. Κομίνη, Κων. Καλπούζο και Δημ. Παπάζογλου.

Τέλος, το πιο βαθύ και γλυκό ευχαριστώ θέλω να το πω στους γονείς μου για την ηθική και υλική υποστήριξη όλα αυτά τα χρόνια. Σας ευχαριστώ πολύ...

Χρήστος Κουλουμέντας

Abstract

Two-Photon Excited Fluorescence (TPEF) and Second-Harmonic Generation (SHG) are relatively new promising tools for the imaging of biological structures and processes at the microscopic level. The combination of the two contrast modes in a single instrument can provide unique and complementary information concerning the structure and the function of tissues and individual cells. In the present study a compact, inexpensive and reliable setup was developed for the simultaneous TPEF and SHG imaging of biological samples. By means of the developed setup, high-resolution mapping of the nematode *C. elegans* in both its anterior and posterior body part, was achieved. Numerous strains, expressing Green Fluorescent Protein (GFP) were investigated, and the two touch receptor neurons of the nematode at its posterior body part (PLM) were localized. Optimum conditions for the detection of the exogenous SHG signal, arising from the GFP molecules, attached to transmembrane proteins of the PLM neurons, were found. Plans for future work for monitoring the membrane potential of the PLM neurons by means of SHG measurements are described.

Περίληψη

Ο Διφωτονικά Διεγειρόμενος Φθορισμός (ΔΦΔΦ) και η Γέννεση Δεύτερης Αρμονικής (ΓΔΑ) είναι δύο νέα σχετικώς εργαλεία για την απεικόνιση σε μικροσκοπικό επίπεδο βιολογικών δομών και διαδικασιών. Ο συνδυασμός τους σε ένα κοινό απεικονιστικό σύστημα είναι δυνατόν να προσφέρει μοναδικές και, το σπουδαιότερο, συμπληρωματικές πληροφορίες σχετικά με τη δομή και τη λειτουργία ιστών, αλλά και μεμονομένων κυττάρων. Στα πλαίσια της παρούσας εργασίας αναπτύχθηκε μία εύχρηστη, αξιόπιστη και χαμηλού κόστους διάταξη για την ταυτόγχρονη απεικόνιση βιολογικών δειγμάτων, με χρήση των μη γραμμικών φαινομένων ΔΦΔΦ και ΓΔΑ. Χρησιμοποιώντας αυτήν τη διάταξη, επιτεύχθηκε η χαρτογράφηση του εμπρόσθιου και του οπίσθιου μέρους του νηματοειδούς *C. elegans*, με υψηλή διακριτική ικανότητα. Μελετήθηκαν πολλά γεννετικά μεταλλαγμένα είδη *C. elegans*, τα οποία εξέφραζαν σε διαφορετικά σημεία και με διαφορετικό τρόπο, μόρια της φθορίζουσας στο πράσινο πρωτεΐνης GFP. Επιτεύχθηκε, επιπλέον, ο εντοπισμός των δύο νευρώνων (PLM) στο οπίσθιο μέρος του νηματοειδούς που είναι υπεύθυνοι για την αντίδραση του ζώου σε μηχανικά ερεθίσματα. Μελετήθηκαν και βρέθηκαν οι ιδανικές πειραματικές συνθήκες για την ανίχνευση του εξωγενούς σήματος δεύτερης αρμονικής, προερχόμενου από τα μόρια της πρωτεΐνης GFP, τα οποία προσδένονται σε διαμεμβρανικές πρωτεΐνες των νευρώνων PLM. Στην παρούσα εργασία περιγράφονται ακόμη τα μελλοντικά μας σχέδια για την παρακολούθηση και την καταγραφή του ηλεκτρικού δυναμικού της μεμβράνης των συγκεκριμένων νευρώνων με μετρήσεις του σήματος δεύτερης αρμονικής.

Table of Contents

INTRODUCTION

The constant evolution of optical microscopy over the past century has been driven by the desire to improve the spatial resolution and image contrast with the goal to achieve a better characterization of smaller specimens. Numerous techniques such as confocal, dark-field, phase-contrast, Brewster angle and polarization microscopies have emerged as improvement of conventional optical microscopy. Being a pure imaging tool, conventional optical microscopy suffers from its low physical and chemical specificity. This can be remedied by combining it with spectroscopic techniques like fluorescence or Raman spectroscopy. In biology, such microscopes have been successfully applied to the study of a wide range of complex biological systems, with good spectral resolution. However their spatial resolution is restricted by the diffraction limit imposed by the wavelength of the probe light. Conventional microscopy also does not provide microscopic information about the real surface structure of the sample. Furthermore, it is insensitive to the polar organization of molecules in the surface layer, although this could be important. In biology, for example, it is interesting to know the polar orientation of molecules adsorbed on a membrane and its influence on the membrane physiology.

In this context, nonlinear optical measurements used in conjuction with microscopy observation have created new opportunities. Second-order nonlinear processes such as second-harmonic generation (SHG) or sum frequency generation (SFG), and third-order processes such as third-harmonic generation (THG), coherent anti-Stokes Raman scattering (CARS), and two-photon excited fluorescence (TPEF) have been used for the imaging and the understanding of biological systems and processes. *In our work images and results obtained by using the nonlinear processes of the TPEF and SHG will be presented*.

By far the most well known form of nonlinear microscopy is based on TPEF. It is a 3-D imaging technology, alternative to conventional confocal microscopy. It was firstly introduced by Denk, Webb and coworkers in 1990 [1], and since then has become a laboratory standard. The electronic transition of a fluorophore can be induced by the simultaneous absorption of two photons. These two photons, typically in the infrared spectral range, have energies approximately equal to half of the energetic difference between the ground and excited electronic states. Since the two-photon excitation probability is significantly less than the one-photon probability, two-photon excitation occurs with appreciable rates only in regions of high temporal and spatial photon concentration. The high spatial concentration of photons can be achieved by focusing the laser beam with a high

numerical aperture (NA) objective lens to a diffraction-limited focus. The high temporal concentration of photons is made possible by the availability of high peak power pulsing lasers, with pulse width of the order of hundreds of femtoseconds (10^{-15} sec). The most important feature of two-photon microscopy is its intrinsic depth discrimination. For one-photon excitation in a spatially uniform fluorescent sample, equal fluorescence intensities are generated from each z section above and below the focal plane assuming negligible attenuation of the laser beam. However, in the two-photon case almost the total fluorescence intensity comes from a $4\,\mu m$ thick region about the focal point for objectives with NA 0.8. Thus, 3-D images can be constructed as in confocal microscopy, but without a confocal pinhole. This depth discrimination effect of the two-photon excitation arises from the quadratic dependence of two-photon fluorescence upon the excitation photon flux, which decreases rapidly away from the focal plane. The ability to limit the region of excitation is very important, especially for biological specimen, since their photodamage is restricted only to the focal point. Since out-of-plane fluorophores are not excited, they are not subject to photobleaching. Moreover, TPEF microscopy exhibits an additional advantage. Two-photon excitation wavelengths are red-shifted to approximately twice the one-photon excitation wavelengths. The significantly lower absorption and scattering coefficients ensure deeper tissue penetration. Finally, the wide separation between the excitation and emission spectra ensures that the excitation light can be rejected without filtering out any of the fluorescence photons, resulting in sensitivity enhancement and better signal-to-noise ratio (SNR).

A lesser known form of nonlinear microscopy, SHG microscopy, was used several years prior to the invention of TPEF, based on the generation of second-harmonic light either from surfaces or from endogenous tissue structures such as rat-tail tendons. In SHG, light of the fundamental frequency ω is converted by the nonlinear material into light at exactly twice that frequency, 2ω. Because of difficulties in signal interpretations and because of its seemingly arcane utility, at least in biological imaging, SHG microscopy has gone by relatively unnoticed until very recently. The discovery that exogenous markers can lead to exceptionally high signal levels has been a leading cause for the revival of SHG microscopy. In particular, SHG markers, when properly designed and collectively organized, can produce signal levels easily comparable to those encounterd in standard TPEF microscopy. Apart from that, many intrinsic structures of biological systems produce strong SHG signal, so labeling with exogenous molecular probes is not always required. As will be shown in the following chapters, the spatial resolutions provided by SHG and TPEF microscopies are commensurate, meaning that the two contrast modes can be conveniently derived from the same setup.

Despite their similarities, TPEF and SHG are based on fundamentally different phenomena [2]. TPEF relies on nonlinear absorption, followed by fluorescence emission, and hence is not a coherent process. SHG, on the other hand, relies on nonlinear scattering, and hence is a coherent process. The consequences of this basic difference will be described in detail in the chapter presenting the theory of SHG. SHG alike TPEF exhibits intrinsic three-dimensionality and ability to section deep within a biological tissue, due to its nonlinear nature. It has a significant efficiency only at extremely high incident light intensities, and therefore arises only from a well-defined volume around the focal center of the incident light beam. Moreover, in SHG imaging technique, alike TPEF, the wavelength of the fundamental incident light lies in the IR spectum region, thus suffering less from scattering and absorption inside the biological samples and exhibiting large penetration depths. We already mentioned that an enabling aspect of TPEF microscopy is the dramatic reduction of "out of plane" photobleaching and phototoxicity, compared with the conventional fluorescence microscopy. However, these effects still occur "in the plane" of focus. By contrast in SHG microscopy, photodamage considerations do not intrinsically exist, since, as it was mentioned, SHG does not arise from an absorptive process. However, photobleaching usually acompanies SHG, if the incident beam produces simultaneously two-photon excitation of the chromophores in the sample. Due to their similarities and their differences, TPEF and SHG can be combined in a single microscope, and this combination can be very advantageous, since they provide complementary information about several biological systems, as it will be presented in the next chapters.

SHG is a second-order nonlinear phenomenon, and its strength is fully determined by the second-order susceptibility tensor $\chi^{(2)}$ of the nonlinear medium. This tensor is non-vanishing only for non-centrosymmetric media. Under this symmetry constraint it is obvious that SHG can be mainly produced from structures with high degree of orientation and organization but without inversion symmetry, such as crystalls or endogenous arrays of structural proteins in biological systems. It can be also produced from metal surfaces, where there is a huge change in the refractive indices, and generally from interfaces, where the symmetry breaks. Over the last two decades SHG has been widely used as a spectroscopic tool in a variety of interfacial studies, including liquid-solid, liquid-air and liquid-liquid interfaces [3]. Because of the interfacial specificity of the process, SHG is an ideal approach to the study of biophysics in model membranes [4,5], and the membrane physiology of living cells [6-8]. Particurarly, one of the innovative applications of the SHG phenomenon is its usage as a highly sensitive monitor of membrane potential [5-12,]. When a laser pulse is incident on a membrane, it

induces dipoles in the fluorescent molecules that are membrane bound via transmembrane proteins, making them candidates for SHG. Alterations in the membrane potential alter the magnitude of the induced dipoles, thus affecting the magnitude of the observed SHG signal. Green Fluorescent Protein (GFP) has been used as SHG probe in this way [8,12], since it undergoes large electron redistribution in the presence of light, and the resulted induced dipole is affected by the characteristics of the transmembrane potential. In our work GFP is used as SHG probe in *Caenorhabditis elegans* (*C. elegans*) in an effort to associate functional responses of the *C. elegans* with molecular processes.

The nematode *C. elegans* is characterized of optical transparency which makes it an ideal model for application of either optical microscopy or laser based techniques. It is the first animal to have its entire genome sequenced [13]. That facilitates the performance of genetic and molecular approaches to solve core biological problems. The *C. elegans* nervous system has been reconstructed with electron microscopy [14] and contains 302 neurons. Many of the neurons have been found to contribute to specific functions. The coordinated function of individual neurons leads to characteristic behavioral responses. A clear example is the six touch neurons circuit, which makes *C. elegans* capable of sensing mechanical stimuli and adjusting its behavior in order to avoid the stimuli source. Although systematic investigations have revealed important data about the neurons that participate in specific behaviors, in many cases the processes that take place at the molecular level have still to be elucidated. In order to understand the contribution of single molecules to the neuronal activity, scientists attempt to record the membrane currents under different conditions. In this line of investigation the core touch receptor molecules have been identified. However the possible alterations of the membrane current due to the function of these molecules have never been assayed in vivo. Such experiments have been performed in many organisms by using patch clamp techniques, but these conventional electrophysiological studies are very difficult in *C. elegans* because of its small size [15]. This has led scientists to access the individual neurons electrophysiologically by using other techniques, such as SHG sensitivity of membrane potential.

In the work presented in this thesis, we developed for the first time in our country a compact, inexpensive and reliable experimental apparatus for nonlinear optical microscopy utilizing *fs* pulses, and gathered valuable experience for future studies of biological systems using this innovative kind of microscopy. We used the nonlinear optical phenomena of TPEF and SHG for the detailed imaging of the nematode *C. elegans* in both its anterior and posterior body

parts, and we extracted valuable information about the structure and the morphology of the nematode *C. elegans*. We used exogenous labeling, and specifically the fluorophore GFP in order to obtain complementary information via TPEF scanning microscopy. For our studies we used a variety of strains, which express molecules of GFP in different structures of their body. We focused further our research on the posterior part of the worm, where the two of the six touch receptor neurons are located.

The manuscript is divided in two main parts. In the chapters of the first part the basic theory is presented, while in the chapters of the second part the results of the experimental work and the future plans are presented. The first part contains six chapters.

In *Chapter 1* we begin with a brief introduction to fluorescence and photophysics.

In *Chapter 2* we carry on with the presentation of the theory of TPEF. Basic magnitudes, like the two-photon fluorescence cross section (σ_{TPEF}), are introduced, and a constant comparison between the two-photon microscopy of tissues and the conventional linear confocal microscopy is made throughout the whole chapter. We briefly discuss the use of exogenous fluorophores for the study of biological systems, and the photodamage mechanisms in tissues.

In *Chapter 3* we present extensively the basic theory and the main applications of SHG in biophysical studies. First, SHG is examined at the molecular level. Second, SHG from an assembly of molecules is examined. This case is treated in detail, since it leads to radiative phenomena dramatically different from those encountered in fluorescence. Third, SHG originating from exogenous labels is discussed. Finally, SHG from endogenous tissue structures is presented.

In *Chapter 4* we present the structure and the special characteristics of the fluorophore GFP.

In *Chapter 5* we summarize the optical techniques used for monitoring membrane potential over the last 20 years, and we describe the ability of SHG of probing membrane potentials. Based on the structure of GFP molecule, described in *chapter 4*, we explain how GFP can serve as a sensitive membrane potential sensor, monitoring its SHG signal.

In *Chapter 6* a brief but necessary presentation of the nematode *C. elegans* follows, since it is the biological system under test throughout the whole work presented in this thesis. The long-term goals of the whole project as well as the aims of our work are specified in detail.

The second part of this thesis contains two chapters.

In *Chapter 7* the developed experimental facility for nonlinear imaging is analyzed. The laser system, the optical components including the microscope, the mechanical scanning system, as well as the software developed for the control of the scanning process, the data acquisition and the data processing are described in full detail. The results obtained by combined TPEF

and SHG microscopy are presented, and valuable information about the morphology of the worm *C. elegans* is analyzed.

In *Chapter 8*, finally, conclusions and plans for future work are discussed.

1. ABSORPTION AND FLUORESCENCE

Emission of light in the form of fluorescence often accompanies deactivation of an electronically excited species. Fluorescence is defined as the radiative transition between two electronic states of the same spin multiplicity. Most organic molecules have "paired" electrons in their ground state molecular orbital configuration. The spins are balanced (e.g. $s_1 = +\frac{1}{2}$ and $s_1 = -\frac{1}{2}$) and the spin multiplicity ($M_s = 1$) is singlet. Alternatively, inversion of the spin of the excited electron results in the two unpaired electrons having the same spin orientation. The spins are not balanced (e.g. $s_1 = +\frac{1}{2}$ and $s_1 = +\frac{1}{2}$), the spin multiplicity is 3, and a triplet state results. Most commonly, fluorescence refers to singlet-singlet transitions, especially the transition between the lowest excited state (S_1) and the ground state (S_0). Other types of less common fluorescence processes do occur, but we will focus on S_1-S_0 fluorescence which is by far the most common type.

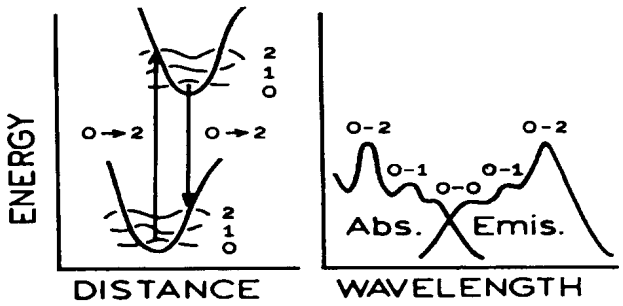

Figure 1.1 Potential energy diagram showing absorption and emission transitions between vibrational sublevels in ground end electronically excited states. Diagram showing the "mirror" image relationship around the wavelength of the 0–0 transition.

The absorption process involves interaction of the molecule in the ground state with a photon to promote an electron from a lower energy to a higher energy molecular orbital. The absorption process takes place on a time scale (~10^{-15} sec) much faster than that of molecular vibration. In the excited state the electron is promoted to an antibonding orbital such that the atoms in the bond are less tightly held, and the equilibrium bond length is subsequently longer. This is shown as a displacement to the right of the excited state potential curve with respect to the ground state in **Figure 1.1**. The vibrational level (in Figure 1.1, level 2) that is initially populated is that where vertical overlap at the energy of the absorbed photon occurs. For large molecules in condensed phases such as liquids and solids, fluorescence generally

occurs from the lowest vibrational level of the electronic excited state (level 0). That is due to the fact that vibrational deactivation, through intermolecular collisions, occurs more rapidly ($\sim 10^{-12}$ sec) than the fluorescence emission process ($\sim 10^{-8} - 10^{-9}$ sec).

The transition that is associated with the emission of a photon is also so rapid that no change in nuclear configuration can occur during the process. The vibrational level that is initially populated in the ground state (in Figure 1.1, level 2) will be again that which shows "vertical" overlap with the lower vibrational level of the S_1 state. Thus, the energy of the emitted photon will be significantly lower than the absorbed photon, and the fluorescence is red shifted with respect to the absorption. This red shift is termed Stokes shift. The energy level spacings between adjacent vibrational levels decreases with increasing energy, and a similar spacing of vibrational levels is often seen in the ground and the excited states. This results in the "mirror" image relationship around the energy of the 0–0 transition, commonly observed between absorption and emission spectra. The "mirror" image relationship is depicted in Figure 1.

2. DEACTIVATION OF THE S_1 STATE

Fluorescence is only one of the possible mechanisms by which an excited molecule can undergo to the ground state. The Jablonski diagram in **Figure 1.2** shows that there are a number of potential transitions open to the S_1 state after population by excitation and internal conversion from upper states. Before we describe these potential transitions, we briefly discuss the process of internal conversion. The energy separation between consecutive singlet levels ($S_0, S_1, \ldots, S_n$) tends to decrease with increasing electronic energy. Nonradiative transitions between upper states (S_n to S_{n-1}) occur rapidly to populate the lowest excited state, S_1. These types of transitions are denoted *internal conversion* as they occur between states of the same spin multiplicity. For this reason, the fluorescence emission spectrum is typically independent of the excitation wavelength. This is an example of *Kasha's generalization* that radiative processes or excited state reactions arise from the lowest electronically excited states (S_1 or T_1). According to the Jablonski diagram, now, the excited molecule can undergo both nonradiative and radiative (fluorescence) relaxation to the ground state (S_0) or nonradiative transition (*intersystem crossing*) to the lowest excited triplet state (T_1).

Intersystem crossing is defined as a nonradiative transition between states of different multiplicity (e.g. singlet-triplet) and results via inversion of the spin of the excited electron. Although intersystem crossing is formally forbidden due to selection rules, spin-orbit and vibronic coupling mechanisms makes it possible, but in any case less probable than fluorescence. Direct absorption into the triplet state from the ground state is spin forbidden, but the triplet excited state can be accessed indirectly through intersystem crossing from S_1 to T_1 state. The opposite transition from the excited triplet to the ground singlet is called phosphorescence and is also spin forbidden, hence it occurs very slowly with a radiative lifetime in the order of seconds or longer. By contrast, fluorescence lifetimes are of the order of nanoseconds. Phosphorescence can be observed only when the other de-activating processes have been suppressed, typically in rigid glasses, at low temperature and in the absence of oxygen.

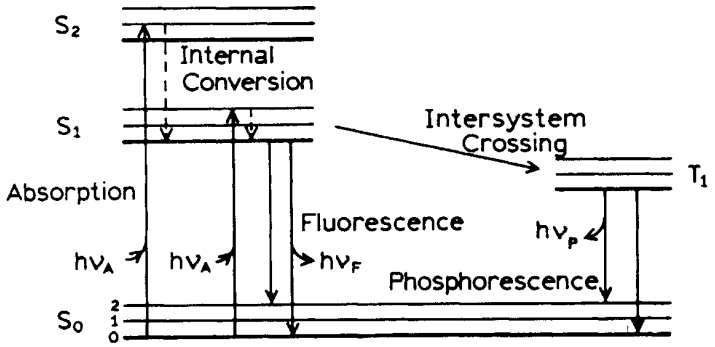

Figure 1.2 Modified Jablonski diagram showing radiative and nonradiative transitions between ground state (S_0) and excited singlet (S_1, S_2) and triplet (T_1) states.

Up to now only unimolecular processes have been discussed. Generally, the rate of a bimolecular process is limited by the rate at which molecules can diffuse together to react. Fluorescence quenching and energy transfer are two main bimolecular processes involving excited states. *Fluorescence quenching* can occur by a variety of mechanisms and introduces other avenues for deactivation of the excited singlet state. The simplest of these is straightforward quenching where the excited state energy is degraded as heat, when the excited fluorophore and specific quenchers (other molecules) are free to diffuse together and interact in a fluid environment. On the other hand, as *energy transfer* is referred the situation where the energy absorbed by one molecule is transferred to a second molecule that gives rise to an observed effect. Energy transfer can occur by different mechanisms. The first is a trivial radiative process, the second is the dipole or "Förster" energy transfer, and the third is the "electron exchange" energy transfer.

3. BASIC MAGNITUDES IN FLUORESCENCE THEORY

In **Box 1.1** some basic magnitudes and some useful relations, underlying the theory of the photon absorption and fluorescence are introduced.

BOX 1.1: **Basic magnitudes and useful relations**

According to the *Beer – Lambert law* the *molecular single photon absorption cross-section* σ_1 (cm^2) is given as:

$$\sigma_1 = \frac{\ln\left(\frac{I}{I_{out}}\right)}{nd} \tag{1.1}$$

where I the light intensity entering the sample, I_{out} the light intensity leaving it, n the number of molecules per volume (cm^{-3}), and d the sample path length (cm). The cross-section σ_1 is related with the single-photon absorption rate (W_1) through the relationship (I expressed as: $photons / \sec \cdot cm^2$):

$$W_1 = \sigma_1 \, I \tag{1.2}$$

The *quantum yield of fluorescence* Φ_f is defined as:

$$\Phi_f = \frac{\text{number of fluorescence emitted photons}}{\text{number of absorbed photons}} \tag{1.3}$$

The quantum yield of fluorescence can also be defined in terms of rate constants by:

$$\Phi_f = \frac{k_r}{\sum k} \tag{1.4}$$

where k_r is the radiative rate constant and $\sum k$ is the sum of the rate constants for all processes that depopulate the S_1 state.

The radiative lifetime, τ_r is defined by:

$$\tau_r = \frac{1}{k_r} \tag{1.5}$$

while the observed fluorescence lifetime τ_f by:

$$\tau_f = \frac{1}{k_f} = \frac{1}{\sum k} \tag{1.6}$$

Only in the unlikely absence of any competing deactivation channels would τ_r be identical to τ_f.

4. FLUORESCENCE IN BIOMOLECULES

Chromophores are components of molecules that have the potential to absorb light. They are generally aromatic rings, exhibit large potential for conjugation, and have at least one electron

donating group (–OH, $–NH_2$) attached to the aromatic ring. Electron withdrawing groups can diminish or destroy fluorescence.

The natural (intrinsic) fluorescence in biological macromolecules, usually proteins, is imparted by special residues. The most important of these residues are depicted in **Figure 1.3**. *Tryptophan*, *Tyrosine* and *Phenylalanine* are fluorescent aromatic amino-acids [16,17], they are hydrophobic and prefer to be buried in protein hydrophobic cores. *NADH* is the reduced form of nicotinamide adenine dinucleotide. The reduced nicotinamide ring is fluorescent [16]. Flavins are also fluorescent. *FAD* is the oxidized form of flavin adenine dinucleotide and is strongly fluorescent [18]. *Pyridoxal phosphate* (PLP) is a prosthetic group of transaminase and is a derivative of vitamin B_6. *Pyridoxamine phosphate* is an intermediate product, during the interaction of pyridoxal phosphate with α-keto acids in order to equilibrate amino groups among them. Both PLP and pyridoxamine phosphate are intrinsic chromophores.

Significant autofluorescence has also been noted in the structural proteins *collagen* [19] and *elastin* [20]. In both proteins, autofluorescence is associated with cross-links. Several mechanisms are employed in the formation of the cross-links, which contain fluorescent aromatic rings [19-23]. Finally, porphyrin is a small molecule (prosthetic group), that proteins like hemoglobin and myoglobin employ to carry out their functions. Due to its aromatic structure, porphyrin is also fluorescent in the red region of the optical spectrum.

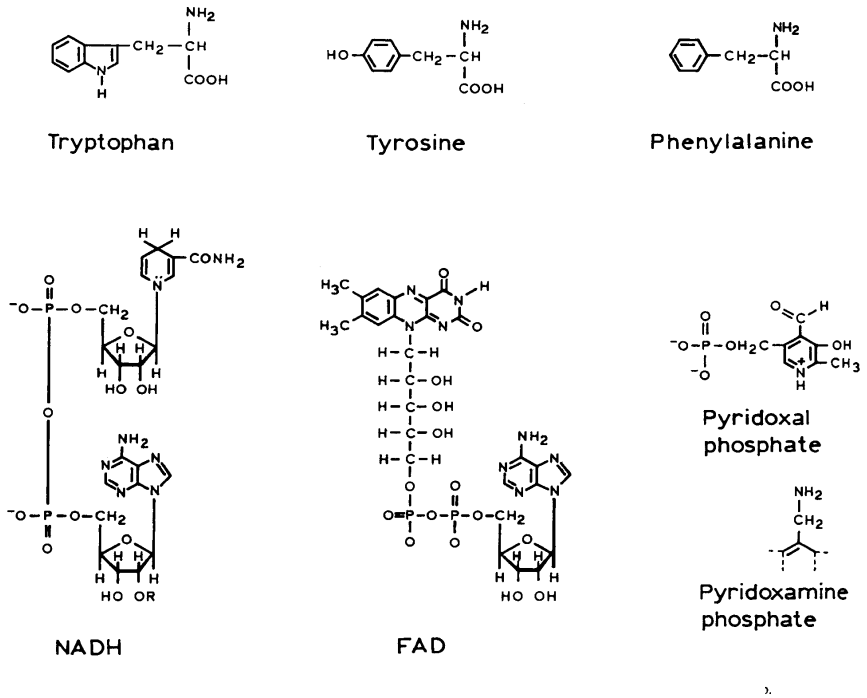

Figure 1.3 The chemical structures of the main intrinsic biochemical chromophores are depicted. In NADH, R is a hydrogen; in NAD(P)H, R is a phosphate group.

The intrinsic chromophores of proteins have not ideal properties for fluorescence measurements: low absorption coefficient, low quantum yield and short radiative lifetime. Hence in most biochemical studies, extrinsic fluorophores have to be added. The addition is realized either by means of chemical attachment of synthetic dyes like tetramethylrhodamine, or by means of genetically encoding as in the case of the Green Fluorescent Protein (GFP). In a following chapter the structure and the properties of GFP are presented analytically, since it plays a central role in our study.

5. MEASURABLE PROPERTIES OF FLUORESCENCE

In biochemical studies employing fluorescence, the properties that can be measured are usually the *fluorescence spectra*, the *fluorescence lifetime*, the *polarization of the fluorescent light*, the *excitation transfer* and the *location of fluorescence*. Each of these properties can obtain unique information about enviromental effects, orientation and dynamics of the fluorescent biomolecules. In our study, as far as fluorescence is concerned, even with the major difference that it is about two-photon excited fluorescence (TPEF), the main goal is the localization of the fluorescent (genetically encoded) GFP molecules within the biological system under investigation (*C. elegans)*. For this reason scanning microscopy techniques are used. In the next chapter, the basic theory of TPEF and the basic principles of TPEF scanning microscopy are presented.

1. TWO-PHOTON ABSORPTION

In *chapter 1* the basic principles of absorption and fluorescence were presented. The process of absorption, in its simplest form, enables the absorption of a single photon from the molecule in the ground state in order to promote an electron to a higher energy molecular orbital. Apart from this simple form of absorption, quite more complicated exist, enabling more photons with lower energy. Absorption in these cases involves interaction of the molecule in the ground state with more photons to promote again an electron to a higher energy molecular orbital. The transition to the final excited state may involve the participation of intermediate real excited states, and then it is referred to as "*Multiple-Photon Absorption*". The total transition is a multi-step process, and each step involves the independent absorption of a single photon, thus it is a resonant absorption. The molecule absorbs a photon, populates an excited state, and before the transition (radiative or nonradiative) to the ground state occurs, the molecule absorbs a second photon populating a higher excited state, and so on.

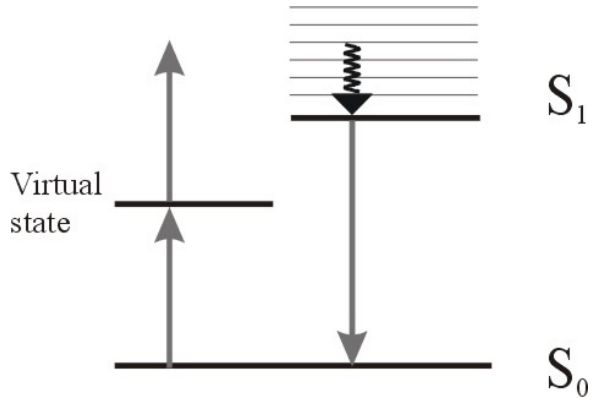

Figure 2.1 Potential energy diagram showing two-photon absorption through a virtual state. The molecule populates the first excited state, and undergoes normally to the ground state as in the case of the single-photon absorption.

On the other hand, the transition from the ground to the final state may involve the participation of intermediate virtual states, if the absorption of a single photon is not resonant, i.e. if the energy of the absorbed photon does not coincide with the energy difference of two energy states. The total transition includes a series of virtual transitions, each occurring with a violation of energy conservation, and then it is referred as "*Multi-Photon Absorption*". The case of special interest for biophysical studies and for this work specifically is when the final state of the transition is the first excited state S_1. In this case there are clearly no intermediate real states, and the absorption involving more photons and resulting to this transition is without question a multi-photon absorption. In **Figure 2.1** the Jablonski diagram of two-

photon excitation is depicted. The total transition of the molecule to the first excited state is realized via the absorption of two photons and involves the participation of one virtual state. Three-photon absorption would be realized via the absorption of three photons, and two virtual states would be involved. However, in the work presented here, two-photon absorption is used, and the generalization to the multi-photon case is made only for the best understanding of the two-photon absorption process.

In a virtual transition, the lifetime of the electron in the intermediate state τ_v is determined not by conventional relaxation mechanisms, but rather by the uncertainty principle connecting time and energy, $\Delta E \cdot \Delta\tau \sim \hbar$. The uncertainty in the energy of the virtual state can be taken as the detuning Δ from the nearest allowed resonance, $\Delta = \hbar(\omega_{10} - \omega)$, where $\hbar\omega_{10}$ is the energy difference between the ground and the state S_1. For a typical detuning of 1eV, the lifetime of the virtual state is expected to be about 0.5 fs. As the detuning from resonance Δ, approaches the natural width of the state Γ, virtual transitions become real transitions. In order for the electron to be able to be promoted from a virtual intermediate state to one of higher energy, the next photon (the second, in two-photon absorption) must be absorbed within the very short lifetime of the virtual state. Therefore, such a process requires a very large photon density, and is observed only at very high light intensity.

The concept of multi-photon excitation, proceeding as a series of single-photon transitions through virtual states can be used to provide order of magnitude estimates of the N-photon cross-section. In **Box 2.1** the derivation of the "Two-photon absorption cross-section", σ_2 is presented [24].

BOX 2.1: **Derivation of the "Two-photon absorption cross-section"**

As it was mentioned in *chapter 1*, the single photon absorption rate is given by:

$$W_1 = \sigma_1 I \tag{2.1}$$

For a resonant transition, the single photon absorption cross-section is of the order of $10^{-17}\ cm^2$ for many molecules of biological interest. A second photon can be absorbed from a single molecule, only if it is incident within the lifetime of the state. The lifetime of a virtual state, τ_v is determined by the detuning of the state. Therefore, τ_v is of the order of the photon period:

$$\tau_v \sim \frac{2\pi}{\omega} \tag{2.2}$$

which is of the order of 1 fs. The rate of absorption out of the virtual state is again $W_1 = \sigma_1 I$, so that the combined rate for the absorption of two-photons W_2, is given by:

$$2 -$$

Thus, defining a two-photon absorption cross-section, σ_2 ($cm^4 \cdot \text{sec}/\ photon \cdot molecule$) such that:

$$W_2 = \frac{1}{2}\sigma_2 I^2 \tag{2.4}$$

and combining eq. (2.3) and (2.4) the following estimation is obtained:

$$\sigma_2 \sim \frac{4\pi}{\omega}\sigma_1^2 \sim 10^{-49}\ \ cm^4 \cdot \text{sec}/\ photon \cdot molecule \tag{2.5}$$

The value obtained from this crude estimation is in rather good agreement with both theoretical and experimental data, since for common chromophores with excitation wavelength ranging from 690 nm to 1050 nm, σ_2 is about 10^{-48} to 10^{-50} $cm^4 \cdot \text{sec}/\ photon \cdot molecule$ [25].

In the introduction, it was already mentioned that two-photon absorption, as well as second-harmonic generation (SHG) is a nonlinear phenomenon. Moreover, it was mentioned that the strength of SHG is fully determined by the second-order susceptibility tensor $\chi^{(2)}$ of the nonlinear medium. On the contrary, two-photon absorption is related with the third-order susceptibility tensor $\chi^{(3)}$ of the nonlinear medium. In **Box 2.2** a series of calculations relating the two-photon absorption cross-section, σ_2, with the term $\chi^{(3)}$, is presented [26].

BOX 2.2: **Relating σ_2 to $\chi^{(3)}$**

Suppose that an optical field with real amplitude E and a single frequency ω is incident to a nonlinear material. Macroscopically, the optical response of the material to the incident light, or generally electromagnetic radiation, is characterized by the optically induced polarization density, P, which can also be expanded in a Taylor's series about $E = 0$:

$$P = \chi^{(1)} * E + \chi^{(2)} * E * E + \chi^{(3)} * E * E * E + \ldots \tag{2.6}$$

Eq. (2.6) can be rewritten as:

$$P = \chi * E \ \text{ where } \chi = \chi^{(1)} + \chi^{(2)} * E + \chi^{(3)} * E * E + \ldots \tag{2.7}$$

The tensor χ is referred to as the susceptibility tensor. The index of refraction n is related with χ as:

$$n^2 = \frac{k^2 c^2}{\omega^2} = 1 + 4\pi\chi \tag{2.8}$$

Using the definition $n^2 = \varepsilon = \eta + i\kappa$, where ε is the complex dielectric constant, allows the real and imaginary parts of the refraction index to be expressed in terms of the real and imaginary parts of χ. Thus:

$$\eta^2 - \kappa^2 = 1 + 4\pi\,\text{Re}\left\{\chi^{(1)} + \chi^{(3)} * E * E + \ldots\right\} \tag{2.9}$$

and

$$2\eta\kappa = 1 + 4\pi\,\text{Im}\left\{\chi^{(1)} + \chi^{(3)} * E * E + \ldots\right\} \tag{2.10}$$

Even terms in $\chi^{(n)}$ make no contribution for uniform excitation in an isotropic medium due to inversion symmetry. Several constraints are applied now to eq. (2.9) and (2.10). First, it is assumed that no single-photon absorption can occur, because the incident photons have no enough energy, since they lie in the near infrared region (NIR). This allows the imaginary part of $\chi^{(1)}$ to be set equal to zero. Second $\text{Re}\left\{\chi^{(1)}\right\} >> \text{Re}\left\{\chi^{(3)}\right\}$ ensuring that the real refractive index η effectively is a constant at its single photon value. This condition removes intensity-dependent components from the refractive index [27].

Eq. (2.10) now becomes:

$$\kappa = \frac{4\pi^2 I' \operatorname{Im}\left\{\chi^{(3)}\right\}}{\eta^2 c} \tag{2.11}$$

where $I' = \frac{c\eta E^2}{2\pi}$ is the radiation intensity at ω, expressed this time not as photon flux, hence $I' = I \cdot \hbar\omega$.

The absorption coefficient K for the intensity is defined by $\frac{dI'}{dz} = -KI'$ and is given in terms of κ as:

$$K = \frac{2\omega}{c}\kappa = \frac{8\pi^2 \omega I'}{\eta^2 c^2} \operatorname{Im}\left\{\chi^{(3)}\right\} \tag{2.12}$$

The absorption coefficient is related with the two-photon absorption cross-section σ_2 through a magnitude called two-photon absorption coefficient, denoted as β. The latter is normally defined using the relation:

$$\frac{dI'}{dz} = -\left(\alpha + \beta I'\right) I' \tag{2.13}$$

which is usually used for gas samples, but it can be also used for chromophores of biological interest. It is obvious that since single-photon absorption is negligible, $\beta = \frac{K}{I'}$. Combination of eq. (2.12) and (2.13), allows β to be expressed as:

$$\beta = \frac{8\pi^2 \omega}{\eta^2 c^2} \operatorname{Im}\left\{\chi^{(3)}\right\} \tag{2.14}$$

The relationship between β and σ_2 is given by:

$$\beta = 2N \frac{\sigma^{(2)}}{\hbar\omega} \tag{2.15}$$

where N represents the molecular number density, and the factor 2 arises from the absorption of two photons. Combining eq. (2.14) and (2.15) and neglecting N in order to express σ_2 in $cm^4 \cdot \sec/\, photon \cdot molecule$ the following relation between σ_2 and $\chi^{(3)}$ arises [28]:

$$\sigma_2 = \frac{4\pi^2 \hbar\omega^2}{\eta^2 c^2} \operatorname{Im}\left\{\chi^{(3)}\right\} \tag{2.16}$$

Eq. (2.16) serves as the basis for determining the value of two-photon absorption cross-section of a single molecule through measurements of the third-order optical susceptibility of a collection of such molecules [26].

Historically, two-photon absorption has been used and is still used in spectroscopy to probe excited states that cannot be reached by single-photon absorption. In molecules with center of symmetry, the electronic states can be divided into gerade (*g*) and ungerade (*u*) states. Single-photon transitions from *g* to *g* or from *u* to *u* are forbidden due to parity restrictions, but two-photon transitions are allowed [29]. However, the chromophores concerned in this work, and generally chromophores of biological interest, are in their great majority molecules with no center of symmetry, thus the parity restrictions can be relaxed. In this sense, the same excited states of the molecules can be reached, regardless of the excitation mode, and the simple

diagram depicted in Figure 2.1 is reasonable. Going further, it seems reasonable to expect that the excitation spectra of single-photon and two-photon absorption will be almost identical in shape, if the values of the excitation wavelength are multiplied by a factor of two. This assumption proves to be real for many chromophores without a center of symmetry (Cascade Blue, Coumarin 307, Lucifer Yellow, Indo-1) [25]. However, despite the obvious similarities, one general property observed in all measured two-photon absorption spectra is that the peak wavelengths of these spectra appear blue-shifted and never red-shifted relative to twice the single-photon absorption peak wavelengths [25]. One explanation is that some higher excited singlet states are reached with greater propability by two-photon than by single-photon absorption. Thus, parity restrictions, even relaxed, imply much larger two-photon absorption cross-sections at the blue shifted wavelengths than at twice the single-photon peak wavelengths.

Both one-photon and two-photon absorption cross-sections, σ_1 and σ_2 respectively, depend on the polarization of the incident photons. However, when a fluid or generally a collection of randomly oriented molecules is considered, an important difference between single-photon and two-photon absorption arises. In this case, σ_1 and σ_2 must be averaged over all orientations of the molecule to obtain $\langle\sigma_1\rangle$ and $\langle\sigma_2\rangle$, the absorption cross-sections of the sample. Using some simple considerations, it appears in **Box 2.3** that for all polarizations of the incident photons (linear, circular or elliptical), the single-photon absorption is independent of polarization, whereas the two-photon absorption is dependent. The following description of the polarization dependence is brief and the interested reader is referred to [30,31] for a more complete analysis.

BOX 2.3: **Polarization dependence**

The single-photon absorption cross-section σ_1 is proportional to the quantity $\left|\vec{\lambda}\cdot\vec{P}^{if}\right|^2$, where $\vec{\lambda}$ is the polarization vector of the absorbed photon and $\vec{P}^{if}$ is the *transition vector* between the initial state $\langle i|$ and the final state $|f\rangle$. Its components P_a^{if} are given by $\langle i|p_a|f\rangle$, where p_a is the operator for total momentum in the a direction. When the absorption of randomly oriented molecules is considered, σ_1 must be averaged over all orientation of the molecule. The result is $\langle\sigma_1\rangle \sim \frac{1}{3}\left(\vec{\lambda}\cdot\vec{\lambda}^*\right)\left(\vec{P}^{if}\cdot\vec{P}^{if*}\right)$, and since $\vec{\lambda}\cdot\vec{\lambda}^* = 1$ for all polarizations (linear, circular or elliptical) the sample absorption is independent of polarization.

In two-photon absorption σ_2 is proportional to $\left|\vec{\lambda}\cdot\overline{S}^{if}\cdot\vec{\mu}\right|^2$, where $\vec{\lambda}$ and $\vec{\mu}$ are the polarization vectors of the two absorbed photons and $\overline{S}^{if}$ is the two-photon *transition tensor* between the states $\langle i|$ and $|f\rangle$ [31].

It may be considered as a 3×3 matrix with components $S_{\alpha\beta}^{if}$. Again when the two-photon transition of a sample containing randomly oriented molecules, is considered, σ_2 must be averaged over all orientations to yield $\langle\sigma_2\rangle$. However, this time the polarization dependence does not vanish and as it is showed [30], the following proportionality applies: $\langle\sigma_2\rangle \sim \delta_F F + \delta_G G + \delta_H H$, where δ_F, δ_G and δ_H are molecular parameters independent of polarization, and F, G and H are simple algebraic functions dependent only on the polarization vectors $\vec{\lambda}$ and $\vec{\mu}$.

2. TWO-PHOTON EXCITED FLUORESCENCE (TPEF)

Once an excited state has been populated through two-photon absorption, a process of deactivation follows with the same characteristics as the one-photon excited fluorescence process (OPEF), described in *chapter 1*. OPEF and TPEF lie their differences in the way that the excited state is reached, but not in the way that the excited state is deactivated to populate again the ground state S_0. Fluorescence in both cases is only one of the possible ways that the excited molecule can undergo to the ground state. Thus, in TPEF, alike in OPEF, a magnitude called quantum yield of fluorescence can be introduced, and we denote it as Φ_{2f}, in order to distinguish it from the quantum yield of fluorescence in the SPEF case, Φ_f. In **Box 2.4**, some basic relations are given, describing quantitavely the TPEF.

BOX 2.4: **Basic relations describing TPEF**

In TPEF, the quantum yield of fluorescence Φ_{2f} is defined as:

$$\Phi_{2f} = \frac{\text{number of fluorescence emitted photons}}{\text{number of pair of absorbed photons}} \tag{2.17}$$

Eq. (2.4) gives the rate, W_2 at which a molecule populates an excited state through two-photon absorption. This rate, when multiplied by the fluorescence quantum efficiency Φ_{2f}, provides the rate at which a photon is emitted from the molecule, which undergoes from the excited to the ground state. In other words, the power of the TPEF, P_{TPEF} in $\frac{photons}{\text{sec}}$ is given by:

$$P_{TPEF} = \frac{1}{2}\Phi_{2f}\sigma_2 I^2 \tag{2.18}$$

Finally, if we define $\sigma_{TPEF} = \Phi_{2f}\cdot\sigma_2$ as the two-photon fluorescence cross-section (or action cross-section), eq. (2.18), can be expressed as:

$$P_{TPEF} = \frac{1}{2}\sigma_{TPEF} I^2 \tag{2.19}$$

The fluorescence emission of an excited molecule, regardless if it is about OPEF or TPEF, is characterized by its *radiation pattern*, the *polarization* of the emitted photons, and its *spectral distribution*.

The radiation pattern of fluorescence is isotropic. The propagation of the emitted photons does not have a preferable direction, and is not related with the propagation direction of the incident light beam causing the excitation. Both OPEF and TPEF are incoherent processes, since they include absorption and re-emission of photons, with finite lifetimes of the populated excited states. In this sense, when a collection of fluorescent molecules is assumed, the total fluorescence radiation results from an incoherent summation of the radiation originated from the singles molecules. This fact has two important sequences. First, the total generated TPEF (or OPEF) power scales as the number of the fluorescent molecules: $P_{TPEF} \sim N$. Second, the incoherent summation does not permit a preferable direction of the fluorescence emission to arise, even when the fluorescent molecules are well aligned to each other, unlike in the case of the second-harmonic generation (SHG), as it will be shown analytically in the following chapter.

As far as the polarization of the emitted photons through fluorescence is concerned, it is expected that when fluorescent molecules are illuminated with linear polarized light, the emitted photons have a specific polarization, related with the polarization of the incident photons and the specific transition moment between the excited and the ground state. This specific transition is directly related with the orientation of the molecules in the space. However, since the molecules are free to rotate during the time taken for the electronic transitions to occur, changing their orientation and the corresponding transition moment, the fluorescence emission is largely unpolarized. For small fluorescent molecules, the rotational correlation time is much shorter than the fluorescence lifetime. For example, fluorescein has a rotational correlation time of 120 ps, 40 times shorter than its fluorescence lifetime [32]. By contrast, when the fluorescent molecule is relatively large, its rotational correlational time is larger than its fluorescence lifetime, and the fluorescence emission is more polarized. GFP is an example of such a fluorescent molecule [33].

Finally, as far as the spectral distribution of the fluorescence emission is concerned, OPEF and TPEF emission spectra were exactly the same in most cases reported in literature [34]. This is expected as it was mentioned above. However, there are reported cases, where slight differences between the emission spectra were observed [35].

3. TPEF MICROSCOPY

TPEF microscopy was introduced by Denk, Webb and coworkers in 1990 for biological and medical studies [1]. Ever since, TPEF microscopy has been used extensively and has become a laboratory standard, since it offers unique possibilities for the characterization of biological samples. TPEF microscopy is often compared with confocal microscopy, which is an example of one-photon excited fluorescence microscopy. Owing to this comparison, a brief presentation of the confocal microscopy follows.

Scanning confocal microscopy was invented in 1962 by Minsky demonstrating that 3-D resolved images can be obtained in translucent specimens without physical sectioning [36,37]. In **Figure 2.2** the principle of the confocal microscopy is depicted.

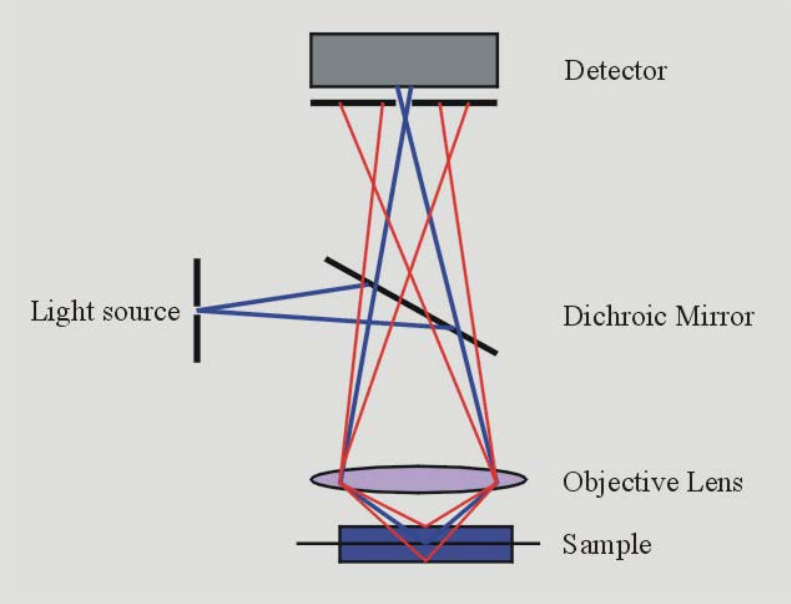

Figure 2.2 Principle of the confocal microscopy. Two pinholes, one before the dichroic mirror and a second just in front of the detector, assure that fluorescence originated only from the focal plane, will reach the detector.

As it is depicted, incident visible light is focused on the biological specimen to the diffraction limit by means of an objective lens. One-photon excited fluorescence is produced in an extended region of the specimen, and not only in the plane of focus. Since the one-photon absorption is a linear process, the intensity of light is enough to excite the fluorescent molecules, also out of the focal volume. However, 3-D resolution is obtained by placing a pinhole aperture in the emission light path at a conjugate location of the focal volume in the specimen. Photons generated inside this volume will be focused at the pinhole aperture and can be transmitted to the detector. On the contrary, photons originated outside this focal volume will be defocused at the aperture plane and will be blocked. In other words the

maximum resolution in the longitudinal direction, denoted as z, is achieved by placing a pinhole before the detector, while the maximum resolution in the transversal directions in the plane of focus, denoted as x and y is achieved by the tight focusing of the incident beam to the diffraction limit, by means of an efficient objective lens. It must be emphasized, however, that 3-D resolution (in the longitudinal direction), is obtained by limitation of the region of observation, not of the region of excitation, as in the transversal directions.

On the other hand, TPEF microscopy is an alternative 3-D imaging technology. A typical TPEF microscope is very similar to the confocal microscope, and will be described analytically in the experimental part of this work. Its main difference from the confocal microscope is the lack of pinholes, since its 3-D sectioning ability is based on the limitation of the excitation region, in all three directions, x, y and z. The incident light lies, this time, in the infrared region of the optical spectrum, and the fluorophores contained in the sample can absorb light, only through the nonlinear two-photon absorption process. Since the two-photon absorption cross-section σ_2 is significantly lower than the one-photon absorption cross-section σ_1, as eq. (2.5) implies, two-photon absorption occurs with appreciable rates only in regions of high temporal and spatial photon concentration. The high temporal concentration of photons is achieved by the availability of pulsed lasers with pulse widths of the order of 100 fs. The high spatial concentration of photons is achieved as in the confocal microscope, by focusing the beam with a high numerical aperture (NA) objective to a diffraction limited focus. Almost the total fluorescence intensity comes from a $2\,\mu m$ thick region about the focal point for objectives with high NA (1.25), like the one used in this work. Thus, 3-D images can be constructed without a confocal pinhole due to the quadratic dependence of two-photon fluorescence intensity upon the excitation photon flux (eq. (2.4)), which decreases rapidly away from the focal point. In **Figure 2.3** it is depicted the main difference between the one-photon confocal and the TPEF microscopy, as far as the excitation region is concerned. It is shown that in the confocal microscopy, the out-of-focus plane excitation is very intense, whereas in the TPEF microscopy is not.

Confocal and TPEF microscopy have their own advantages and disadvantages compared to each other. TPEF microscopy is more adequate for deep tissue imaging since the excitation wavelength lies in the IR and suffers less from tissue absorption and scattering. On the other hand, the excitation wavelengths of confocal microscopy lie in UV and blue region, thus the penetration depth is limited.

a) 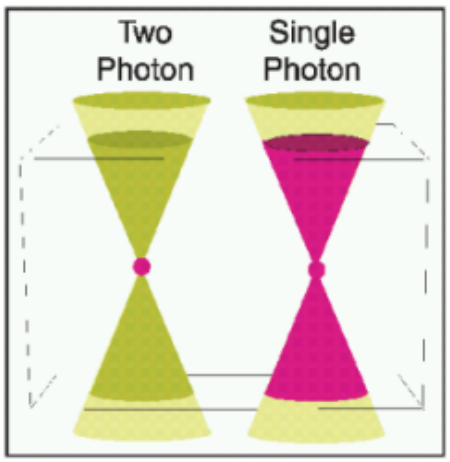

b) 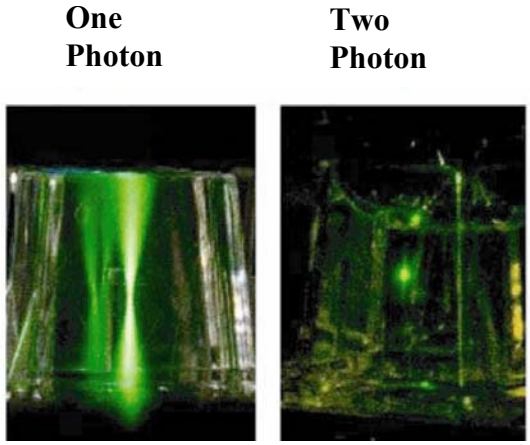

Figure 2.3 a) The excitation region (pink color) is limited in the focal plane for the two-photon case, while extends above and below in the one-photon excitation. b) The same characteristic is noted in the two comparative pictures.

Apart from the deeper penetration, TPEF microscopy exhibits two more important advantages. First, since the excitation light is in the IR region, the wide separation between the excitation and the emission spectra ensures that the excitation light can be rejected without filtering out any of the fluorescence photons, resulting in sensitivity enhancement and better signal to noise ratio (SNR). Second, the fact that the 3-D sectioning arises from the limitation of the excitation region, ensures that photobleaching and photodamage of the biological specimen are restricted only to the focal point. Since out-of-plane fluorophores are not excited, they are not subject neither to photodamage nor to photobleaching. The minimally invasive nature of two-photon imaging can be best appreciated in a number of embryology studies. Previous work on long-term monitoring of *C. elegans* and hamster embryos using confocal microscopy failed because of photodamage-induced developmental arrest. However, posterior TPEF microscopy studies indicated that the embryos of these organisms can be imaged repeatedly over the course of hours without observable damage [38,39].

At this point it is necessary to describe briefly the terms photobleaching and photodamage. Photobleaching occurs when, under illumination, the triplet state in the fluorophore reacts with molecular oxygen, forming a nonfluorescing molecule. According to Sandison et al. [40], photobleaching tends to limit the fluorescence emission to a maximum of $\sim 10^5$ $\frac{photons}{molecule \cdot \sec}$ for some of the best fluorophores in living cells.

On the other hand the term photodamage is more general and describes various mechanisms. Endogenous and exogenous fluorophores act as photosensitizers in photo-oxidative processes [41,42], and the photoactivation of these fluorophores results in the formation of reactive oxygen species that trigger the subsequent biochemical damage cascade in cells. Flavin-

containing oxidases have been identified as one of the primary endogenous targets for photodamage [43].

As far as the resolution of the two techniques is concerned, confocal microscopy is advantageous. For the excitation of the same fluorophore, two-photon resolution in x and y direction, is roughly half the one-photon confocal resolution, given that the excitation beam is focused to the diffraction limit. This lower spatial resolution is due to the use of longer wavelength light, approximately twice as long as the excitation light in confocal microscopy. However, in many practical setups the focusing of the fundamental laser beam to the diffraction limit is not feasible. In these cases, the resolution of the TPEF microscopy in x and y direction is superior to the corresponding resolution of the one-photon confocal microscopy, due to the quadratic dependence of two-photon fluorescence intensity upon the excitation photon flux. The resolution of the two kinds of microscopy in the longitudinal direction can not be directly compared, owing to the dependence of the confocal resolution on the size and the quality of the pinhole. However, it is of the same order of magnitude. In **Box 2.5** the TPEF active volume is defined as the region from where the TPEF exclusively originates. Analytical expressions are presented.

BOX 2.5: **TPEF active volume – Resolution of TPEF microscopy**

The usual description of a Gaussian beam emerges from the paraxial approximation. However, the paraxial approximation is not valid when the beam is tightly focused.
The electric field of a Gaussian tightly focused excitation beam of angular frequency ω propagating in the z direction and polarized in the $\hat{\varepsilon}$ direction may be approximated by:

$$\vec{E}(x,y,z) = -iE_{\omega}\exp\left(-\frac{x^2+y^2}{w_{\rho}^2}-\frac{z^2}{w_z^2}+i\xi k_{\omega}z\right)\hat{\varepsilon} \qquad (2.20)$$

where w_{ρ} and w_z are respectively the radial and axial beam waists at the focal center, $\hat{\varepsilon}$ is a unit vector in the $x-y$ plane, k_{ω} is the wave vector at frequency ω, and ξ represents the effective reduction in the axial propagation vector caused by the phase anomaly, or Gouy shift. Eq. (2.20) will be discussed further in the next chapter. We define the TPEF active volume as the volume from where TPEF almost exclusively originates. This volume is critically dependent on the radial and axial beam waists, w_{ρ} and w_z, and is given by:

$$V_{TPEF} = \left(\frac{\pi}{2}\right)^{(3/2)} w_{\rho}^2 w_z \qquad (2.21)$$

Owing to the above definition of the TPEF active volume, the longitudinal and the transversal resolution of the TPEF microscopy are defined as w_z and w_{ρ}, correspondingly. In **Figure 2.4** a focused Gaussian beam is

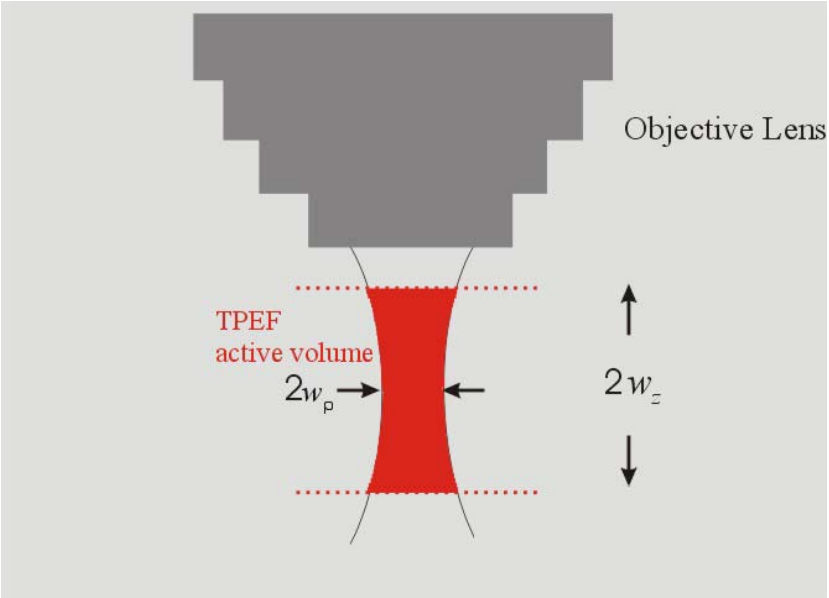

Figure 2.4 Tightly focused Gaussian beam. The radial and axial beam waists, w_ρ and w_z correspondingly, determine the TPEF active volume, the region from which TPEF exclusively originates.

4. BIOPHYSICAL APPLICATIONS OF TPEF MICROSCOPY

Fluorophores utilized in two-photon tissue imaging are divided in two classes, endogenous and exogenous.

As it was described in *chapter 1*, most proteins are fluorescent due to the presence of tryptophan and tyrosine. However, two-photon tissue imaging based on amino-acid fluorescence is uncommon, because these amino-acids have one-photon absorption in the UV spectral range (250-300 nm). Two-photon excitation of these fluorophores requires femtosecond laser sources with emission in the range of 500-600 nm, which is not easily available. Two-photon imaging of cellular structures is often based on the fluorescence of NAD(P)H [44] and flavoproteins [25]. NAD(P)H has a one-photon absorption spectrum at about 340 nm, whereas flavoproteins around 450 nm.

Two-photon microscopy can also image extracellular matrix structures in tissues. Two of the key components in the extracellular matrix are collagen and elastin, as it was mentioned in *chapter 1*. Elastin has excitation wavelengths of 340-370 nm, and can be readily imaged by two-photon excitation in the wavelength range of about 800 nm. Similarly, many types of collagen have among others excitation wavelengths around 400 nm, thus TPEF of collagen can be readily achieved and observed in many two-photon systems.

While autofluorescent tissue structures can be readily studied, the study of nonfluorescent components is difficult. However, many biochemical processes are based on nonfluorescent

structures, and for their monitoring, compatible fluorescent exogenous probes should be developed and uniformly delivered into intact, in vivo tissues. As it was discussed in *chapter 1*, for the OPEF case, GFP plays the same significant role in the TPEF case, and is one of the most important, genetically encoded, exogenous fluorophores, used in TPEF microscopy.

Two-photon microscopy has found an increasingly wide range of applications in biology and medicine. The advantage of two-photon imaging has been well demonstrated in neurobiology, embryology, dermatology and pancreatic physiology. Especially, as far as the neurobiological studies are concerned, TPEF microscopy provide 3-D mapping of neuron organization and assays neuron communications by monitoring action potentials, calcium waves and neural transmitters. Many two-photon neural biological studies have focused on the remodeling of neuronal dendritic spines or on the dynamics of calcium signal propagation [45,46]. Others focused on system level interactions of neurons [47,48], neuronal hemodynamics [49], or on the in vivo study of neuronal pathology [50,51].

1. INTRODUCTION - HYPER-RAYLEIGH SCATTERING (HRS) FROM A SINGLE MOLECULE

Second-harmonic generation (SHG) microscopy was used several years prior the invention of TPEF microscopy. In 1962 SHG was first demonstrated by Kleinmann in crystalline quartz [52], and in 1974, Hellwarth first integrated SHG into an optical microscope to visualize the microscopic crystal structure in polycrystalline ZnSe [53]. SHG microscopy was introduced in the field of biology, first in 1979 [54]. Ever since the use of SHG microscopy has been extended, finding potential for new applications, especially with the discovery of exogenous markers, which can lead to high signal levels. Intrinsic structures of biological systems, as well as exogenous markers, when properly designed and collectively organized, can produce signal levels easily comparable to those encountered in standard TPEF microscopy [55]. Moreover, as it will be shown below, the spatial resolutions provided by the SHG and TPEF microscopies are commensurate, meaning that the two contrast modes can be conveniently derived from the same instrument.

Despite their similarities, SHG and TPEF are based on fundamentally different phenomena [2,56]. As it was described in *chapter 2*, TPEF relies on nonlinear absorption followed by fluorescence emission. On the contrary, SHG relies on nonlinear scattering and is a coherent process. For a complete analysis of the SHG radiation, emerging from biological samples, SHG must be examined first at the molecular level. At this level, SHG is usually referred to as Hyper-Rayleigh Scattering (HRS). Afterwards, SHG from an assembly of molecules must be examined, as it arises from the coherent summation of the radiation of the individual molecules-radiators.

To first order, the molecule may be regarded as a simple electrical dipole. That is, the molecular electron distribution may be regarded as mobile relative to the nuclear distribution, and the molecular dipole moment is defined as $\vec{\mu} = q\vec{r}$, where q is the nuclear and electronic charges and $\vec{r}$ is their relative displacement. Changes in $\vec{\mu}$ are occasioned by forces applied to the molecular electrons. In the analysis carried in this chapter, only electric dipole forces are considered, that is forces whose interaction energies are given by $W = \vec{\mu}\vec{E}$, where $\vec{E}$ is the applied (incident) electric field. The molecules, as electric dipoles, can either be symmetrical or asymmetrical. The simplest form of asymmetry is possessed by a uniaxial polar molecule. In this case the molecule may be regarded as a one-dimensional rod, along which its electron cloud can shift up or down. We begin by examining the case when the molecule is perfectly symmetric, meaning that the molecular dipole moment vanishes at rest.

Upon illumination, the electron cloud, depicted in **Figure 3.1** as a point electron, is subject to a sinusoidal force along the molecular axis, whose frequency is ω. Because the molecule is symmetric, the resultant oscillation of the electron cloud is also symmetric and generates radiation at the same frequency ω. Such radiation is called *Rayleigh scattering* [57]. It is linear in the sense that the scattered frequency is exactly the same as that of the driving illumination light. In this example of a symmetric molecule, no second-harmonic light (light of frequency 2ω) can be generated.

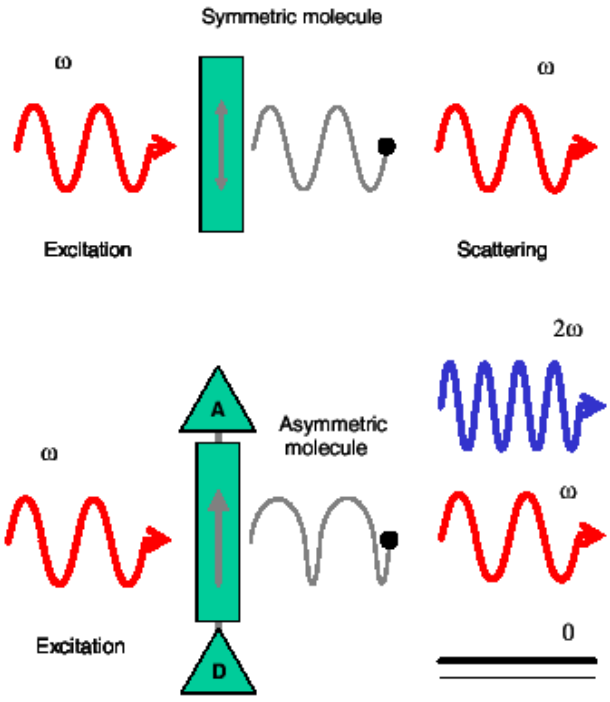

Figure 3.1 When driven by light of frequency of ω, the induced electron motion in a symmetric uniaxial molecule produces Rayleigh scattering at the same frequency ω. In an asymmetric molecule, the induced electron motion produces scattered light at frequencies ω and 2ω. The latter is called Hyper-Rayleigh scattering (HRS).

One way to impart charge asymmetry on a molecule is by grafting electron donor (D) and acceptor (A) moieties to its opposite ends, producing what is known as a "push-pull" chromophore [58], since both moieties act in tandem to favor electronic motion in the direction $D \rightarrow A$. When an asymmetric molecule is subjected to the same sinusoidal driving field as above, the resultant electron motion, though still periodic, is no longer symmetric, as shown in the lower part in **Figure 3.1**. The acceleration of the electron motion contains additional frequency components. In addition to the usual linear component at frequency ω, the scattered radiation contains nonlinear components at frequencies 0 and 2ω. The 0 frequency component is called optical rectification [56]. The 2ω component is called Hyper-

Rayleigh scattering (HRS), and is the center of the analysis, carried out in this chapter. As a general rule, the generation of second-harmonic light requires a non-symmetric source. In **Box 3.1**, the basic equations describing the HRS from a single molecule are presented. The description includes the definition of the SHG cross-section σ_{SHG}, so that a direct comparison between the SHG and the TPEF emission can be made at the molecular level [59].

BOX 3.1: **SHG originated from a single molecule**

Molecular SHG is caused by the nonlinear dependence of the induced dipolar moment $\vec{\mu}$ of the molecule on the incident optical electric field $\vec{E}$. Thus $\vec{\mu}$ can be expanded in a Taylor's series about $\vec{E} = 0$:

$$\vec{\mu} = \vec{\mu}_o + \alpha * \vec{E} + \frac{1}{2}\beta * \vec{E} * \vec{E} + \frac{1}{6}\gamma * \quad E * E + \ldots \tag{3.1}$$

where α is the linear molecular polarizability and β and γ are the nonlinear first and second hyperpolarizabilities [2]. SHG is governed by β, which is a tensor with 27 elements β_{ijk}, where $i, j, k = x, y, z$. For simplicity we assume the simplest form of asymmetric molecules, those having the character of "push-pull" molecules. They are uniaxial polar molecules, which can be regarded as rods, as in Figure 3.1. We further assume that such a "rod" is aligned along the axis, and that the excitation field is linearly polarized in the same direction. Under this description, only the component plays an active role and should be examined. If the excitation light has frequency ω, the induced dipole moment at frequency 2ω will be given by:

$$\vec{\mu}_{2\omega} = \frac{1}{2}\beta_{xxx} \cdot E^2 \hat{x} \tag{3.2}$$

where E is the excitation field amplitude. The radiated second-harmonic far field at an inclination ψ from the x axis is:

$$\vec{E}_{2\omega}(\psi) = -\frac{\mu_{2\omega}\omega^2}{\pi\varepsilon_0 c^2 r}\sin(\psi)e^{-2i\omega t} \tag{3.3}$$

where ε_0 is the free-space permittivity, c is the speed of light, r is the observation distance from the dipole, and $[t]$ is the corresponding retarded time. The resultant power per differential solid angle at an inclination ψ, in units of $photons/\sec$, may be expressed as:

$$P_{2\omega}(\psi) = -\frac{3}{16\pi}\sigma_{SHG}\sin^2(\quad)I \tag{3.4}$$

where I is the excitation intensity in units of $photons/$ and σ_{SHG} is defined (in $cm^4 \cdot \sec/\ photon \cdot molecule$) as:

$$\sigma_{SHG} = \frac{4n_{2\omega}\hbar\omega^5}{3\pi n_\omega^2 \varepsilon_0^3 c^5}\left|\beta\right|^2 \tag{3.5}$$

In eq. (3.5) n_ω and $n_{2\omega}$ are the indices of refraction at ω and 2ω. The definition of σ_{SHG} is such, that the total power, obtained by integration of eq.(3.4) over all solid angles, reduces to the simple expression:

$$P_{SHG} = \frac{1}{2}\sigma_{SHG} I^2 \tag{3.6}$$

We recall that the fluorescence emitted by a molecule, undergoing two-photon excitation can be expressed similarly according to eq. (2.19) as $P_{TPEF} = \frac{1}{2}\sigma_{TPEF} I^2$. In this sense, σ_{SHG} and σ_{TPEF} may be expressed in the same units for direct comparison.

2. COHERENT SUMMATION OF THE HRS FROM THE INDIVIDUAL MOLECULES

Some important aspects of HRS are considered now, that distinguish it from Rayleigh scattering or from fluorescence. As an illustration, two asymmetric molecules are considered, that are located in close proximity, separate by a distance d much smaller than an optical wavelength, and oriented in parallel directions. When these molecules are illuminated by a driving field, their respective electron motions will be identical, and the resultant HRS from both molecules will be in phase (**Figure 3.2a**). In other words, the net HRS amplitude will be doubled, meaning that the net HRS power will be quadrupled relative to the HRS power obtained from a single molecule. If, on the other hand, the two molecules are oriented anti-parallel, the asymmetric components in their electronic motions are now inverted relative to one another. Thus, their respective HRS amplitudes are out-of-phase and exactly cancelled (**Figure 3.2b**). More specifically, it has been empirically found, that in biological samples, when two antiparallel oriented molecules have a distance $d < \lambda/10$, they do not produce a total detectable signal [59,60]. It is noted that the dependence of radiative phase on molecular orientation is a characteristic property of HRS, that does not appear neither in Rayleigh scattering nor in fluorescence. In particular, the Rayleigh scattered components from both molecules in Figure 3.2 remain in phase regardless of whether the molecules are oriented parallel or anti-parallel. Similarly, if the molecules are fluorescent, the phases of their fluorescence emission are essentially random, also independent on molecular orientation.

For imaging applications, one is not interested in looking at the HRS from one, or even two molecules, but from an entire population of molecules. First, a configuration of N molecules in solution is considered (**Figure 3.3a**). Since the orientations of these molecules are random, the phases of their individual SHG contributions are also random. The molecules produce

HRS incoherently, and the total generated HRS scales as the number of the radiating molecules: $P_{HRS} \sim N$. This same scaling law applies to fluorescence, as it is described in *chapter 2*. Alternatively, in **Figure 3.3b** a configuration is illustrated, where the

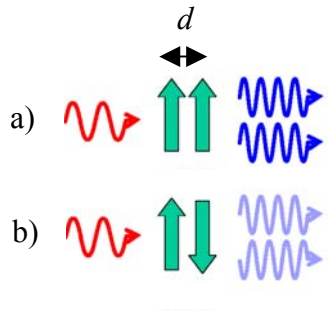

Figure 3.2 The HRS from two molecules located close together. a) If the molecules are parallel, their HRS are in phase and interfere constructively. b) If the molecules are anti-parallel, their HRS are out-of-phase and cancel each other.

molecules are globally aligned along the same direction. The phases of the individual HRS contributions from each molecule are now prescribed by the phase of the driving field, which is presumambly well defined. The HRS is therefore produced coherently, meaning that interference effects play a significant role. When HRS is produced coherently by an organized population of molecules, it is called SHG. Due to the coherent character of SHG, its total power scales as the square of the number of radiating molecules: $P_{SHG} \sim N^2$. Moreover, because of the same character, the angular distribution of SHG is highly structured. In general, SHG is constrained to propagate along the same direction as the driving field. Much more will be refered about the radiation pattern of SHG in the continue of this chapter. As a conclusion, for imaging applications, it is highly desirable that the radiating molecules are organized than unorganized, because first, much more signal is generated for the same number of molecules, and second, the signal can be collected more efficiently due to its high directionality.

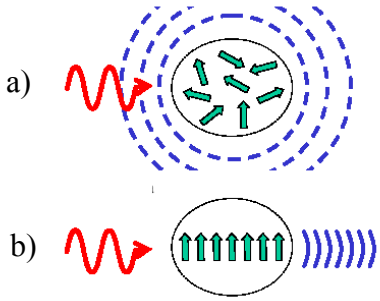

Figure 3.3 The HRS from a population of N molecules. a) Randomly oriented molecules scatter incoherently and the total HRS scale as N. b) Aligned molecules scatter coherently producing SHG. This signal is well directional, and its power scales as N^2.

When a nonlinear medium (organized population of asymmetric molecules) is excited by an excitation source, the material can be described conveniently using the macroscopic nonlinear susceptibilities. This description is, however, ideal only when the excitation source is a planar wave, but is still adequate, also when the excitation source is a collimated beam, or even a weakly focused beam. However, when the nonlinear medium is excited from a tightly focused beam, as it is in the case of SHG microscopy, where high-resolution is demanded, the macroscopical description is inadequate. In that case, the description must refer to the molecular level, using the molecular hyperpolarizabilities. Each molecule scatters the driving field according to its SHG cross-section (eq. (3.5)), and their resultant electric field contributions in the radiation zone are summed-up coherently, in the same manner as for phased-array antennas [61]. In this work, describing the construction and the applications of a SHG microscope, the insight in the molecular level is the appropriate way to describe the nonlinear response of the biological specimen. In a next paragraph, the calculations for the coherent summation of the individual molecular HRS, resulting in a total SHG signal, will be presented, and conclusions for the directionality and the magnitude of the signal will be carried out. However, some basics for the macroscopical description of SHG are provided in **Box 3.2**, in order to obtain a full understanding of the nonlinear phenomenon of SHG.

BOX 3.2: **Macroscopical description of SHG**

The nonlinear response of a material to an incident electric field, can be described, as it was mentioned in *chapter 2*, by eq. (2.6), which is reproduced here for convenience:

$$P = \chi^{(1)} * E + \chi^{(2)} * E * E + \chi^{(3)} * E * E * E + \ldots \tag{3.7}$$

While TPEF is determined by the 3rd order susceptibility tensor $\chi^{(3)}$, SHG is correspondingly determined by the 2nd order susceptibility tensor $\chi^{(2)}$. $\chi^{(2)}$ is a bulk property of the medium, referring to the entire population of the individual molecules of the medium. The total power of the generated second-harmonic signal P_{SHG}, is proportional to:

$$P_{SHG} \sim \left(\chi^{(2)}\right)^2 I^2 \tag{3.8}$$

where again I is the excitation intensity in units of $photons / \sec \cdot area$. The bridging between the macroscopical behavior of the material, as far as SHG is concerned, and the HRS originated from the individual molecules is achieved through the relation:

$$\chi^{(2)} = N_s \langle \beta \rangle \tag{3.9}$$

where N_s is the density of molecules, and β is the first molecular hyperpolarizibility, as it has already been defined in Box 3.1. The brackets denote an orientational average, which shows the need for orientational organization among the molecules that constitute the material. Moreover, it makes clear the need for an

environment lacking a center of symmetry. In other words, media that are characterized by inversion symmetry, do not have the ability for SHG, since their $\chi^{(2)}$ becomes zero. This property is well known [62]. Let us assume now, to our convenience, that we have a population of molecules, completely aligned to each other, so that the brackets do no have a sense anymore. Combining eq. (3.5) and (3.9), it is clear that the molecular SHG cross-section, σ_{SHG} is proportional to the square of the 2nd order susceptibility tensor $\chi^{(2)}$:

$$\sigma_{SHG} = \frac{4n_{2\omega}\hbar\omega}{3\pi n_{\omega}^{2}\varepsilon_{0}^{3}c^{5}}\left|\chi^{(2)}\right|^{2} \tag{3.10}$$

We recall combing eq. (2.16) and (2.19) that the molecular TPEF cross-section, σ_{TPEF} is proportional to the imaginary part of the 3rd order susceptibility tensor $\mathrm{Im}\left\{\chi^{(3)}\right\}$. As such, σ_{TPEF} tends to be much larger than σ_{SHG} in practice. However, due to the coherent character of the SHG, and the coherent summation of the HRS from the individual molecules, the total SHG signal can be comparable or even larger from the total TPEF signal, emerging from an entire population of molecules.

For the coherent summation of the HRS radiations from single molecules, the knowledge of three parameters is necessary. First, the characteristics of the molecular hyperpolarizibility of the single molecules. Second, the way in that, the single molecules are globally organized inside the biological specimen. Third, the way in that the beam is incident on the sample, and particularly if the beam is collimated or it is tightly focused. In **Figure 3.4**, it is depicted the simplistic case of a collimated beam, incident on a region, where well-organized asymmetrical molecules are located. The beam can be described in this region as a planar wave with its wavefronts well-defined and perpendicular to the propagation axis z.

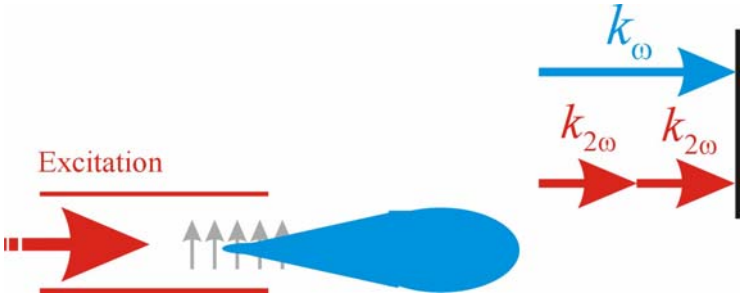

Figure 3.4 SHG from well-organized asymmetrical molecules, when illuminated by a collimated laser beam. Momentum coservation principle assures that the SHG signal propagates on-axis.

The phase of the HRS produced by each molecule is governed by the phase of the driving field. However, in this case, the driving field is propagating, meaning that the HRS produced

by the individual molecules-emitters propagates as well: Molecules that are located leftmost, generate HRS earlier than those located rightmost. The resulting SHG radiation pattern can be evaluated by treating each molecule in the interaction area as a local emitter of second-harmonic radiation. The phase and amplitude of this radiation is precisely determined by the phase and the amplitude of the driving field at the same location. When the second-harmonic contributions from each molecule, given by eq. (3.3), are added, taking into account their respective phase and amplitude, the resulting total SHG is found to propagate in the same direction as the driving field. This result arises directly from the "*momentum conservation principle*", and describes the well-known in nonlinear optics "*phase matching condition*": To ensure momentum conservation in the axial direction, the second-harmonic photon whose momentum is twice that of a driving photon, must propagate in the same direction as the driving photons, as illustrated vectorially in Figure 3.4.

The illumination geometry, depicted in Figure 3.4, is simplistic and does not correspond to geometries used in laser scanning microscopy. In *chapter 2*, it has been already noted that the 3-dimensional microscopic resolution of TPEF microscopy emerges from the tight focusing of the illumination laser beam to a microscopic spot size. The intensity is large enough to provoke two-photon absorption, only in a restricted area around its focal center. This is the case in the SHG microscopy as well. The rigorous confinement of TPEF to a small volume stems from its quadratic dependence on excitation intensity, as eq. (2.19) implies. Inasmuch as SHG also depends quadratically on excitation intensity, as eq. (3.6) implies, it is expected that the active SHG volume, and hence the effective resolution afforded by SHG microscopy is the same as that in TPEF microscopy. This turns to be true in almost all practical cases of interest, and in general, the SHG and TPEF active volumes may be defined identically [59].

A focused beam differs from a collimated beam, not only as far as the restriction of the intensity is concerned, but also as far as its phase fronts are concerned. Its phase fronts are no longer evenly distributed along its propagation axis. This characteristic must be taken into account, when the coherent summation of the individual molecules-emitters is carried out, since the phase of the emitters is determined by the phase of the driving (focused) beam. The radiation pattern changes dramatically, and the SHG signal does not propagate on-axis anymore. In Box 2.5 the mathematical description of a focused beam in the vicinity of the focal spot was given. In **Box 3.3** this description is repeated, the HRS contributions of the single molecules restricted in the active volume, are coherently summed, and the characteristics of the second-harmonic radiation are described [59]. The description distinguishes between geometries, where the individual molecules are distributed a) on a 1-D

line, in the propagation direction, b) on a 2-D surface in the plane parallel to the propagation direction, and c) in a 3-D volume. The first geometry has little practical usage. However, the second geometry describes pretty well exogenous SHG from chromophores, grafted on cellular membranes, as it will be explained in the next paragraph. Finally, the third geometry describes mainly endogenous SHG, from structural proteins like collagen, actomyosin complexes and tubulin. Endogenous SHG will be presented analytically in a following paragraph.

BOX 3.3: **Description of a focused beam – SHG active volume – Coherent summation of HRS from single molecules**

The electric field of a tightly focused excitation beam of angular frequency ω propagating in the z direction and polarized in the $\hat{\varepsilon}$ direction may be approximated by:

$$\vec{E}(x,y,z) = -iE_\omega \exp\left(-\frac{x^2+y^2}{w_\rho^2} - \frac{z^2}{w_z^2} + i\xi k_\omega z\right)\hat{\varepsilon} \tag{3.11}$$

where w_ρ and w_z are respectively the radial and axial beam waists at the focal centers, $\hat{\varepsilon}$ is a unit vector in the $x-y$ plane, k_ω is the wave vector at frequency ω, and ξ represents the effective reduction in the axial propagation vector caused by the phase anomaly, or Gouy shift [63]. In the case of relatively weak focusing ξ may be approximated by $(1-\frac{2}{k_\omega^2 w_\rho^2})$, whereas for tight focusing this expression tends to be a slight overestimate.

The active SHG volume can be defined as :

(1-D line distribution of molecules) $$V_{(1)} = \left(\frac{\pi}{2}\right)^{1/2} w_z \tag{3.12a}$$

(2-D surface distribution of molecules) $$V_{(2)} = \left(\frac{\pi}{2}\right) w_\rho w_z \tag{3.12b}$$

(3-D volume distribution of molecules) $$V_{(3)} = \left(\frac{\pi}{2}\right)^{(3/2)} w_\rho^2 w_z \tag{3.12c}$$

Eq. (3.12c) provides the same result for the SHG active volume, as eq. (2.21) for the TPEF active volume. The transversal and longitudinal resolution are again defined as w_ρ and w_z, correspondingly.

Eq. (3.2) provides the induced dipole moment at frequency 2ω of a single uniaxial molecule, when the driving field is linear polarized, parallel to the axis of the molecule. For the coherent summation below, we generalize, and we do not exclude other kinds of asymmetry, or other relation between the orientation of the molecules relative to the polarization of the field. Thus, no one of the 27 elements of the tensor β is a-priori zero. The basic strategy for the coherent summation consists in averaging the molecular dipole moments over regions of the active volume, whose dimensions are small compared with the radiation

$$\vec{\mu}_{2\omega,i}(x,y,z) = \frac{1}{2}\vec{E}_{\omega}(x,y,z)\sum_{j,k}\left\langle \beta_{ijk} \right\rangle \hat{\varepsilon}_j \hat{\varepsilon}_k \tag{3.13}$$

where $\langle \beta \rangle$ is the local ensemble-averaged unit-density hyperpolarizability. It should be noted that eq. (3.13) is the generalized form, when the molecules are arranged in a 3-D volume. In other cases the molecules may be distributed in a 2-D plane ($x-z$) or even along the axis of propagation z . We proceed, however, further with the general case. All the molecules taken in the average at a given position (x,y,z) are driven in phase with one another, and the net local second-harmonic dipole moment per unit volume generated at this position is simply $N_{(d)} \cdot \vec{\mu}_{2\omega}(x,y,z)$, where $N_{(d)}$ is the molecular spatial density. Referring to **Figure 3.5**, the radiation state is defined by three unit vectors, $\hat{r},\hat{\theta},\hat{\varphi}$ corresponding to the propagation direction, the p-polarization direction and the s-polarization direction respectively. That is:

$$\begin{aligned} \hat{r} &= \sin\theta\cos\varphi\hat{x} + \sin\theta\sin\varphi\hat{y} + \cos\theta\hat{z} \\ \hat{\theta} &= \cos\theta\cos\varphi\hat{x} + \cos\theta\sin\varphi\hat{y} - \sin\theta\hat{z} \\ \hat{\varphi} &= -\sin\varphi\hat{x} + \cos\varphi\hat{y} \end{aligned} \tag{3.14}$$

To begin, we first write the contribution to the radiated electric field from the local induced second-harmonic dipole moment per unit molecular concentration at the focal center only (indicated by the superscript $^{(0)}$). In the direction $\{\theta,\varphi\}$ or Ω for short, this is given by:

$$\vec{E}_{2\omega}^{(0)}(\Omega) = \frac{\eta}{r}\begin{bmatrix}\hat{\theta}\\ \hat{\varphi}\end{bmatrix}\cdot\vec{\mu}_{2\omega}(0,0,0) \tag{3.15}$$

where $\eta = \dfrac{\omega^2}{\pi\varepsilon_0 c^2}$, r is the far-field propagation distance to the observer, and $\vec{E}_{2\omega}^{(0)}(\Omega)$ has been separated into its p- and s-polarization. The total radiated field in the propagation direction Ω is then given by the coherent summation of the contributions from the local induced second-harmonic dipole moments at all points (x,y,z), with their associated spatially dependent phase shifts taken into account. It is found then that:

$$\vec{E}_{2\omega}(\Omega) = \frac{\eta N_{(d)}}{r}\int\begin{bmatrix}\theta\\ \varphi\end{bmatrix}\cdot\vec{\mu}_{2\omega}(x,y,z)\exp\left\{-k_{2\omega}\left[(x,y,z)\cdot\hat{r}\right]\right\}dxdydz \tag{3.16}$$

For the derivation of eq. (3.16) it is assumed that $N_{(d)}$ is constant inside the SHG active volume and that $\langle \beta \rangle$ is independent of position, on average. On integration, eq. (3.16) yields:

$$\vec{E}_{2\omega}(\Omega) = N_{(d)}V_{(d)}A_{(d)}\vec{E}_{2\omega}^{(0)}(\Omega) \tag{3.17}$$

where $V_{(d)}$ is the SHG active "volume" (corresponding to length, area or volume for d=1,2 or 3 respectively, given by eq. (3.12)), and $N_{(d)}$ is the molecular density (linear density, surface density or volume density for d=1,2 or 3 respectively). It should be noted that the integral in eq. (3.16) is indeed a volume integral only in the case where d=3, whereas is a surface integral when d=2, and a simple linear integral when d=1. Finally, $A_{(d)}$ is an "antenna" factor arising from the phased-array summation of the radiated fields from the distributed sources-molecules, also dependent on the dimensionality. It is convenient to define three components to this antenna factor:

$$A_x = \exp\left\{-\frac{k_{2\omega}^2 \cdot w_\rho^2 \left(\sin\theta\cos\varphi\right)^2}{8}\right\} \tag{3.18a}$$

$$A_y = \exp\left\{-\frac{k_{2\omega}^2 \cdot w_\rho^2 \left(\sin\theta\sin\varphi\right)^2}{8}\right\} \tag{3.18b}$$

$$A_z = \exp\left\{-\frac{k_{2\omega}^2 \cdot w_z^2 \left(\cos\theta - \xi\right)^2}{8}\right\} \tag{3.18c}$$

We consider again the three cases. If the sources are distributed on a 1-D line in the z direction, $A_{(1)} = A_z$. If they are distributed on a 2-D surface in the $x-z$ plane, then $A_{(2)} = A_x A_z$. Finally if they are distributed in a 3-D volume, then $A_{(3)} = A_x A_y A_z$.

Finally, the resultant SHG power emitted in the unit solid angle about Ω is:

$$P_{2\omega}(\Omega) = \frac{1}{2} n_{2\omega} \varepsilon_0 c r^2 \left|\vec{E}_{2\omega}(\Omega)\right|^2 \tag{3.19}$$

The total radiated power is obtained by integration over all angles. To proceed further with this analysis, one should decide between the three possible geometries. Moreover, the type of the molecular asymmetry and the way in that the molecules are globally organized are crucial for the determination of the parameter $\langle\beta\rangle$ in eq. (3.13), which is the starting point. In the next paragraph, we will show that this determination is possible for exogenous chromophores, grafted in cellular membranes. Their distribution is described pretty well by the second geometry (surfacial distribution). On the contrary, in another paragraph we will show that this determination is not trivial for endogenous structural proteins, such as collagen. The distribution of the structural proteins resembles more with the third geometry (volume distribution).

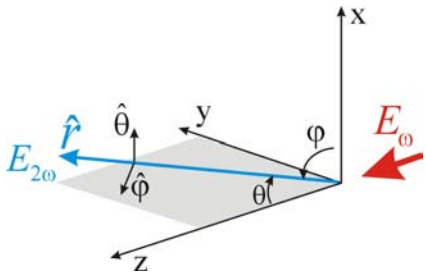

Figure 3.5 Coordinate system. Excitation beam propagates in z direction. SHG propagates in r direction, defined by $\{\theta,\varphi\}$. $\hat{\theta}$ and $\hat{\varphi}$ are the p and s polarization directions respectively.

In the above analysis, it was considered that the phases of the excitation beam are well-correlated to each other during its propagation. However, this is true only for limited distances

within a nonlinear material like biological tissues. The maximum distance, where the phases can be considered well-correlated, and thus SHG can emerge through constructive interference between the molecules, is called *coherence length*. For tissues, in general, coherence length is on the order of $20\,\mu m$ [64]. However, this length is much greater than the axial beam waist w_z of focused beams used in laser scanning SHG imaging. Thus, SHG signal emerges from an area with dimensions much smaller than the coherence length of the laser beam, and no further considerations are necessary on this matter.

3. EXOGENOUS SHG

This paragraph describes SHG, arising from exogenous chromophores incorporated in biological systems. As described in the first paragraph of this chapter, the simplest and most common form of molecular asymmetry is that exhibited by "push-pull" molecules. Most exogenous chromophores, incorporated in biophysical studies are "push-pull" in design. Among them GFP is a characteristic example as it will be shown in *chapter 4*.

A push-pull molecule comprises donor and acceptor moieties spanned by a uniaxial charge transfer path, known as cojugation path. In **Figure 3.6** a molecule is depicted, that falls into the family of polyenic stilbene derivatives [65]. Its name is ASP and has the ability both to generate HRS and to produce fluorescence. As in most cases, ASP can be adequately described by a quantum two-state model, as far as the first molecular hyperpolarizability is concerned [66], since the contributions of all other states are negligible [67]. The aromatic configuration of ASP, which possesses only a small dipole moment, is shown at the top of Figure 3.6. On the contrary, the quinoid configuration of ASP, which possesses a much larger dipole moment is shown at the bottom of Figure 3.6. The change in dipole moment between these configurations is due to the global shift of all the π-electron bonds (shown as double bonds) from the donor to the acceptor ends of the molecule. In the absense of illumination the molecule resides in its ground state $|g\rangle$, which typically resembles the aromatic configuration. Upon illumination, however, the ground state is coupled to the excited state $|e\rangle$, which more closely resembles the quinoid configuration. As a result, the molecule incurs a net change in dipole moment. It is emphasized that this change in dipole moment is not the same as the oscillating dipole moment induced in the molecule at the driving optical frequency. Instead, it corresponds to the zero-frequency optical rectification alluded in Figure 3.1b. Its magnitude is both proportional to the illumination intensity and to the net difference

in dipole moments between the excited and the ground state, $\Delta\mu = \mu_e - \mu_g$. Furthermore, it is noted that $\Delta\mu$ is in general not as large a it is illustrated in Figure 3.4, because neither $|g\rangle$ is completely aromatic, nor $|e\rangle$ completely quinoid. Both of them are a linear superposition of the aromatic and the quinoid configurations [66]. Finally, it is stated that for a molecule to be capable of generating significant HRS, it must exhibit a non-zero $\Delta\mu$ as large as possible. In [66], the following relation is provided: $\beta = \frac{6\mu_{eg}^2 \Delta\mu}{E_{eg}^2}$, where μ_{eg} is the transition dipole, and E_{eg} is the transition energy between the ground and the excited state. $\Delta\mu$ may therefore regarded as an approximate measure of a molecule's asymmetry, which is indispensible for HRS. The first molecular hyperpolarizability β, which is the origin of HRS, is proportional to $\Delta\mu$. Although β is theoretically a tensor containing 27 elements, it is actually unidimensional and its direction lies along the axis of the conjugation path.

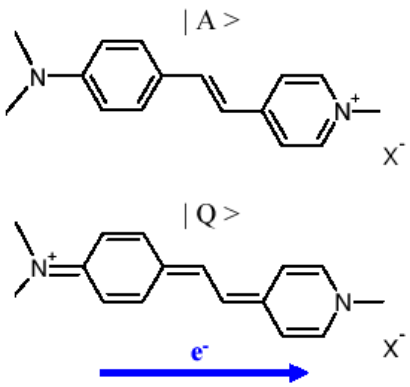

Figure 3.6 A polyenic stilbene derivative in its aromatic (top) and quinoid (bottom) configurations. There is a net change in dipole moment between both configurations.

As it has already been mentioned, σ_{SHG} is much smaller than σ_{TPEF} even for the best push-pull chromophores. To obtain SHG signals comparable to those found in TPEF microscopy, the chromophores must design in a way that allows them to be organized with relatively high number densities and high degrees of spatial alignment, as depicted in Figure 3.3b. In this example HRS becomes SHG, and the signal enhancement resulting from coherence can be fully exploited. Possible strategies for favoring molecular alignment include poling with an electric field [65,68]. A different and very interesting strategy for biophysical applications is by grafting a hydrophobic moiety onto one end of the chromophore and a hydrophilic moiety onto the other end [69]. With this structure, the chromophore has been "functionalized" to be a molecular membrane marker. When perfused onto a lipid bilayer (a cell membrane), say

from above as shown in **Figure 3.7**, the modified molecules invariably insert themselves into the membrane with the same orientation. The hydrophobic moiety tries to remain as far as possible from the aqeous surroundings, or in other words is directed into the membrane interior. The hydrophilic moiety, on the other hand, points outward, into the aqeous surroundings. Figure 3.7 depicts Di-6-ASPBS markers in a phospholipid membrane. The hydrophobic moiety constitutes from hydrocarbon sidechains, while the hydrophilic from the attached SO_3^- counterion. The basic molecule is again ASP, as it is depicted in Figure 3.6 in its aromatic configuration. Typical labeling densities used in experiments are of the order of 1 dye molecule for every 100 phospholipids.

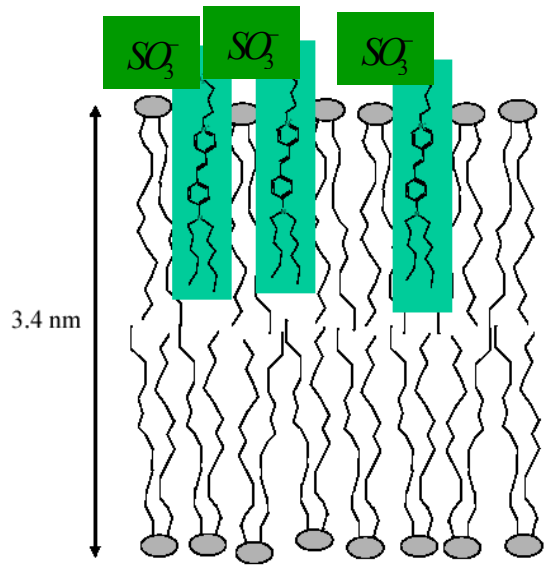

Figure 3.7 Presumptive insertion geometry of amphiphilic stilbene derivatives in a lipid bilayer, when perfused from above.

In short, with such arrangements, the desired goal of producing high labeling densities with high degree of alignment, is achieved. Such labeling configurations can produce enough SHG signal to be visualized in imaging applications. Finally, it should be noticed that this labeling configuration was well described, because in our work, a similar strategy was followed for the membrane labeling of *C. elegans'* neuronal cells. Much more will be explained about this issue in the next chapters, as well as in the experimental part of this work.

We consider, now, that a cell is illuminated by a laser beam, as it is depicted in **Figure 3.8**. Its membrane is labeled with push-pull chromophores, and the beam is focused with an objective of moderate numerical aperture (NA=0.8). The illumination is from the side, because the radiation-molecule interaction is supposed to be exclusively dipolar, and as so, it is most efficient when the principles axes of the chromophore molecules are oriented parallel to the

electric-field polarization axis of the illumination beam. The SHG active area is given by eq. (3.12c), and is centered at the beam focus. Any SHG generated outside this area may be safely neglected. The SHG from the focused beam instead of propagating on-axis as in Figure 3.4, propagates off-axis in two well-defined symmetric lobes. This may be explained again by phase-matching. Because the phase of the excitation beam has effectively been retarded near the focal center, its effective axial momentum has accordingly been decreased and may be written as ξk_ω, instead of k_ω. The latter is implied from the description of the beam, given from eq. (3.11). As before the momentum of SHG is $k_{2\omega}$. Momentum conservation along the axial direction forces SHG to propagate at an off-axis angle given by: $\theta = \pm\cos^{-1}(\xi)$.

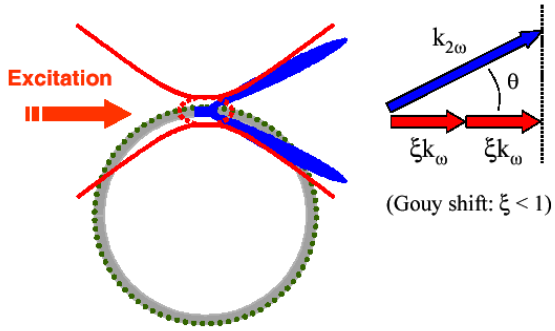

Figure 3.8 SHG from a labeled membrane when illuminated by a focused laser beam. The active SHG area is confined near the focal center. SHG propagates off-axis because of momentum conservation, taking into account the Gouy phase slippage.

The latter conclusion can be derived in a more consistent way, following the analysis presented in Box 3.3, and taking into consideration the uniaxial hyperpolarizability of the push-pull chromophores grafted onto the membrane, as well as their total alignment at the active SHG area. Conclusions for the total SHG emitted power can be extracted as well. In Box 3.4, the basic steps for these derivations are presented synoptically [59].

BOX 3.4: Surfacial distribution of molecules – Directionality and total emitted SHG power

We consider a uniform planar distribution of uniaxial push-pull molecules in the plane $x-z$, with their axis oriented in the x axis. In this case, the only nonzero component of the molecular first hyperpolarizability is β_{xxx}. Moreover, we consider that the driving field is also polarized in the $\hat{x}$ direction. Eq. (3.13) takes the form:

$$\vec{\mu}_{2\omega}(0,0,0) = \frac{1}{2}\beta_{xxx}E_\omega^2\hat{x} \tag{3.20}$$

which again is the induced dipole moment per unit molecular surface density, at the focal center. Since the quantity $\vec{\mu}_{2\omega}(0,0,0)$ is known, $\vec{E}_{2\omega}(\Omega)$ can be determined through eq. (3.15), (3.16) and (3.17). Finally,

$P_{2\omega}(\Omega)$ can be obtained through eq. (3.19) and the total radiated power is then obtained by integrating $P_{2\omega}(\Omega)$ over all angles. In [59] it is found analytically that the integrated total power (in $photons/\sec$) is:

$$P_{SHG} = \frac{1}{2}\Theta_x N^2 \sigma_{SHG} I^2 \tag{3.21}$$

where I_ω is the intensity of the excitation beam at the focal center and $N = N_{(2)}V_{(2)}$, is the total number of molecules confined in the SHG active area, which is given by eq. (3.12b). Θ_x is a parameter which will be defined immediately. Eq. (3.21) is explained as follows: As eq. (3.6) implies, the product $\frac{1}{2}\sigma_{SHG} I^2$ describes the total power emitted by a single molecule-radiator, located at the focal center. This power is emitted equally in the forward and the backward directions. If we assume that N such molecules are located exactly at the focal center, their excitation would be in phase, and their radiated fields would be coherently summed. In this case the total radiated power would be $\frac{1}{2}N^2\sigma_{SHG} I^2$, and would also be emitted equally in the forward and the backward directions. However, since the molecules are not located at the focal center, but they are uniformly distributed within the SHG active area, a corrective factor Θ_x must be added in the formula for the total emitted power. This corrective factor for the case we study is given by:

$$\Theta_x = \frac{3}{8\pi}\int A_{(2)}^2(\Omega)\left[1-\sin^2\theta\cos^2\varphi\right]\sin\theta d\theta d\varphi \tag{3.22}$$

where $A_{(2)} = A_x A_z$,and A_x and A_z are provided by eq. (3.18a) and (3.18c).

The angular pattern of the radiated SHG light is governed mainly by the function $A_{(2)}(\Omega)$. By inspection of eq. (3.18c), it is clear that A_z, and accordingly $A_{(2)}$ is maximized when $\theta = \pm\cos^{-1}(\xi)$. Thus, the SHG power is emitted in two well-defined lobes, and we came to the same conclusion as we did using momentum conservation arguments. It can be shown that the angular spread between the outgoing lobes 2θ, is roughly $1/\sqrt{2}$ that of the incoming excitation beam.

In the previous paragraph, it was described that the SHG signal arising from a uniformly distributed collection of molecules, when it is excited by a collimated beam, propagates on axis in the forward direction. In this paragraph, it was described that the SHG signal arising from the same collection of molecules, when it is excited by a focused beam, propagates off-axis in two well-defined lobes, but also in the forward direction. However, there can be cases where, a great amount of the radiated SHG power is emitted in the backward direction. These are cases, where the molecules-radiators are not uniformly distributed inside the SHG active area, but the molecular distribution possesses an axial periodicity. Particularly, if the periodicity is in the vicinity of $\lambda/4$, where λ is the excitation wavelength in the sample

medium, then up to 25% of the SHG power is radiated in backward directed lobes [70]. One can imagine that a grating is formed inside the sample, due to this periodic arrangement of the molecules, resulting in the backward propagation of the generated second-harmonic signal. For the purposes of this work, however, the assumption of the uniform distribution of the molecules is adapted. Thus, the SHG signal is considered to propagate in its great majority forwards, and the detection system in our SHG microscope, is localized in this direction.

4. ENDOGENOUS SHG

This paragraph describes SHG arising from endogenous tissue structures in biological specimen. Historically, biological SHG microscopy originated with the visualization of such structures. The physical principle behind endogenous SHG is the same as in exogenous SHG, meaning that in both cases a local asymmetry in the specimen along the excitation polarization direction is required. In exogenous SHG we concentrated on asymmetries involving uniaxial push-pull molecules, however, in endogenous SHG other kinds of asymmetry are mainly incorporated. These include helical geometries exhibiting “chirality”, as these geometries where identified in sugars and most amino-acids, or on a larger scale in filaments and fibrous bundles.

The organization of the most endogenous tissue structures forces us to adapt the bulk (volume) geometry, in order to properly describe endogenous SHG. Thus, the active SHG volume is provided by eq. (3.12c), since focused beams illuminate the specimens. In the previous paragraph, an analysis was carried out indicating the off-axis propagation of the SHG signal in the forward direction. The analysis was adjusted to the case of 2-D distribution of molecules. In the case of a 3-D distribution, the conclusions about the radiation pattern of the SHG are very similar. For uniformly distributed asymmetric molecules within the SHG active volume, SHG propagates in the forward direction, but also off-axis, exhibiting two well-defined lobes. However, the angular spread between the outgoing lobes is smaller, and SHG is emitted closer to axis [69].

Collagen is an extracellular protein that is the main fibrous component of skin, bone, tendon, cartilage and teeth, and can be readily be imaged with SHG microscopy [71,72]. Though the physical origin of collagen’s remarkably high SHG efficiency has not been fully established, its non-centrosymmetric structure consisting of three intertwined polypeptide helices (**Figure 3.9**) plays very likely a significant role [73]. Each collagen molecule has a diameter of 1.5 nm, while collagen fibrils are typically 30 – 50 nm in diameter containing therefore 30 or so,

tightly packed molecules. Each molecule acts as an induced dipole, when it is illuminated by a laser beam. However, the direction of the induced dipole is not as clear as in the case of the uniaxial push-pull molecules, but in any case the resultant SHG signal arises from the coherent summation of the contributions originated from the individual collagen molecules. Since the diameter of the fibril is small compared to the typical wavelengths of the excitation beams, the collagen molecules contained in a single fibril can be considered to be excited in phase to each other. That means that the SHG signal originated from a single fibril has not a predominant propagation direction (forward or backward). However, collagen fibrils in tissue are typically not closely packed, but spaced in a loose array, so that a large number of fibrils are contained in the SHG active volume of a focused laser beam, with a particular disposition. Due to the large number of fibrils, contained in the active volume, the contributions from each fibril interfere constructively in the forward direction, whereas destructively in the backward direction [73].

Figure 3.9 Portion of a collagen molecule. Its right-hand triple polypeptide helix is depicted.

Apart from collagen, *actomyosin assemblies* and *microtubule-based structures* exhibit high degree of organization and can be imaged using SHG microscopy. Actomyosin assemblies are the basic components of the sarcomere, i.e. of the skeletal muscle. Sarcomere is composed

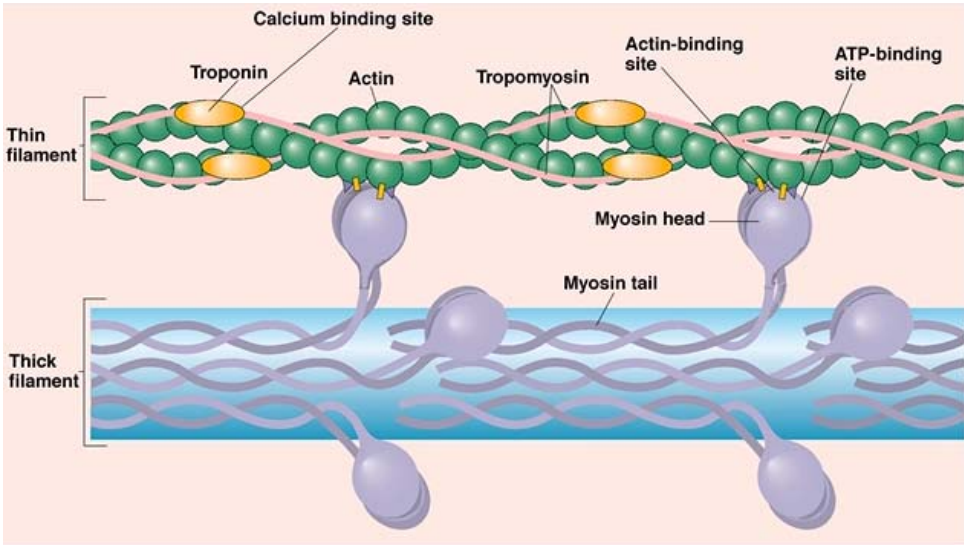

Figure 3.10 Cross-bridge formation in muscle contraction. The bridged actin (thin) and myosin (thick) filaments are referred to as actomyosin assemblies. They exhibit particular SHG efficiency.

from myofibrils, which in turn are composed from thin and thick filaments. The thin filaments consist mainly of the protein actin, while the thick of the protein myosin. Muscular contraction, occurs due to the movement of the myosin filement over the actin filament. Actually, the successive binding of myosin from the molecules of actin, provokes the movement of myosin over actin. The way in which the cross-bridge between actin and myosin occurs in muscle contraction, is depicted in **Figure 3.10**. Actomyosin assemblies are consisted of coiled-coil multiple helices and have a characteristic asymmetry, leading to SHG efficiency [74,75]. In our work, SHG originated from actomyosin assemblies in *C. elegans*, plays a central role. Owing to that, these assemblies will be refered further in the experimental part of this work.

Microtubule-based structures, on the other hand, do not consist of coiled-coil multiple helices, they exhibit, however, a characteristic asymmetry, and are efficient for SHG [76]. Microtubules are formed from two protein groups: α-tubulin and β-tubulin. Centrosomes are representative well-organized microtubule structures. In *C. elegans*, centrosomes in early embryonic cells have been imaged by SHG [74].

5. TPEF – SHG MICROSCOPY – APPLICATIONS

TPEF and SHG are nonlinear phenomena upon which laser-scanning imaging techniques are based. A focused laser beam scans the sample, and provokes either TPEF or SHG (or usually both), from a restricted region around the focal point of the beam. It has been already discussed that the TPEF and the SHG active volumes may be defined identically, due to their identical quadratical dependence on excitation intensity. Hence, TPEF and SHG intrinsically provide the same spatial resolutions, and can be combined, as contrast mechanisms, in a single microscope. In many cases, the information offered by TPEF and SHG is complementary, as it will be depicted later. **Figure 3.11** illustrates the main components of a combined TPEF-SHG microscope. In Figure 3.11 the laser focal spot is scanned in three dimensions. Scanning in $x-y$ axes provides the mapping of the sample, while scanning in z axis, provides the image sectioning of the sample, without the need of its physical sectioning. Precondition for the image sectioning is, however, the large penetration depth of the laser beam, which is ensured by the fact that its wavelength lies in the IR spectrum.

TPEF is detected in the backward, while SHG in the forward direction. A beam-splitter and filters are used for the discrimination of the signals, and for blocking the undesirable ones.

TPEF propagates equally in both backward and forward directions, hence it is convenient to detect it in the backward direction. By contrast, SHG propagates almost exclusively (when the molecules are uniformly distributed within the active volume) in the forward direction, hence it is a necessity to be detected forwards. At this point, some preconditions and considerations should be refered. The forward detection of the SHG signal is feasible only in relatively thin samples. SHG lies in the visible spectrum, hence it suffers from absorption and scattering within the biological specimen. Thick tissue SHG imaging is precluded in the forward direction. For thick tissue imaging, SHG microscopy using backward directed signal detection has also been demonstrated [77]. This is seemingly opposed to the forward propagation analysis for the SHG signal. However, it is not. The SHG signal is initially forward directed, and subsequently is re-routed in the backward direction, either by reflection from internal sample structures or by multiple scattering if the sample is diffusive. Also in the case of thin samples (like *C. elegans*), where the forward detection is convenient, a portion of the signal propagates backwards, because of either multiple scattering or reflection. More about this consideration will be discussed in the experimental part.

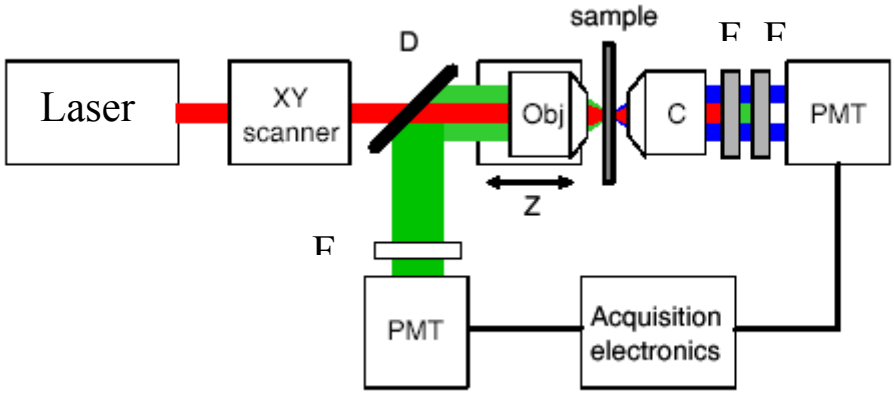

Figure 3.11 A combined scanning TPEF-SHG microscope. A pulsed laser beam (red) is focused into a thin sample. The TPEF (green) is collected in the backward direction using a dichroic beam-splitter. SHG (blue) is collected in the forward direction , after blocking both transmitted laser light and fluorescence.

TPEF signal is directed in equal portions in the forward and the backward directions. Although filters are located in the forward direction in order to block the TPEF signal, a simple technique is used for ensuring the proper discrimination of TPEF and SHG. This technique is based on the distinct spectral characteristics of the TPEF and the SHG signals. Up to now, in the presented analysis, the fundamental laser beam was considered to have a single frequency ω. This consideration is simplistic. Pulse-lasers with ultra-short pulse width have a very wide spectral bandwidth, since the temporal duration of the pulse is inversely

proportional to the spectral bandwidth. The frequency ω refers now to the central wavelength of the peak intensity. The intensity spectrum of a laser is the representation of the laser intensity I as a function of the wavelength. For typical femtosecond lasers with pulse duration on the order of 200 *fs* , the bandwidth at Full Width at Half Maximum (FWHM) is on the order of 10 *nm* . For the SHG signal, the wavelength of the peak intensity is equal to half that of the excitation beam, and its linewidth equals to $1/\sqrt{2}$ that of the excitation beam, i.e. for a laser beam with a bandwith of 10 *nm* , the SHG signal has a bandwidth of about 7 *nm* at FWHM. In **BOX 3.5** the above statement is documented.

BOX 3.5: Spectrum of the SHG

The intensity spectrum of the fundamental beam is supposed to have a Gaussian distribution around the wavelength λ_1:

$$I_{\omega} \quad \text{ex} \quad \left\{ \frac{(\lambda \quad \lambda_1)^2}{K^2} \right\} \tag{3.23}$$

According to the definition of the FWHM, this parameter is given by:

$$\left(\qquad \right) \tag{3.24}$$

Since $I_{\omega} \quad I_{\omega}$, the intensity spectrum of the SHG signal arises from the latter quadratic dependence with a wavelength shift from the central wavelength for the fundamental beam to the central wavelength for the SHG signal. We write the intensity spectrum of the SHG signal, normalized to unit for λ_2:

(3.25)

Using again the definition of FWHM, we find for the SHG signal:

$$\left(\qquad \right) \quad \sqrt{} \tag{3.26}$$

Combining eq. (3.24) and (3.26), it is obtained:

$$\left(FWHM\right) \quad = \frac{1}{\sqrt{2}} \left(FWH \quad \right)_{\omega} \tag{3.27}$$

The spectrum of the SHG differs fundamentally from that of TPEF, whose wavelength and linewidth depend mainly on the chromophore molecules, and not on the excitation laser. Moreover, the linewidth of TPEF is much larger (about an order of magnitude). For example, **Figure 3.12** illustrates an emission spectrum produced by a cellular membrane uniformly

labeled with Di-6-ASPBS [69]. Two identifiable signals are apparent. The leftmost peak is the SHG signal, centered at half the excitation wavelength ($880\,nm$ - Ti:sapphire Laser). The rightmost lobe is the simultaneously generated TPEF signal. If the excitation beam was tuned to a new wavelength, the SHG peak would track this new wavelength, whereas the TPEF lobe would not. Usually, in combined TPEF-SHG microscopy, when possible, the excitation been is tuned so that the TPEF and SHG signals are widely disparate in wavelength and do not overlap. However, in our work the laser source was not tunable, with emission peak at $1028\,nm$, leading to an overlap between the SHG signal (peak at $514\,nm$), and the fluorescence generated by GFP. Despite this difficulty, the identification of the SHG signal was easy, by the abrupt reduction of the signal level within a few nm, due to the narrow bandwidth of SHG. More on this matter will be discussed in the experimental part of the work.

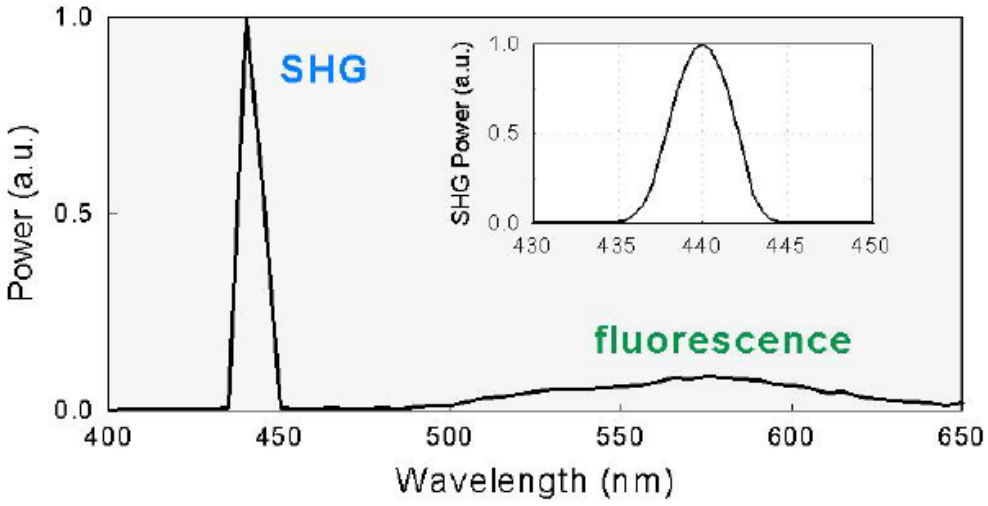

Figure 3.12 Emission spectrum obtained from a Di-6-ASPBS labeled membrane illuminated by a laser of wavelength at $880\,nm$. The leftmost peak is SHG, while the rightmost lobe is TPEF. In the inset, the same SHG peak is shown in magnification.

It has already been noted that TPEF and SHG when combined in a single microscope, can reveal complementary information. As a general principle, it can be said that TPEF gives information about the concentration of chromophores within biological specimens, while SHG provides information about the global orientation of the chromophores. This principle arises from the coherent character of SHG, which is absent in TPEF. As an example, **Figure 3.13** depicts two images of an isolated neuron from the mouse neocortex, labeled with an amphiphilic stilbene derivative [69]. Though the dye is meant to label the cytoplasmic membrane only, it has also been incorporated into the cell body, as it is apparent from the

TPEF image. The mechanisms responsible for this incorporation have not fully identified. It is noted that dye molecules inside the cell cytoplasm are randomly oriented in general, and hence cannot produce SHG. SHG imaging is therefore insensitive to intracellular dye incorporation, and reveals only outer cell membranes with exceptionally high contrast. On the contrary, TPEF is not subject to symmetry constraints, and TPEF imaging reveals the dyes molecules in the cell body as well.

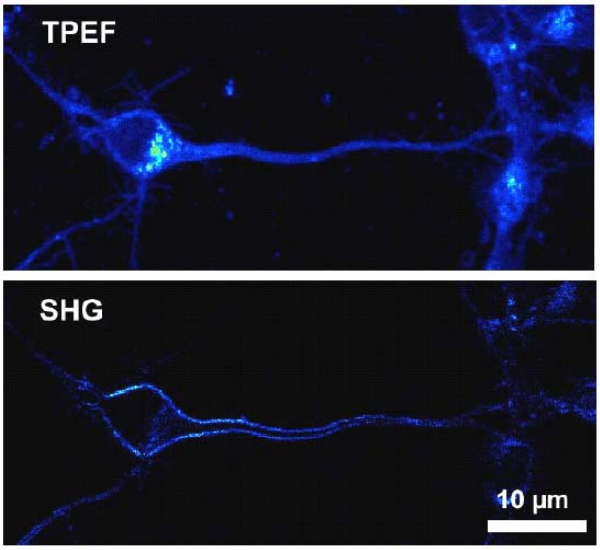

Figure 3.13 Isolated neuron labeled with a stilbene derivative, in primary cell culture from the mouse neocortex. Simultaneous TPEF (top) and SHG (bottom) images (Images from [69]).

In *chapter 2*, some of the biophysical applications of TPEF microscopy were described. In this paragraph some of the basic applications of SHG microscopy are senteniously presented. It is noted that the applications are still being discovered, because SHG microscopy is not yet a mature field. As far as the endogenous SHG is concerned, three-dimensional imaging of tissues is the main application, since optical sectioning is achieved, without the need of physical sectioning. Tissue imaging suggests the imaging of structural proteins within the tissue. As it has been noted, the most important structural protein of the animal body is collagen, which exhibits SHG efficiency. Hence, a lot of studies with practical significance in medicine and biology have been made concerning collagen. As examples, we refer the dynamic imaging of collagen and its modulation in tumors in vivo [78], as well as the development of a sensitive test for liver cirrhosis [73]. In **Figure 3.14** a projection of 3-D SHG datasets of human endometrium is illustrated. The pattern of collagen fibrils around a mucus gland is apparent [73].

As far as the exogenous SHG is concerned, the main applications are the study of the molecular "flip-flop" dynamics in membranes [69,79], the measurements of inter-membrane separation [80], and the measurements of membrane potential. As "flip-flop" it is defined, the passing of a chromophore from one to the other leaflet of a membrane. Although the energy barrier opposing such a passing is high, "flip-flop" occurs with some specific rates. Combined TPEF and SHG microscopy studies the dynamics of these passings. The measurements of inter-membrane separation are based on the coherent character of SHG. When the separation of the two membranes is optimum the SHG signals from the molecules, grafted on each membrane, interfere constructively. At smaller or larger distances, the two signals do not interfere ideally. When the separation is zero, the signals interfere destructively, and when the separation is very large, the two membranes are imaged independently. Finally, the techniques for the membrane potential measurements are of special interest for us, and will be presented separately in *chapter 5*. The work presented here, has the long-term goal to visualize the membrane potential of specific neurons of *C. elegans*, through the detection of SHG signals.

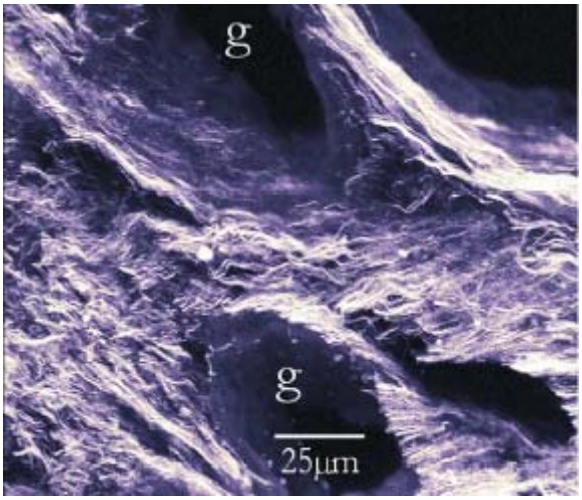

Figure 3.14 Projection of 3-D SHG datasets of human endometrium. The pattern of collagen fibrils around a mucus gland (g) is apparent (from reference [73]).

1. INTRODUCTION

Green Fluorescent Protein (GFP) is the extrinsic fluorophore used in our work and the main source of the TPEF signal, detected from our system. Hence, a brief presentation of GFP is necessary at this point.

GFP was initially discovered in 1962 by Shimomura and colleagues, from the jellyfish *Aequorea Victoria*, during their study of aequorin, a $Ca2^{+}$-activated chemiluminescent protein [81]. In **Figure 4.1** a photograph of the jellyfish *Aequorea Victoria* is depicted. *Aequorin* emits its chemiluminescence at $470\,nm$, which excites GFP. After an energy transfer, GFP emits its fluorescence at $508\,nm$.

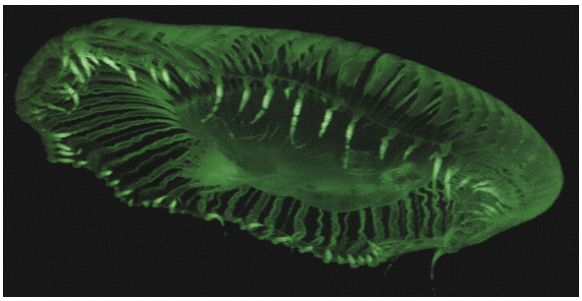

Figure 4.1 Photograph of the jellyfish *Aequorea Victoria*.

GFP gained widespread attention in the early 1990s, after it was discovered that GFP can be produced and expressed heterogeneously in a wide variety of cells/organisms. The expression results in fluorescence in targeted cells/organisms without any cofactors, as long as there is excitation light. For example, it has been shown that GFPs have been widely expressed in many organisms, including transgenic mice [82], *Xenopus laevi* oocytes [83], *Danio rario* (Zebrafish) *[84], Drosophila melanogaster [85], E. coli* [86], bacteriophage [87], viruses [88], and *C. elegans* [12,86,89].

The primary structure of *Aequorea Victoria* GFP has been decoded [90]. It is a protein of 238 amino-acids with a molecular weight of 27 or 30 kDa, and is an exceptionally stable protein concerning variations of *ph* and temperature [91]. Its extraordinary stability is a consequence of its compact tertiary structure. In **Figure 4.2** this structure is illustrated. GFP is the representative of a new protein *fold*, which have been named as *beta-can* [92]. On the outside, 11 antiparallel beta strands (green) form a very compact cylinder. Inside this beta-structure there is an alpha-helix (dark blue), in the middle of which is located the chromophore (red). There are also short helical segments (light blue) on the end of the can. The cylinder has a diameter of about 30 Å and a length of about 40 Å. The very compact single-domain structure with the chromophore centrally located in the molecule and protected from bulk solvent can

explain a number of characteristics of GFP, such as the high quantum yield of fluorescence (0.72-0.85) and the inability of oxygen to quench the excited state [93].

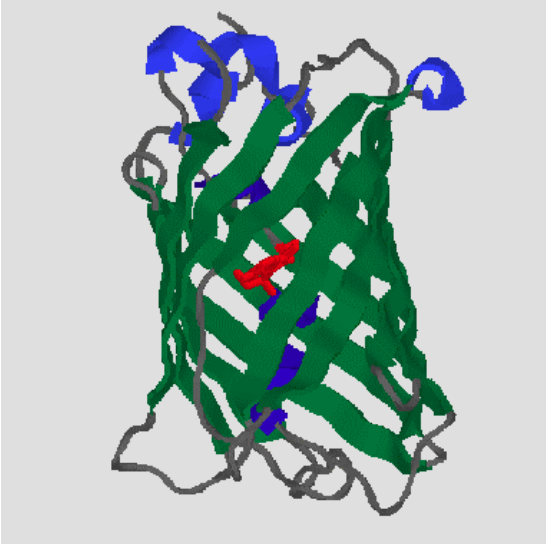

Figure 4.2 Tertiary structure of *Aequorea Victoria* GFP. On the outside, 11 antiparallel beta strands (green) form a very compact cylinder. Inside this beta-structure there is an alpha-helix (dark blue), in the middle of which is the chromophore (red). There are also short helical segments (light blue) on the end of the can.

2. CHROMOPHORE OF GFP

GFP is unique among fluorescent proteins in that its chromophore is not a separately synthesized prostethic group but composed of modified amino-acid residues within the polypeptide chain. The chromophore is positioned in an orientation that is close to perpendicular to the axis of the cylinder. The chromophore itself is a p-hydroxybenzylidene-imidazolidone. It consists of residues 65-67 (Ser - *dehydro*Tyr - Gly) of the protein. The cyclized backbone of these residues forms the imidazolidone ring. In **Figure 4.3** the initial amino-acids, as well as the biosynthetic scheme of the chromophore, are depicted. Although the amino-acid sequence (Ser-Tyr-Gly) can be found in a number of other proteins as well, it is neither cyclized in any of these, nor is the Tyrosine oxidized, nor are these proteins fluorescent. This implies that the tendency to form such a chromophore is not a intrinsic property of this tripeptide.

When the neutral phenol group of the chromophore, depicted in Figure 4.3c, is deprotonated, the phenol group is converted to a phenolate anion. The chromophore with the neutral phenol group has an absorption peak of 395 *nm* , whereas the chromophore with the phenolate anion has an absorption peak of 475 *nm* . In native GFP, both forms of the chromophore coexist, with the form containing the neutral phenol group to be predominant [94]. Thus, in the

absorption spectrum of the native GFP, both peaks are evident [91], as it is illustrated in **Figure 4.4**. The form of GFP with the phenol group, when illuminated and excited, turns also its phenol group to a phenolate anion. Thus, both forms of native GFP have the same excited state containing phenolate anion rather phenol group, and their emission spectra are identical, exhibiting a peak at 508 *nm* , as it is illustrated in **Figure 4.4**.

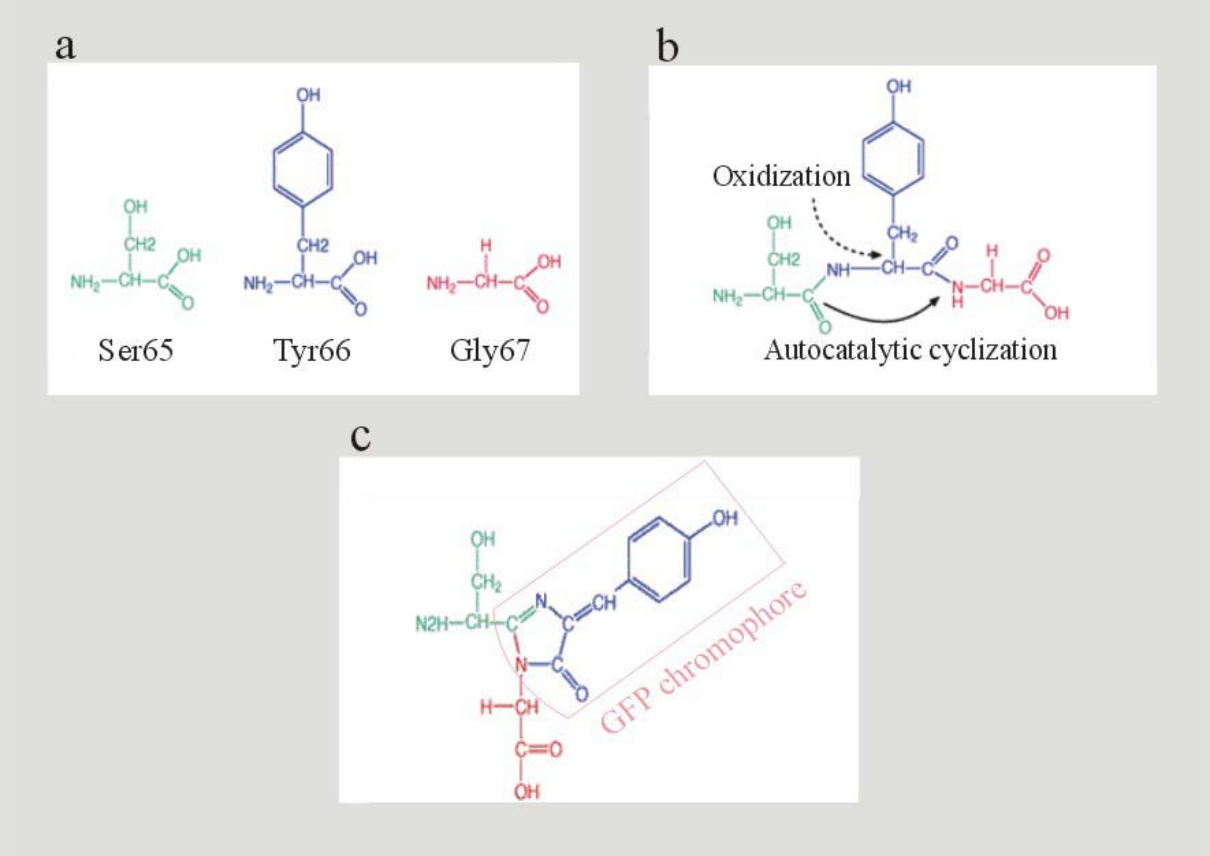

Figure 4.3 a) The chromophore of *Aequorea* GFP consists of residues 65-67 (Ser - *dehydro*Tyr - Gly) of the protein. b) The biosynthetic scheme includes the oxidization of Tyrosine and the autocatalyzed cyclization of the three amino-acids. c) The chromophore of GFP is enclosed by the pink line. It has a phenol group at one end of the molecule, conjugated to an imidazolinone group at the other.

Mutants of GFP can be devised in which all chromophores are in the phenolate form. In our work such a mutant was used, which is called S65C. Its absorption peak is at 479 *nm* and its emission peak at 507 *nm* [94]. S65C has been proved to be efficient for TPEF, although in the literature there are no values for its TPEF cross-section σ_{TPEF} .

Moreover, the chromophore of GFP has been proved to be efficient for significant Hyper-Rayleigh Scattering (HRS). Although it is not officially referred to as push-pull molecule, it has all the characteristics of the push-pull molecules, that make them HRS efficient, namely the donor and the acceptor moieties, as well as the conjugation path between them. Upon illumination, the GFP molecule undergoes significant electron redistribution, with the

phenolate anion to serve as a donor, and the imidizalinone group to serve as the acceptor. This electron redistribution results in a large induced dipole, and enables the chromophore of the GFP to produce HRS signal [12]. Unfortunately, there are no elements in the literature for its SHG cross-section, σ_{SHG}. As it has been explained in *chapter 3*, a total SHG signal is generated, only when the GFP molecules are globally aligned in the cell or generally inside the tissue they are expressed.

In the following chapter, it is described, how such an alignment can be achieved in cells, and how the SHG signal arising from the GFP molecules, may be utilized for membrane potential measurements.

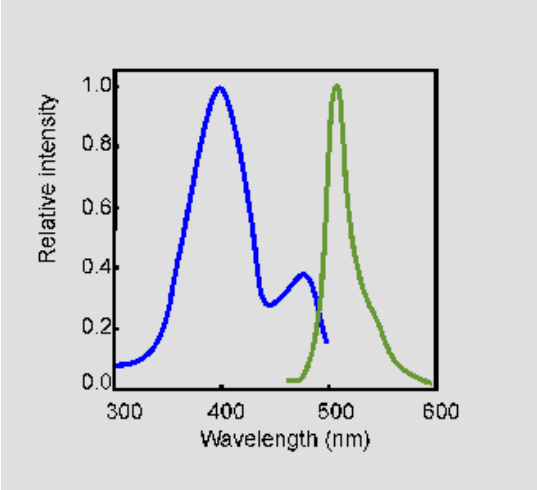

Figure 4.4 The excitation spectrum of native GFP from *Aequorea Victoria* (blue) has two excitation maxima at 395 nm and at 475 nm. The fluorescence emission spectrum (green) has a peak at 508 nm and a shoulder at 540 nm.

1. MEMBRANE POTENTIAL OF NEURONAL CELLS

A typical neuronal cell (neuron) is shown in **Figure 5.1**. Neurons, like all cells, are enclosed in a lipid bilayer, the membrane, which separates the intracellular components from the extracellular space. The concentration of ions inside the cell is different to that in the surrounding liquid. More anions are located at the inside than the outside surface, while more cations are located at the outside than the inside surface of the membrane. The difference in the concentrations generates an electrical potential (membrane potential), which plays a major role in neuronal dynamics. Neuron membrane is 2-4 nm thick, and is impermeable to most charged molecules, acting as a capacitor by separating the charges lying on either side of the membrane. However, the existence of ion channels along the neuron permits the transmission of ions from one to the other side of the cellular membrane. The way in which ion channels are distributed along the cellular membrane is depicted in **Figure 5.2**.

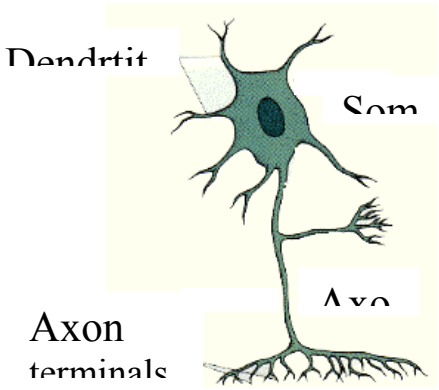

Figure 5.1 Typical neuronal cell. Its dendrites, soma, axon and axon terminals are depicted.

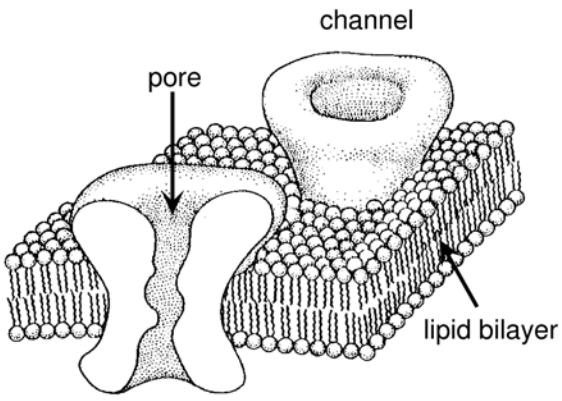

Figure 5.2 Distribution of ion channels along the cellular membrane. The transmission of ions across the membrane takes place through these ion channels.

Each ion channel is always a multiprotein complex and is formed by specific proteins, which are referred to as channel subunits. Most channels are highly selective for a particular type of ions. The membrane has also ion pumps, which expend energy to maintain the concentrations of the ions inside and outside the cell. In **Figure 5.3** a K^+ ion channel and a pump for Na^+ and K^+ ions are depicted. The exterior potential is defined to be 0 by convention. Because of excess cations at the outside surface of the membrane the resting membrane potential is negative, typically about $-60\ mV$. Resting potential is the equilibrium point, when ion flow into the cell is matched by ion flow out of cell, and describes the neuron when it is inactive.
On the contrary, when the neuron is stimulated, the membrane potential is reversed having a positive value. This reversion can be seen as a perturbation, which propagates along the neuron. In this way the neuronal signal is transmitted longitudinally on the neuronal surface and continuously to the connected neurons. The membrane depolarization of the neuronal cells is a unique property among all other cells of the multicellular organisms, from nematodes through vertebrates. The reason for the existence of this phenomenon is that neurons have to transduce stimuli produced signals, rapidly. Some specialized neurons (inner ear hair cells, mechanoreceptors) produce responses in time length of 1/20000 sec.

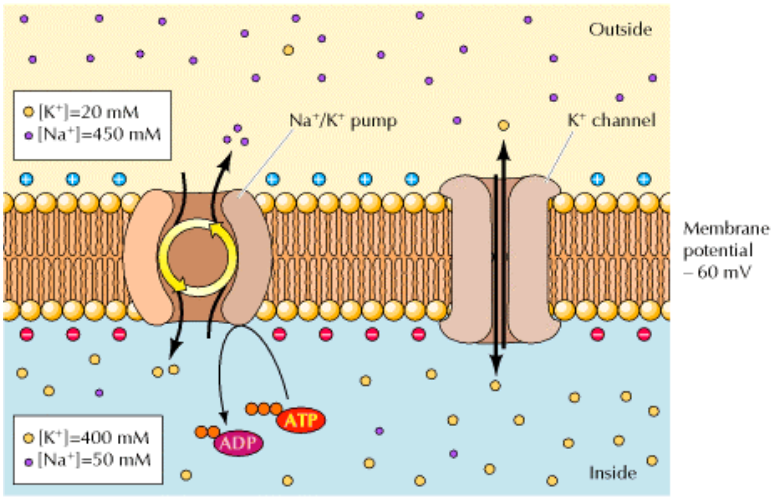

Figure 5.3 Ion channel and ion pump across the cellular membrane. The total concentrations of cations are greater at the outer surface of the membrane, resulting in a negative membrane potential of about –60 mV (the exterior potential is defined to be 0 by convention).

2. OPTICAL VISUALIZATION OF MEMBRANE POTENTIAL

The optical visualization of membrane potential with microscopic resolution has been the goal of considerable research. Presently, the most popular optical mode for monitoring membrane

potential is fluorescence. In this linear spectroscopic approach the fluorescence intensity is monitored as a function of membrane potential. It has been shown that the fluorescence intensity of a dye can be altered by membrane potential in one of three ways. First, by *a reorientational mechanism* in which a membrane-bound dye tilts in response to an electric field [95]. Second, by *a voltage-dependent redistribution mechanism* in which the fluorescent dye partitions into the membrane as a function of the electric potential [96], and third, by a *molecular electrochromic mechanism* [97,98]. The first two techniques are considered to be highly sensitive, but they are generally inadequate for imaging the fast dynamics of excitable cells, which occur on time scales of a millisecond or less. The third technique is adequate for imaging the fast dynamics, and the principle behind this technique is the following: a local electric field provokes shifts in the electronic energy levels of a molecule, known as *Stark shifts*. These shifts lead to changes in the molecular absorption or fluorescence emission wavelengths, which are monitored by techniques of ratiometric excitation or detection.

The use of SHG to monitor membrane potentials is well known [5,6]. Its advantages over the use of fluorescence has the general advantages that were mentioned for the imaging applications in *chapter 4*. Additionally we note that, unlike the case of fluorescence, in SHG the endoplasmaticaly localized molecules will not contribute to the observed signal, due to symmetry constraints. Thus, only those asymmetrically distributed molecules in the membrane will be responsible for the signal without any of the background normally seen when fluorescence is used as the probe.

Two main techniques to monitor membrane potentials, employing SHG, are used. According to the first technique an applied DC field can provoke the alignment of dipolar molecules, and SHG can provide a signature of this alignment [99,100]. However, this technique is slow, since it requires a global re-orientation (polling) of molecules. More recently, it has been demonstrated that SHG can report membrane potential much more directly by a mechanism of internal molecular charge distribution. Intuitively, one can think of an applied field as provoking a modification in the molecular charge asymmetry, discussed in *chapter 3*. Inasmuch as charge asymmetry is needed for SHG, it is expected that SHG is sensitive to an applied bilateral membrane field. The mechanism for this field response critically depends on the molecule's being charge-transfer in nature, and one finds that high SHG field sensitivity in general requires molecules exhibiting large $\Delta\mu$. Responses in molecules are fast, typically on the order of picoseconds or less, which are essentially instantaneous as far as any biological dynamics are concerned.

Unlike in the case of electrochromism where external voltage variations are identified by changes in excitation or emission wavelengths, in the case of SHG the voltage variations are identified by changes in SHG signal powers. An illustration of SHG voltage sensitivity is provided in **Figure 5.4**. Figure 5.4 depicts a Giant Uni-lamellar Vesicle (GUV) labeled with push-pull chromophores of the kind described in *chapter 3*, before and after the application of a transmembrane electric field that changes sign every image line. GUVs are single bilayer spheres roughly 10-50 μm in diameter, comparable in size to typical biological cells. One observes a corresponding increase and decrease in the resultant SHG signal power. In particular, when the membrane potential is negative, as it is the membrane potential of an inactive neuron, the SHG is increased. On the contrary, when the membrane potential is positive, as it is the membrane potential of a depolarized (stimulated) neuron, the SHG signal is decreased, due to the decrease of the asymmetry of the push-pull molecules. In this example, the relative SHG power changes by about 20% for a transmembrane potential change of 100 mV [10]. Such a voltage sensitivity is about an order of magnitude better than what is typically obtained with fluorescence techniques based on electrochromism.

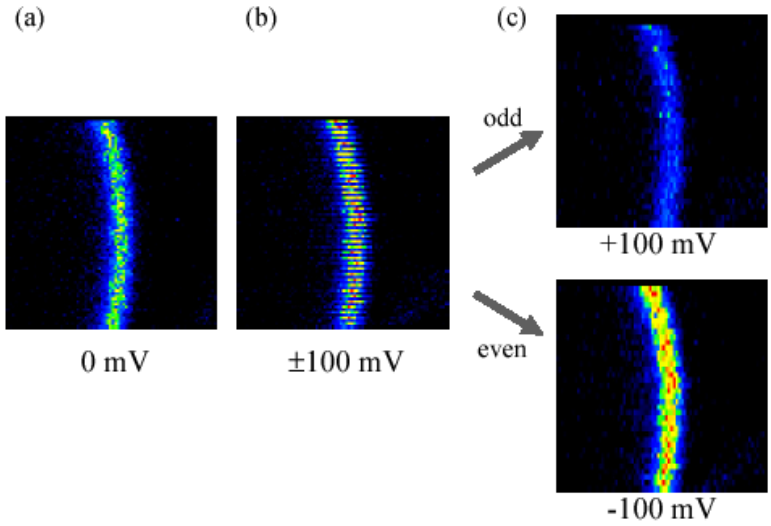

Figure 5.4 SHG images of a GUV segment labeled with a push-pull chromophore (a) before and (b) after application of a transmembrane electric field that alternates sign every image line. The field amplitude corresponds to a transmembrane voltage of about $\pm 100\ mV$. Even and odd lines are de-interlaced in (c) to better illustrate the electric field dependence of SHG.

3. GFP AS A SHG OPTICAL SENSOR OF MEMBRANE POTENTIAL

GFP has already proved its efficiency for SHG in transgenic forms of the worm *C. elegans* [8,12]. In *chapter 4*, we described the molecule of GFP, and we presented the reasons that make this chromophore efficient for high signal levels of HRS (existence of donor and acceptor moieties, as well as existence of conjugation path between them). Upon illumination, the GFP molecule undergoes significant electron redistribution, with the phenolate anion to serve as a donor, and the imidizalinone group to serve as an acceptor. This electron redistribution results in a large induced dipole, and enables the chromophore of the GFP to produce HRS signal. Thus, in order to have a sufficient total SHG signal, arising from the GFP molecules, expressed in selective sites of the worm, the global alignment of the molecules is necessary.

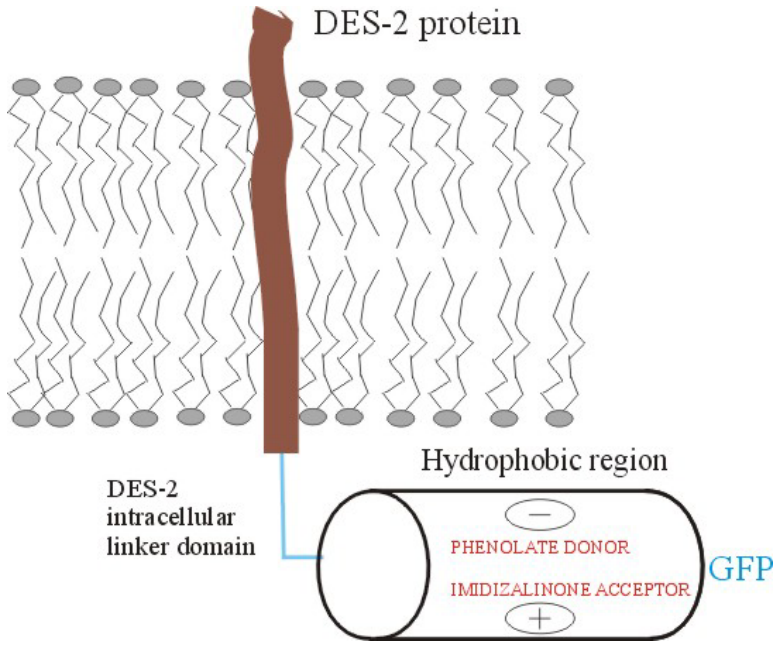

Figure 5.5 Diagrammatic representation of a hypothetical orientation of the GFP molecule attached to the DES-2 transmembrane domain by a DES-2 intra cellular linker domain in choline sensitive PVD cells of the *C. elegans* nematode.

In [12], this alignment was achieved in the following manner: The focus of the investigation was the specific neuronal cells PVD of *C. elegans*. The strain that was used, had an integrated array expressing a DES-2::GFP chimera. DES-2 is a protein, that crosses the membrane of the PVD cells, thus having mainly a transmembrane domain. The GFP molecules are positioned in the interior of the cell, and are attached to the DES-2 transmembrane domain by a DES-2 intracellular linker domain, as it is depicted in **Figure 5.5**.

There is strong evidence that the axis of the GFP chromophore is close to be perpendicular to the membrane plane across which the voltage alterations occur. Due to the fact that the axis of the chromophore is perpendicular to the cylinder that encloses the GFP molecule, this cylinder should be parallel to the membrane plane (Figure 5.5). In spite of the traditional view that a membrane field only affects components fully embedded in the membrane, and GFP is certainly not embedded in the membrane, the presence of such a field in close proximity to a redistribution of highly polarizable electrons under the action of the electromagnetic field of light, could seriously perturb the chromophore electron redistribution. Such a perturbation would alter the induced dipole and this would alter the observed SH signal which is extremely sensitive to such perturbations. Still, one point remains unclear: which side of the chromophore's conjugation path (the phenolate or the imidazolinone) is positioned close to the membrane and which one away from it. The reasons for the one or the other orientation have to do with specific regions of the β barrels that compose the cylinder of the GFP molecule. Some of these regions are more hydrophobic, and some others have a propensity for specific charges. A fully theoretical prediction can not be done, whether the donor or the acceptor group of the chromophore will be closer to the membrane plane. However, the experimental results in [12] indicate a decrease of the SHG signal, each time the membrane of the PVD cell is depolarized. Based on the above observation, it is suggested that the GFP chromophore is aligned with the "electron donating" phenolate anion closer to the membrane leaflet than the "electron accepting" imidazolinone. In this reported work [12], the depolarization of the PVD was achieved with the addition of choline, which stimulates directly the PVD cells.

1. THE NEMATODE *C. ELEGANS*

It has been strongly noted during the introduction and the first chapters of this work, that in most of our experiments the biological specimen under test was the nematode *C. elegans*. Although the nonlinear microscope that we developed can be used in a variety of studies in the field of physics, biophysics and medicine, the fusee for its development was the investigation of the molecular and physiological processes, underlying the neuronal function of *C. elegans*. For this reason, a brief presentation of the nematode is necessary.

Figure 6.1 Photograph of an adult *C. elegans*, with the use of electron scanning microscope. The length of the nematode is about 1 mm, and the width is about 80-100 μm.

C. elegans is a small (1 mm) free-living hermaphroditic nematode that completes a life cycle in 2.5 days at 25°C. A photograph of *C. elegans* is shown in **Figure 6.1**. The simple body plan and transparent nature of both the egg and the cuticle of this nematode have facilitated an exceptionally detailed developmental characterization of the animal. The complete sequence of cell divisions and the normal pattern of programmed cell deaths that occur as the fertilized egg develops into the 959-celled adult are known [101]. One considerable advantage of the *C. elegans* system is that it is the first metazoan for which the genome was sequenced to completion [13]. Investigators can take advantage of genome data to perform "reverse genetics," directly knocking out genes of interest. Mutations can be easily induced and large screens can be performed to isolate mutants having specific phenotypes. In addition, a novel method of generating mutant phenocopies, called double stranded RNA-mediated interference (RNAi), enables the translational scilensing of a particular gene (knock-down) to be rapidly

evaluated [102]. Another advantage of this system is that construction of transgenic animals is rapid; DNA injected into the hermaphrodite gonad concatamerizes and is packaged into embryos in the form of an extra chromosomal array, hundreds of which can be obtained within a few days of the injection [103]. The anatomical characterization and understanding of neuronal connectivity in *C. elegans* are unparalleled in the metazoan world. Serial section electron microscopy has identified the pattern of synaptic connections made by each of the 302 neurons of the animal (including 5000 chemical synapses, 600 gap junctions, and 2000 neuromuscular junctions), so that the full "wiring diagram" of the animal is known [114]. Although the overall number of neurons is small, 118 different neuronal classes, including many neuronal types present in mammals, can be distinguished. Other animal model systems contain many more neurons of each class (there are about 10.000 more neurons in *Drosophila* with approximately the same repertoire of neuronal types). Overall, the broad ranges of genetic and molecular techniques applicable in the *C. elegans* model system allow a unique line of investigation into fundamental problems in biology.

The coordinated function of individual *C. elegans* neurons leads to characteristic behavioral responses. Although systematic investigations have revealed important information about the neurons that participate in specific behaviors, the molecular and physiological processes underlying neuronal function remain poorly understood.

2. AIMS OF THIS WORK

In the total of the 302 neuronal cells of *C. elegans*, six (6) of them have found to constitute the touch neurons circuit, which makes *C. elegans* capable of sensing mechanical stimuli and adjusting its behavior in order to avoid the stimuli source. In **Figure 6.2,** two (2) of these six neurons are depicted. As it is clearly shown in Figure 6.2, these two neurons (namely PLML and PLMR) are located in the posterior body part of the nematode.

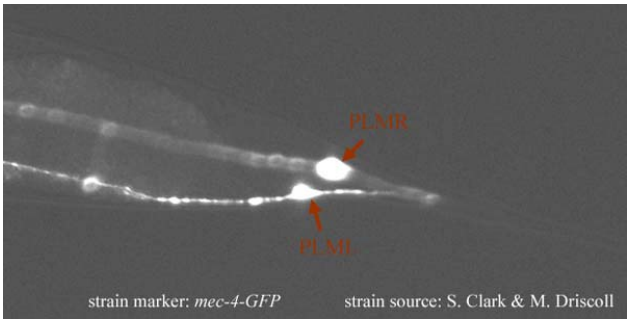

Figure 6.2 The two touch receptor neurons, localized in the posterior part of *C. elegans* are shown. Fluorescence arises from GFP molecules, attached to the transmembrane protein MEC-4.

The long-term goal of our project is the elucidation of the molecular events underlying the conversion of mechanical stimuli into chemical signals and finally biological response. Thus, we aim in the identification of all the proteins that form the mechanosensory apparatus. Genetic approaches revealed that the coordinated function of different extracellular and intracellular proteins is critical for the transduction of the mechanical stimulus into the core mechanosensitive ion channel. Although many different molecules are known to participate in the overall process, their function has never been assayed in vivo. The subunits of the core mechanosensitive ion channel are known to be the MEC-4 and the MEC-10 proteins. The contribution of these molecules in the channel formation revealed through genetic analysis of mutant strains defective in touch sensation. As it is mentioned above, the stimulation of the touch neurons by mechanical force leads to the membrane depolarization through the insertion of Na^+ cations in the cell. But which is the contribution of the rest molecules that form the mechanosensory apparatus? Are there any unidentified molecules that serve in the appropriate transduction of mechanical stimuli? We propose to develop a high resolution technique for in vivo imaging of the neuronal activity. This technique, together with the conventional molecular and genetic applications will help in the dissection of mechanotransduction process. Moreover, the application of such a technique in other neurons possess of great biological interest. Since now, the in vivo imaging of the neuronal activity has not achieved in cases where the electrophysiological techniques are not applicable. For the achievement of the long-term goal, the work plan involves: Construction of nematode strains that lack one or more proteins that possibly form the mechanosensory apparatus, as well as the ion channel. Stimulation of the nematode, and monitoring of the membrane potential of the touch neuron that is close to the touch area. Depolarizing of the neuron indicates the proper existence and functionality of the ion channel, while maintenance of the resting membrane potential indicates the opposite, and gives strong evidence for the significance of the lacking protein in the proper formation of the ion channel in the touch neurons. The basic step in the implementation of this ambitious work plan is the establishment of the membrane potential measurement technique, by monitoring the SHG signal produced by GFP molecules, attached to transmembrane proteins, as it was described in *chapter 5*.

The goals of the work presented here, which are also the mid-term goals of the project, are the following:

1. Development of a reliable scanning imaging system, using the nonlinear phenomena of TPEF and SHG.

2. Mapping of the interior part of the nematode *C. elegans*, and identification of the structures that produce SHG signal.
3. Mapping of the posterior part of the nematode, and identification of the structures that produce SHG signal. In this part, two of the touch receptor neurons are located, thus it is of great importance to know if there are endogenous structures that give strong SHG signal, making difficult the isolation and the identification of the desirable exogenous SHG signal produced by the GFP molecules.
4. Detection of the TPEF arising from the GFP molecules, and localization of the two touch neurons in the posterior part of the nematode.
5. Detection and identification of the SHG signal, produced by the GFP molecules.

In the next two chapters the experimental work and the results are presented. The results are evaluated, and proposals for the fulfillment of the unfulfilled goals are presented. Finally, the plans for the future work till the achievement of the long-term goals are described.

1. ONE-PHOTON FLUORESCENCE MEASUREMENTS

The experimental part starts from the development of a simple setup for the detection and the recording of the fluorescence signal, originating from GFP molecules, which are expressed in the pharynx of *C. elegans* strains. The reasons we make this investigation are, first, the ascertainment that the specific mutants express correctly in the right position and in high quantity GFP molecules, and second the investigation of the fluorescence emission spectrum of GFP, when properly and strongly excited. The strain of the nematode, used in these initial experiments is: IS[pmyo-2::Pes-10::GFP]. More about the strains and the sample preparation will be discussed in the following paragraphs. In **Figure 7.1**, the developed set-up for this line of experiments is depicted.

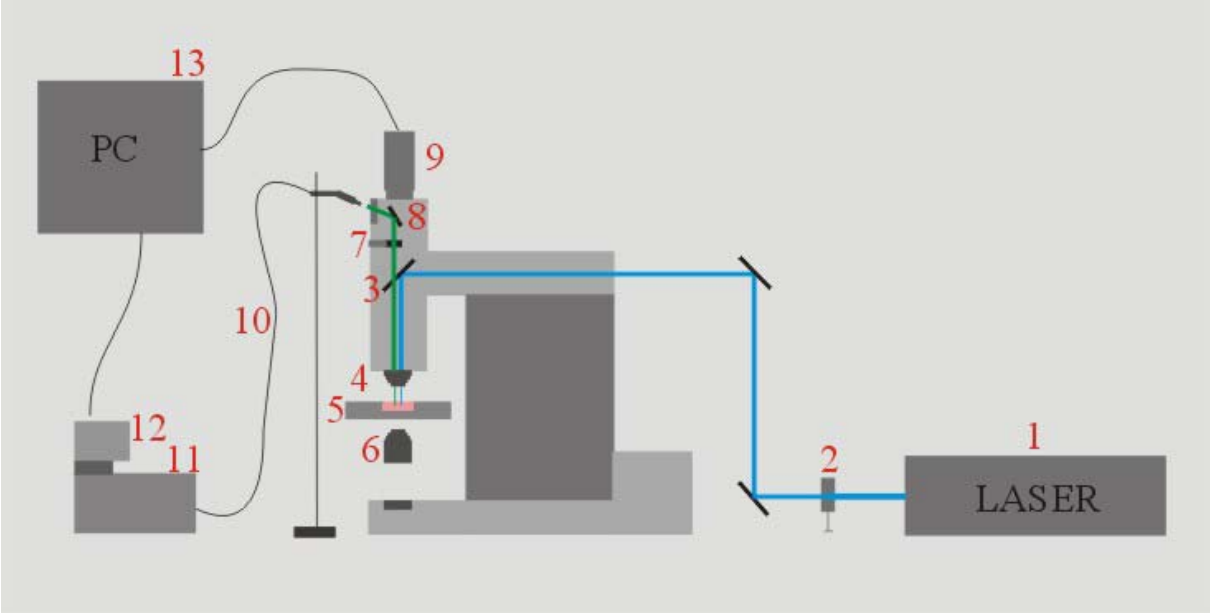

Figure 7.1 Experimental setup for one-photon fluorescence detection. 1) Argon Ion Laser (Line: 476.5 nm), 2) Attenuator, 3) Dichroic Mirror, 4) Objective Lens (50x, NA 0.8), 5) x-y-z scanning stage, 6) Condenser of the microscope, 7) High Pass Filter (490 nm CVI), 8) Flip-mount mirror, 9) CCD Camera, 10) Optical fiber, 11) Spectrograph (resolution: 1 nm), 12) Diode array – 1024 pixels, 13) PC.

The laser (1) we use is an **Argon Ion laser** (Spectra Physics-Series 2000), emitting five lines (514.5 nm, 496.5 nm, 488 nm, 476.5 nm and 457.9 nm). The used wavelength is 476.5 nm, due to its proximity to the absorption peak of the S65C mutant of GFP (479 nm). It is noted that in all the nematode strains investigated in our work, S65C mutant of GFP is expressed. The output power of the TEM_{00} mode at this wavelength is regulated to be $50\,mW$, and it is highly linearly polarized in the vertical direction (95%). The beam passes through an attenuator (2) for regulating further its power, and it is directed by means of mirrors inside the

properly modified microscope (Nikon Eclipse ME600D). It is reflected by a dichroic mirror (3 99%-800 nm), and it is focused by means of an objective lens (4 Nikon 50x, NA 0.8) onto the sample. The sample is positioned on the standard x-y-z translation stage (5) of the microscope. Part of the fluorescence is collected by the same objective, and it is directed together with the reflected laser beam in the backward direction. A small portion of the fluorescence signal is transmitted through the dichroic mirror, and the filter (7) (High Pass 490 nm CVI) positioned on the upper part of the microscope. Finally, a flip-mount mirror (8) determines whether the fluorescence signal is directed to the CCD camera (9 Sony XC-57CE) or the eye-piece of the microscope. The eye-piece has been removed, and an optical fiber probe is positioned at its place. The exact position of the optical fiber probe is regulated by another x-y-z stage, so that the collection of the fluorescence signal is optimal. The signal is waveguided inside the optical fiber (10 400 μm core-cladding diameter VS-IR) to the spectrograph (11-12 Digikrom CM110 CVI), and its spectrum is detected by a diode array consisted of 1024 pixels (AD 150 CVI). Finally, the spectrum is recorded and stored in a PC (13), connected with the spectrograph. The spectrograph was calibrated by means of a mercury lamp. Using the above set-up, the two above mentioned goals of this investigation were fulfilled.

Verification of fluorescence efficiency: In **Figure 7.2** two photos of fluorescent nematodes, taken with the CCD camera, are presented. The fluorescence of the GFP molecules, expressed in the pharynx of the worms, is easily detectable, due to the high spatial concentration of GFP molecules. The outline of the pharynx is obvious. It is mentioned that the expressed GFP molecules are diffused within the pharynx, without any preferable orientation. Thus, fixing the polarization of the exciting laser beam in a specific direction by means of birefridgent crystal plates would not be meaningful. The attenuator was regulated, so that the incident power after the objective lens was measured to be 5 mW . The power was focused to a spot of 1 μm in diameter, thus providing a high light intensity. The efficiency of the focused light to provoke one-photon fluorescence is obvious from the strong and spatially extended signal seen on the pictures of Figure 2. Three reasons are responsible for this efficiency. First, the large concentration of GFP molecules in the pharynx, second, their great absorbance and fluorescence efficiency, when they are excited in the vicinity of their peak absorbance wavelength, and mainly the nature of one-photon fluorescence, which scales only linearly with the incident light's intensity. The latter means that low light intensities, even outside the beam waist's region can provoke fluorescence in such an efficient system.

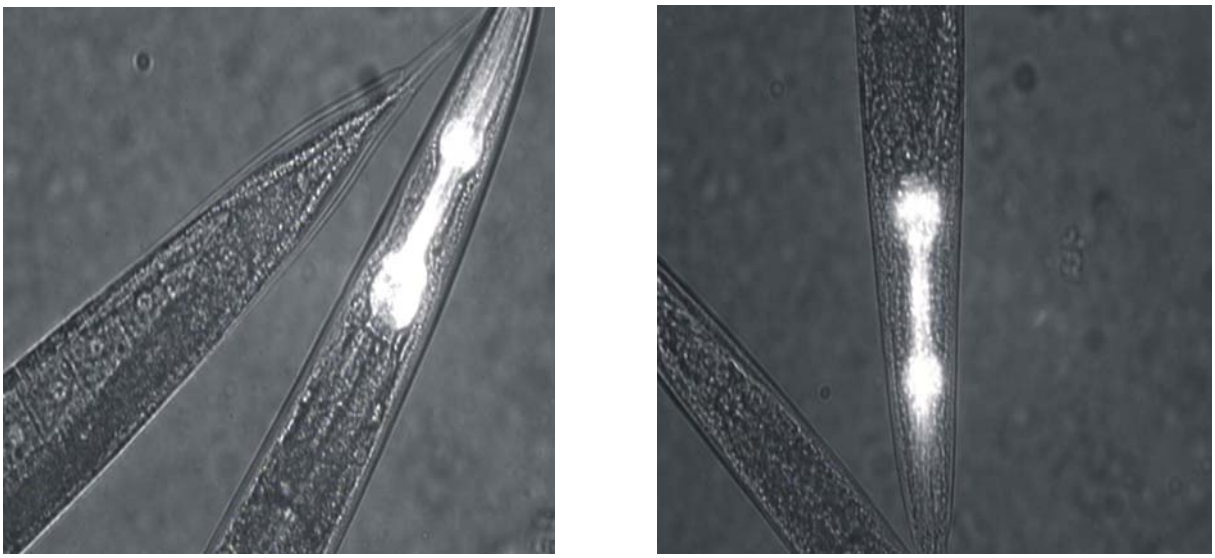

Figure 7.2 One-photon fluorescence originating from diffused GFP molecules in the pharynx of two nematodes. The excited area is very extended, due to the linear nature of one-photon fluorescence. The fluorescence is easily detectable, because of the proper excitation wavelength and the large concentration of GFP molecules inside the pharynx of these strains. Photos taken with the CCD camera on the top of the microscope.

Investigation of the fluorescence emission spectrum of the GFP mutant S65C: Focusing on the centre of the pharynx, where the fluorescence signal levels are high, we switch the flip mount mirror on the top of the microscope, so that the signal is directed now to the eye-piece, and it is coupled into the optical fibre. The signal is spectrally analyzed, and the resultant spectrum is depicted in **Figure 7.3**. A typical fluorescence emission spectrum arises with a bandwidth of more than $100\,nm$. The emission peak is found at about $508\,nm$, which has not a considerable difference from the known peak of $507\,nm$.

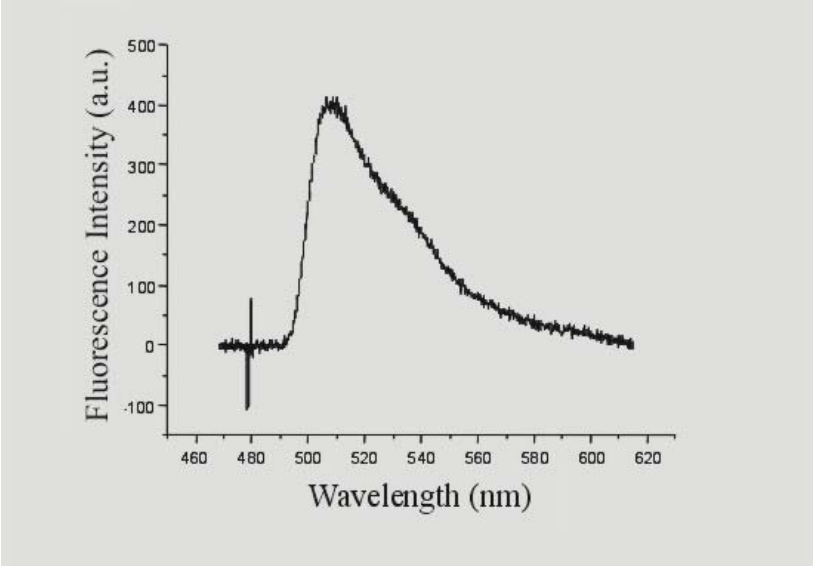

Figure 7.3 Spectral analysis of the fluorescence emission signal. The fluorescence originates from GFP mutants S65C expressed in large concentration inside the pharynx of *C.elegans* nematodes. Fluorescence is extended in more than 100 nm and its emission peak is found at about 508 nm.

2. EXPERIMENTAL SETUP FOR COMBINED TPEF-SHG SCANNING MICROSCOPY

2.1 Description of the basic components

In the present paragraph, the developed experimental setup for nonlinear imaging is presented. The description is extensive because of two reasons: First, it is the first time that a complete experimental setup for imaging using simultaneously TPEF and SHG and utilizing *fs* pulses, is built in our country. This setup gives the opportunity for investigation and research in numerous scientific fields. Second, the setup is inexpensive, compact and reliable. The optical components, that are used, including the microscope, as well as the hardware for signal acquisition and scanning processing, are inexpensive. The software for the general control of the scanning process, data acquisition and image reconstruction, has been developed by our group, considering the needs of the specific project. However, it is easily convertible and can match any specific needs of similar projects. The whole setup, apart from the PC, and the Lock-in amplifier, is positioned on an anti-vibrational, transferable optical table, providing great flexibility and availability.

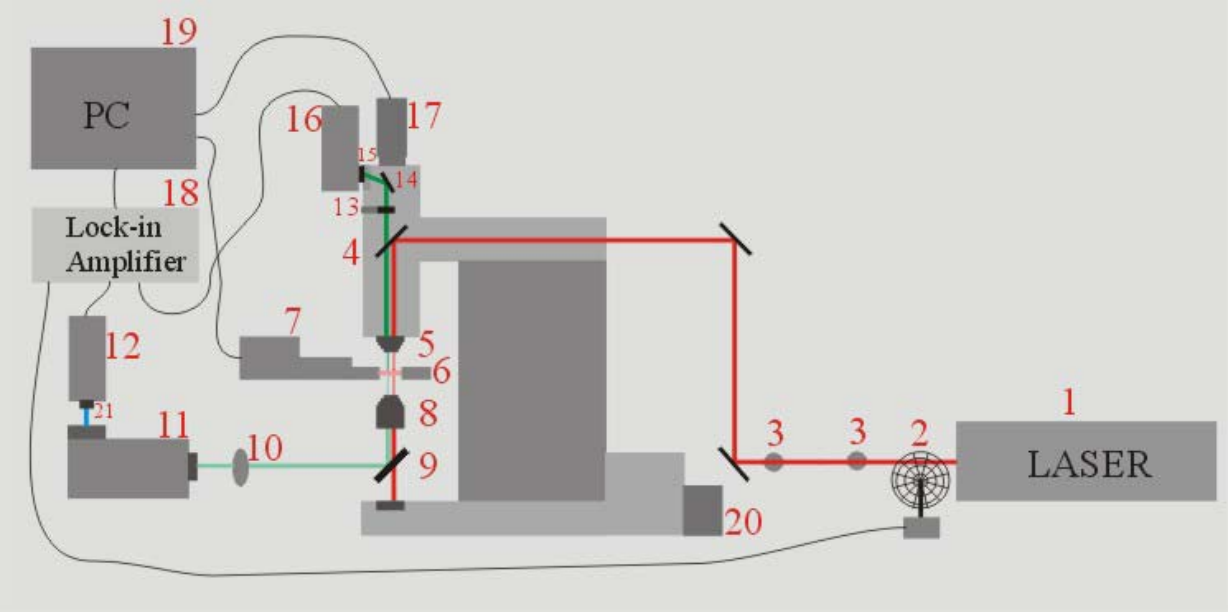

Figure 7.4 Experimental set-up for combined TPEF – SHG scanning microscopy. 1) Femtosecond laser (λ=1028 nm), 2) Chopper, 3) Iris, 4) Dichroic Mirror, 5) Objective lens, 6) Holder of the sample, 7) x-y-z motorized scanning stages, 8) Condenser lens, 9) Dichroic Mirror, 10) Focusing lens, 11) Monochromator, 12) Photo-multiplier tube (PMT), 13) Neutral density filter, 14) Flip-mount mirror, 15) Short Pass Filter, 16) PMT, 17) CCD camera, 18) Lock-in amplifier, 19) PC, 20) Light source, 21) Short Pass Filter. The SHG signal is detected in the forward direction (PMT 12), while the TPEF is detected in the backward direction (PMT 16).

In **Figure 7.4** the layout of the developed setup is depicted, and its main parts are shown. In **Figure 7.5** a photo of the same setup is presented. Its similarities in the structure philosophy with the setup depicted in Figure 3.11 is obvious. The description of the separate parts follows. It is noted that the centre of the whole setup is the same properly modified microscope (Nikon Eclipse ME600D), we used for the one-photon fluorescence experiments.

1) *Laser*: we use as excitation source a diode pumped, femtosecond t-pulse laser (Amplitude Systemes product - high power femtosecond oscillator). The average output power is specified by the manufacturer to be 1 Watt, and it is characterized by long-term stability. The long-term stability of the laser after the warm-up process was verified during our experiments, since the output power remained stable all day long, almost every single day. The pulse duration is 180-200 fs and the repetition rate is 50 MHz. Using the above specifications, the energy of the single pulse is calculated to be 20 nJ. This amount of energy limited in 200 fs is extremely high and provides high efficiency of exciting nonlinear phenomena. The spectrum of the laser was monitored, by coupling the output beam into an optical fiber and guiding it to a spectrograph. This spectrum is depicted in **Figure 7.6**. The FWHM is ~6 nm, and the central wavelength λ_o is 1028 nm. However, the value of the central wavelength did not remain constant during the whole experimental period, and shifts of about ± 2 nm occurred. These shifts are attributed, first, to fluctuations of the temperature in the lab's room, and second to small misalignments of the optical components inside the laser box. The output laser light is highly linearly polarized (99%).

2) *Chopper*: The beam passes through the chopper, and the chopper attributes to the beam a frequency (modulation), that is regulated to be 1470-1480 Hz. The use of the chopper is related with the detection of the TPEF and the SHG signal from the photomultipliers and the recognition of these signals from the Lock-in amplifier. The importance of the beam's modulation in the operation of the Lock-in amplifier will be described in the corresponding paragraph.

3) *Iris*: Two ires are used before the microscope. They help the quick alignment, and they provide an easy way to adjust the diameter and the power of the fundamental beam.

4) *Dichroic Mirror*: A dichroic mirror (99 % reflectivity at 1000 nm) directs the fundamental beam down to the objective lens. Moreover, the reflected fundamental beam is reflected back to the laser, and is prevented from reaching the CCD camera or the eye-piece port.

5) *Objective Lens*: The objective lens offers the tight focusing of the fundamental beam onto the sample. Simultaneously, it collects the TPEF originating from the sample in the backward

direction, and collimates this signal, which is directed to the PMT at the top of the microscope. Two objective lenses are used in our experiments. a) Nikon (50x, NA 0.8, working distance: 0.54 mm), and b) oil matched Edmund Scientific (100x, NA 1.25, working distance: 0.23 mm).

6) *Sample holder*: The biological sample is mounted between two cyclic glass slides. The thickness of each glass slide is 50-70 μm. These were the thinnest commercially available glass slides. The need for a thin slide originates from the short working distance of both the objective lenses, available to us. If the upper glass slide was too thick, the fundamental laser beam would be focused inside the glass region and not in the region of the sample. The sample is mounted between two glass slides, so that a possible contact with the objective lens is avoided. The slides are positioned at a special holder, constructed at the workshop of FO.R.T.H. This holder is connected mechanically with the x-y-z scanning stages.

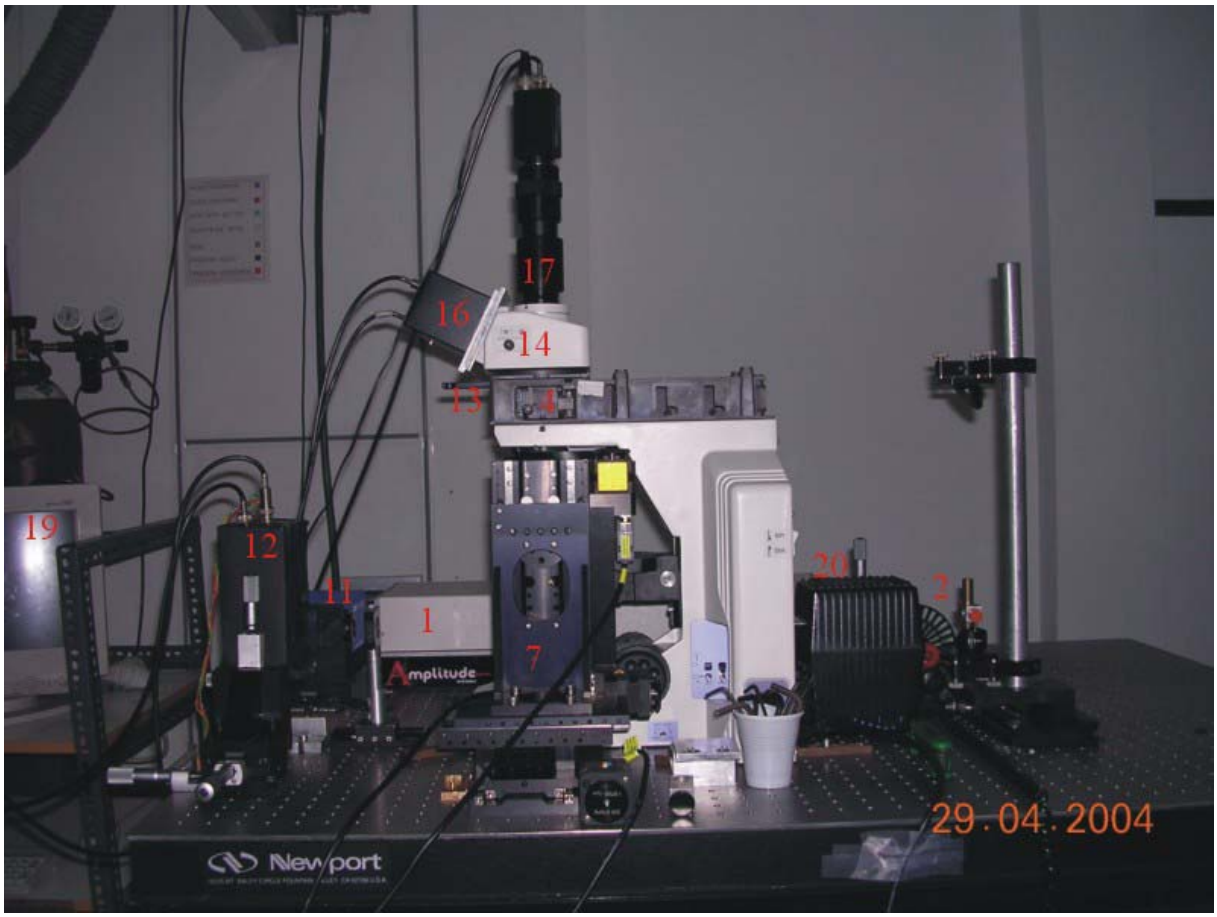

Figure 7.5 Photograph of the experimental setup for combined TPEF – SHG scanning microscopy. The "heart" of the setup is the properly modified Nikon Eclipse ME600D microscope. The setup is placed on an optical table (Newport). The components, depicted in Figure 7.4, that are visible in the above picture have been numerated. The numeration follows that of Figure 7.4.

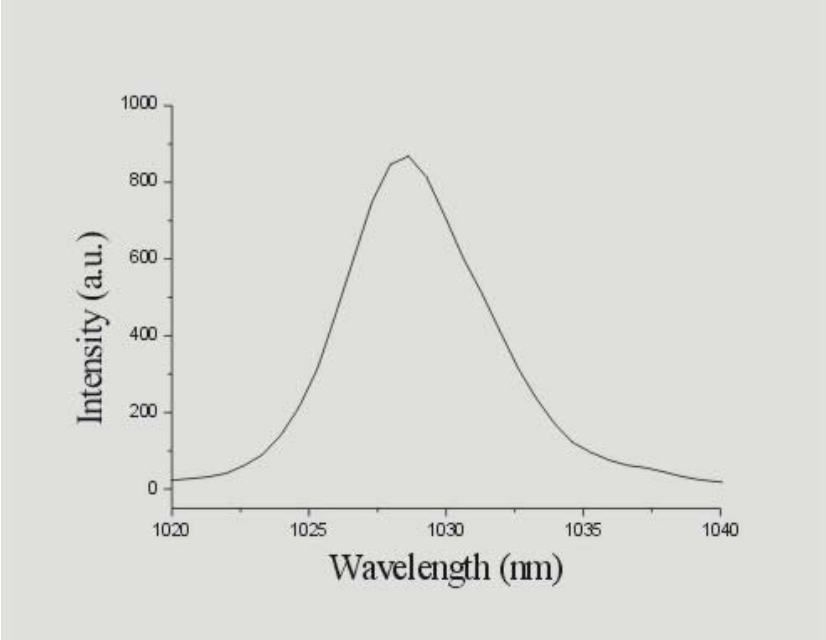

Figure 7.6 Spectral analysis of the laser fundamental beam. The central wavelength λ_o of the fundamental beam is 1028 nm, and FWHM is estimated to be ~6 nm. The value of the central wavelength can shift at about $\pm 2nm$. This shift is due to the misalignment of the optical components inside the laser box, and due to the temperature fluctuations in the lab's room.

7) *x-y-z motorized scanning stage*: The x-y-z motorized scanning stage is a combination of three "one dimensional" Standa 8MT167-100 step motors. Their minimum step is 1 μm, and this already sets a limit in the resolution potential of our system. The combined movement of the three stages is computer controlled by our specially designed software, so that a complicated scanning scheme is created.

8) *Condenser lens*: The condenser of the microscope has a moderate NA ranging from 0.1 to 0.9. We chose that the condenser has the largest possible NA (0.9) in order to be efficient in the collection of the SHG signal. Its working distance is 1.9 mm. It offers a satisfactory optical imaging of the sample, by focusing the light from the standard light source of the microscope. Moreover, it collects and collimates effectively the TPEF and the SHG signal produced by the sample in the forward direction.

9) *Dichroic Mirror*: A dichroic mirror is positioned under the condenser. Its reflectivity is 99% at 45^0 angle of incidence for the 450 - 550 nm spectral range. In this range the greatest part of the TPEF signal, and the complete SHG signal is included. Both of them are reflected and are directed towards the monochromator. By contrast, the fundamental beam propagates through the dichroic mirror and is filtered out from the nonlinear signal.

10) *Focusing lens*: TPEF and SHG signal is focused by means of a lens into the slit of the monochromator. This is important for the proper operation of the monochromator, and prevents loss of the signal. The focal length of the lens is $3\,cm$.

11) *Monochromator*: The monochromator is actually the spectrograph we used in the one-photon fluorescence measurements (Digikrom CM110 CVI), but it has been properly modified. The diode array has been removed. On the output of the spectrograph a $150\,\mu m$ slit has been positioned. The spectrograph offers two optional gratings. The first one is adequate for visible light and has 600 grooves/mm. The second one is adequate for UV light and has 1200 grooves/mm. In our experiments we used the first grating. The signal after its propagation through the grating inside the spectrograph is spectrally analyzed. Its different spectral components diverge, and only the central wavelength passes through the slit. The other components are blocked and prevented from reaching the PMT which is positioned at the back of the spectrograph, where normally the diode array is positioned. The created monochromator was calibrated, tested by means of the mercury lamp, and the estimated value of its spectral resolution is $1\,nm$. The width of the slit on the output of the spectrograph is crucial for the resolution of our monochromator. Putting a $650\,\mu m$ slit, its resolution is estimated to be $\sim 4\,nm$. The monochromator is placed on x-y translation stages (New Focus), with minimum step in each direction $10\,\mu m$.

12) *Photo-Multiplier Tube*: The selected wavelength is incident on the PMT (PMT Hamamatsu R636-10). The specific PMT has a great efficiency in the visible spectral range, and a very low efficiency for wavelengths greater than $800\,nm$. Thus, the remainder from the fundamental beam, even if it reaches via scattering the PMT, can not be detected. The PMT is connected with the Lock-in amplifier, where the created current is converted to a voltage indication. The PMT is placed on a x-y-z translation stage (New Focus) for achieving the optimum alignment.

13) *Filter*: A neutral density filter is placed before the CCD camera and the eye-piece port of the microscope.

14) *Flip-mount mirror*: The standard flip-mount mirror of the microscope routes the image and the TPEF signal from the sample area, either to the CCD camera, or to the eye-piece port.

15) *Short Pass Filter*: A short pass filter (SPF $650\,nm$ CVI) is placed before the PMT at the top of the microscope, in order to cut off the reflected laser light. The TPEF signal is not affected, and reaches without losses the PMT.

16) *Photo-Multiplier Tube*: A PMT (PMT Hamamatsu R4220) is placed at the normal position of the eye-piece of our microscope. The PMT detects the TPEF signal which is

collected by the objective lens in the backward direction. It is also connected with the Lock-in amplifier.

17) *CCD camera*: A CCD camera (Sony XC-57CE) is positioned at the top of the microscope, and is used for the optical observation of the sample through the objective lens.

18) *Lock-in amplifier*: The current signals of the two PMTs are guided into the Lock-in amplifier. The current signals are converted to voltage signals, and via the GPIB communication platform, are transferred to the PC where they are stored. The Lock-in amplifier is a complicated sensitive electronic instrument, appropriate for the detection of low-level signals. It is triggered by the chopper, and "locks" in its frequency. That means that it detects only the signals having this particular frequency. For this reason, the fundamental beam passes through the chopper, and is modulated. The produced TPEF and SHG signals as well as the fundamental beam, carry this frequency, as inheritance from the laser beam's passing through the chopper, and all of these three signals, can be recognized and detected from the Lock-in amplifier. Using this technique, Signal to Noise Ratio (SNR) is dramatically increased, because in most cases, noise is equally distributed in extended spectral ranges ("white noise"). Thus, the detection system increases its sensitivity and enables the detection of extremely low level signals, like the TPEF and SHG signals, produced by biological molecules. We note that the Lock-in amplifier is only one of the solutions for the detection of these signals. Another solution, very popular in similar setups is the use of Boxcar averagers / channel integrators. However, our solution is considerably cheaper, ensuring at the same time the necessary sensitivity.

19) *PC*: The PC is connected with the CCD camera, the monochromator, the Lock-in amplifier and the three step motors.

Using the installed TV-in card, the screen of the PC acts as a monitor for the observation of the sample region, via the CCD camera. Photos of the scanned regions can be taken and stored in the PC for the better interpretation of the scanning data.

Using the commercial Labview software of the spectrograph, we can choose from the panel on the PC monitor the proper grating and the wavelength of the monochromator. Thus, we can decide for the wavelength that is detected from the PMT in the forward direction, getting valuable spectral information.

The Lock-in amplifier provides its output voltage indication, via the GPIB platform, to the PC. This value is directly related with the number of photons, incident on either the PMTs. It is stored and attributed to a specific point in the scanning region. The proper attribution is controlled by our software that is presented in the following paragraph.

Finally, the motion of the three step motors is controlled by the same software. The motors communicate with the PC by means of their manufacturer's card.

20) *Microscope Lamp*: The standard lamp of the microscope (white light, Philips 100 Watt) provides the necessary white light for the optical observation of the sample.

21) *Short Pass Filter*: A short pass filter (SPF 7000 *nm* CVI) is placed before the PMT in the forward direction, in order to cut-off the remainder of the laser light.

2.2 Software of our setup

The developed software is written in Labview 6.1. Its duty is mainly the coordinated motion of the step motors with the data acquisition process from the Lock-in amplifier, and the proper storage of the data. The scanning is performed in the x-y plane for a pre-selected z plane. Hence, the final data file includes three columns, with the first being the x-values, the second the y-values of the scanning points, and the third the voltage indications of the Lock-In Amplifier, which are proportional to the light intensities, incident on the PMTs. The time that the scanning system stays unmoved under the beam ("accumulation time"), before the next step occurs, is a crucial parameter. If accumulation time is too short, it is possible that not enough TPEF and SHG photons are properly collected, and that the indication of the Lock-in amplifier comprises large ambiguity. On the contrary, if the accumulation time is too long, the total duration of the scanning process can be extremely long. A trade-off between these two parameters has to be done. In most of our experiments, the accumulation time during the scannings was set to 30 *ms*, empirically. In *Appendix 1*, the Labview program we developed, is explained in detail.

2.3 Spatial resolution of our nonlinear imaging setup

In **Box 7.1** the resolution (transversal and longitudinal) of our imaging system is calculated.

BOX 7.1: **Spatial resolution of our nonlinear microscope**

In *chapter 3* the mathematical description of a tightly focused beam in the vicinity of the focal center was given. Eq. (3.11) is repeated for convenience:

$$\vec{E}(x,y,z) = -iE_{\omega}\exp\left(-\frac{x^2+y^2}{w_{\rho}^2}-\frac{z^2}{w_z^2}+i\xi k_{\omega}z\right)\hat{\varepsilon} \qquad (7.1)$$

The TPEF and SHG volume were defined identically, based on the above description as:

$$V_{TPEF} = V_{SHG} = \left(\frac{\pi}{2}\right)^{(3/2)} w_\rho^2 w_z \tag{7.2}$$

The transversal and longitudinal resolution were defined as w_ρ and w_z, correspondingly. Figure 2.4 depicts the TPEF (and SHG) volume. For the final determination of the resolution provided by our nonlinear microscope, the minimum step ($1\,\mu m$) of the step motors in the three directions should also be considered. In order to obtain an estimation of the radial beam-waist at the focal spot, the following relation is used [104]:

$$w_\rho \approx \frac{0.52\lambda_o}{n\sin\theta} \tag{7.3}$$

where w_ρ the radial beam-waist, λ_o the wavelength of the fundamental laser beam, n the refractive index of the medium where the beam propagates, and θ the half-angle spanned by the illumination beam in the sample (**Figure 7.7**). Considering that the beam after leaving the objective lens, mainly propagates in the medium surrounding the lens than inside the sample, n can be set equal to the refractive index of the objective lens' surrounding medium. Hence, the denominator in eq. (7.3) is equal to the NA of the objective lens:

$$w_\rho \approx \frac{0.52\lambda_o}{NA} \tag{7.4}$$

Eq. (7.1) is a good approximation of the focused field near the focal center, only when the diameter of the collimated laser beam covers the back aperture of the objective lens. In our case, both the objectives we used have diameter of about 5 mm, while the estimated diameter of the laser beam is about $4.5\,mm$. We regarded this divergence as not critical, and we did not use a system of lens (telescope) for the exact adjustment of the beam's diameter. Using eq. (7.4), we find that the radial beam-waist, when the Nikon (50x, NA 0.8) objective lens is used, is about $670\,nm$. When the Edmund Scientific (100x, NA 1.25) objective lens is used , substitution again in eq. (7.4) provides that the radial beam-waist is about $430\,nm$.

In both cases, the limiting factor for the transverse spatial resolution is clearly the minimum step of the step motors, hence the resolution is estimated to be ~ 1 μm. *As a conclusion, the transverse resolution of our system, is ~ 1 μm, when either the Nikon (50x, NA 0.8) or the Edmund Scientific (100x, NA 1.25) objective is used.*

The longitudinal resolution has been defined as w_z. For a Gaussian ellipsoid illumination profile, as it is described by eq. (7.1), the axial beam-waist w_z is estimated by [104]:

$$w_z \approx \frac{0.76\lambda_o}{n(1-\cos\theta)} \tag{7.5}$$

We attribute again the value of the refractive index that surrounds the objective lens to the parameter n, using the same arguments as above. To proceed further, we consider that the Nikon objective is surrounded by air ($n=1$), while the Edmund Scientific is surrounded by oil ($n=1.45$). Expressing $\cos\theta$ as a function of the NA, eq. (7.5) becomes:

$$w_z \approx \frac{0.76\lambda_o}{n(1-\cos\left(\sin^{-1}\left(\frac{NA}{n}\right)\right)} \tag{7.6}$$

Using eq. (7.6), we find that the axial beam-waist, when the Nikon (50x, NA 0.8) objective lens is used, is about 1960 nm. When the Edmund Scientific (100x, NA 1.25) objective lens is used , substitution again in eq. (7.6) provides that the radial beam-waist is about 1093 nm. In both cases, the limiting factor for the longitidinal resolution is the axial beam-waist, and not the minimum step of the step motors.

Thus, we can safely regard that the longitudinal resolution of our nonlinear microscope is ~2 μm, when the Nikon objective is used, and ~1.1 μm when the Edmund Scientific objective lens is used.

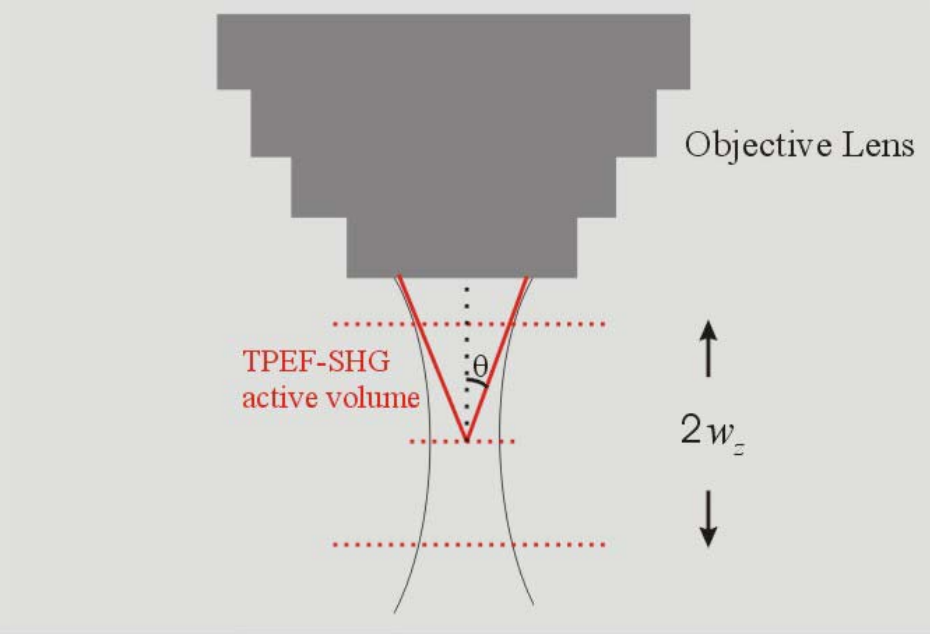

Figure 7.7 Focused Gaussian beam. The definition of θ, the half-angle spanned by the illumination beam in the sample is depicted in the picture.

3. MAPPING OF THE ANTERIOR PART OF *C. ELEGANS*

Our experiments start from the anterior part of *C. elegans*. The main goal of these experiments is to test the proper operation of the nonlinear imaging system. Moreover, we want to investigate the physiology of *C. elegans* in its anterior body-part. The anterior body-part is adequate for the test of our system, because, first, the body structures in this part are very efficient in SHG, and second, the strains we use for these experiments are the same we used for the one-photon fluorescence measurements. They express GFP in considerably high concentrations inside their pharynx. If we could not detect a significant TPEF signal from this strain, that would mean that our setup has an extremely low sensitivity. Fortunately, as it will be shown below, the TPEF signal from the GFP molecules, expressed in the pharynx of the nematode, can be detected very easily, proving the detection potential of our system.

3.1 Sample preparation

The samples were supplied to us by the *Institute of Molecular Biology and Biotechnology of FO.R.T.H.*, and specifically by the lab, leaded by Dr. Nektarios Tavernarakis. Standard procedures for *C. elegans* strain maintenance, crosses and other genetic manipulations were followed [105]. Nematode rearing temperature was kept at 20^{o}C. The strain we used for this

line of experiments is called: IS[*pmyo-2::pes-10::GFP*]. This strain, as well as all the others that will be used in the following experiments, arises with genetic manipulation from the wild type worm, strain N2, variety Bristol. The integrated strain *pmyo-2::pes-10::GFP* expresses the GFP molecules fused with the PES-10 protein under the control of the myo-2 promoter. The GFP molecules are expressed fused inside the pharynx of the nematode. They are expressed in large concentrations, hence their one-photon fluorescence can be easily observed, even with a simple CCD camera (Figure 7.2). Their TPEF is expected to be also easily detected by our system (Figure 7.4). The fused GFP molecules are not bound to any cellular membrane, thus, they can freely rotate and lack any global orientation. Hence, they are not efficient for SHG.

Before each experiment, young adult animals are anaesthetized by immersing to 20mM of sodium azide (NaN_3), and subsequently they are mounted between the glass slides of the sample holder. Sodium azide targets the mitochondria in all the cells of the nematode, and blocks the production of ATP. The nematode is immobilized a few minutes after the immersion, and dies a few hours later. The expression of GFP molecules gradually stops, and 2-3 hours after the immersion, no TPEF signal can be detected from the nematode.

3.2 TPEF image of the anterior part of C.elegans

The sample was placed on the sample holder and was focused. The Nikon (50x, NA 0.8) objective lens was used. The fundamental laser beam passes through the optics of the microscope and is focused onto the sample. The power of the incident beam that reaches the sample is measured to be $10\,mW$. The sample is observed by means of the CCD camera and is brought to a position, where the beam is focused inside the region of the pharynx. We switch-off the lamp of the microscope, we switch the flip-mount mirror of the microscope, so that the signal is directed to the upper PMT, and we verify that a strong signal is detected from the PMT. This is a strong indication that the specific z-plane is adequate for a complete x-y scanning of an extended region. The flip-mount mirror is switched again, and by means of the CCD camera a region with the adequate dimensions is chosen to be scanned. In **Figure 7.8**, a typical TPEF image of the anterior part of the *C.elegans* nematode is depicted. The image has been matched with the photo of the nematode, so that it overlaps exactly with the real scanned region. In Figure 7.8, the lighter colors represent regions that give high signal levels. The outline of the pharynx is obvious, and ensures us that the signal originates from

the pharynx, where the GFP molecules are expressed. The central question, however, is how can be sure that the detected signal is really TPEF.

The question to this answer arises by making simple considerations. The main disadvantage of the detection in the backward direction is indeed the inability to perform a spectral analysis of the signal. However, some spectral regions are excluded due to the spectral response of the PMT, and the filter placed before the PMT.

The reflected laser beam is partially blocked from the short-pass filter (SPF 650 *nm* CVI) before the PMT. The remainder of the reflected laser beam is incident on the PMT, but due to the PMT's poor sensitivity for wavelengths greater than 900 *nm* its detection is poor. Moreover, the reflected laser beam can not be correlated with specific points of the scanned region, but it rather constitutes a steady background for the measurement. Thus, the resultant scheme of the image can not be attributed to the reflected laser beam.

Similarly, the detected signal can not be attributed to one-photon fluorescence, because there are not organic molecules that are known to absorb in the Near Infrared (1020-1040 *nm*).

A third possibility is that the detected signal in the backward direction is SHG signal. This is opposed at first glance to the forward propagation analysis of SHG we carried in *chapter 3*. However, we have noted that SHG can initially propagate in the forward direction, and be partially re-routed backwards, due to reflection at an interface. In our case the SHG signal could originate from the structural proteins that are known to be efficient in SHG and surround the pharynx. The reflection could occur inside the nematode, at the interface between the sample area and the lower glass slide, or at the interface between the lower glass slide and the air. In the following paragraphs it will be referred that such a reflectance happens indeed, and SHG signal can be detected in our setup in the backward direction. However, the detected signal is 20-50 times, lower than the SHG signal that is detected in the forward direction. In the case of the image we get in Figure 7.8, the levels of the signal are too high to be attributed to a reflected SHG signal. Moreover, the spatial distribution of the signal indicates that the signal mainly originates from the inner part of the pharynx, where the GFP molecules are expressed, and not from the surroundings of the pharynx, where the structural proteins are located. Hence, the magnitude and the spatial distribution of the signal leads us to the conclusion that it is about TPEF.

At this point, it is useful to mention that the inability for spectral analysis of the signal in the backward direction is a characteristic of most of the nonlinear imaging systems. In all these systems, the signal in the backward direction is detected and directly attributed to TPEF without further discussion. Spectral information with no details can only be provided with the

use of filters before the input of the PMT. The disadvantage of our setup lies in the fact that due to the specific wavelength of the laser beam, and the specific absorption and emission spectrum of GFP (S65C), SHG and GFP TPEF are spectrally close together and can not be distinguished very easily only with the use of filters.

Being sure that the detected signal is TPEF, we attribute it to the GFP molecules, since we do not know any other fluorescent molecules being located specifically inside the pharynx of the nematode.

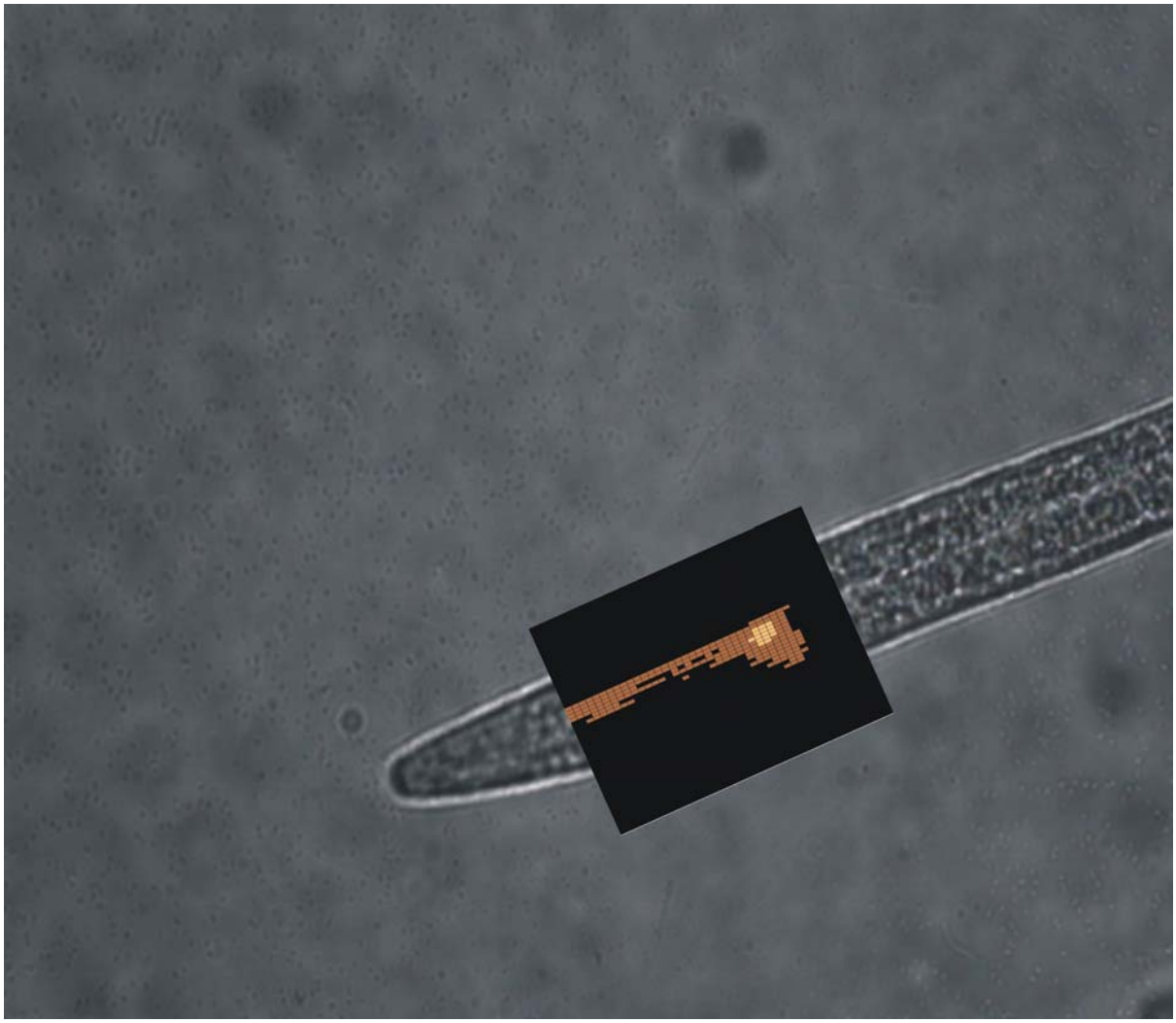

Figure 7.8 TPEF image of the anterior body part of the nematode IS[*pmyo-2::Pes-10::GFP*]. This integrated strain expresses fused GFP molecules (S65C) inside the pharynx of the nematode. The TPEF originates from the GFP molecules, and the resultant image outlines strongly the pharynx of the worm. The scanned region has 60 x 80 μm^2 dimensions. The TPEF signal was detected in the backward direction.

The scanned region is an orthogonal parallelogram with dimensions 60 x 80 μm^2. The minimum step in the x-direction (quasi vertical) is 1 μm, while the step in the y-direction

(quasi horizontal) is $2\,\mu m$. The scanned parallelogram seems to be rotated, with the vertical and the horizontal axes being taken as reference. This rotation appears in all our experiments, because of a corresponding misalignment between the sample holder and the microscope. However, this rotation is steady (17^o) and does not cause any ambiguity in the resultant images.

3.3 Combined SHG - TPEF images of the anterior part of C.elegans

The set of experiments that are presented in this paragraph were made by taking advantage of the whole setup, shown in Figure 7.4. The signal detection in the forward direction was possible, and the spectral analysis of this signal could provide us useful information.

The optimization of the forward detection system was achieved by means of a BBO crystal. The crystal was placed at the sample holder, the fundamental beam was focused onto it, and the produced SHG signal was directed into the monochromator, and finally onto the PMT. The positions of the dichroic mirror after the condenser lens, the lens before the monochromator, the monochromator itself, and the PMT were optimized, so that the indication of the Lock-in amplifier was maximum. The alignment was optimized for the collection of the SHG signal, however, the same alignment is also adequate for the collection of the TPEF signal.

For the experiments presented in this paragraph, the Nikon (50x, NA 0.8) objective lens was used. The use of this objective lens is obligatory in all the experiments we aim to detect SHG signal. In *chapter 3*, it was already mentioned that the condenser must have larger NA than the objective lens, in order to collect practically all the SHG signal. Given that the condenser of our microscope has NA equal to 0.9, the use of the Edmund Scientific (100x, NA 1.25) objective lens is unacceptable. Measurements showed us that almost 90% of the SHG signal is lost, when the Edmund Scientific lens is used for the tighter focusing of the fundamental laser beam. Thus, the Nikon objective was our only reasonable choice for SHG imaging.

For this set of experiments, the following strains were used: the known strain IS[*pmyo-2::pes-10::GFP*] expressing fused GFP molecules inside the pharynx, and wild type worms, strain N2, variety Bristol, as experimental control. Wild type worms are not genetically manipulated, thus they do not express GFP in any part of their body.

We started the experiments investigating the wild type worms. Knowing that in their anterior body part there are not any fluorescent molecules that could produce a significant TPEF signal, we focused our research on the endogenous SHG imaging of these worms. The

monochromator was regulated to allow the transmittance of the SHG peak ($514\,nm$), while blocking all the other wavelengths. In **Figure 7.9**, **Figure 7.10** and **Figure 7.11**, endogenous SHG images of a wild type worm are shown. The worm has been scanned successively in three different optical sections. The distance between the successive sections is $10\,\mu m$. The dimensions of the scanned region are 60 x $120\,\mu m^2$, with the minimum step being $2\,\mu m$ in each direction.

In all three cases the endogenous SHG imaging of the anterior part of the C. elegans nematode was possible, due to the high signal levels from the muscles around the pharynx and the muscles of the body walls at the edges of the nematode. The structural protein that gives rise to the SHG signal is mainly actomyosin. In *chapter 3*, we described the form of the actomyosin assemblies, and we mentioned that they are the main components of the sarcomere, i.e. of the skeletal muscle. Their SHG efficiency is proved by our images, since SHG signal is highly produced from parts of the nematode where relatively thick muscles are located. The images, shown in Figure 7.9, 7.10 and 7.11, are considered to be state of the art, as far as endogenous SHG imaging is concerned. In **Figure 7.12**, two images of the same anterior body part of the *C. elegans* nematode are depicted. The pictures have been taken from a lately published paper [106]: *Nature Biotechnology*, vol.21, November 2003. In these images the highest signal levels arise from the structures we have already mentioned, i.e. the body wall muscles at the edges of the animal (Figure 7.12a), as well as the muscles which constitute the chewing mechanism and surround the pharynx (Figure 7.12b). Combined TPEF and SHG imaging has been used in order to specify the dominant source of SHG. The actomyosin complexes in nematode muscle consist of two major isoforms of myosin: myosin heavy chain A and myosin heavy chain B (MCH A and MHC B, respectively). The published data [106] were consistent with the myosin heavy chain B isoform being the dominant source of SHG, with little contribution from either myosin heavy chain A or actin filaments. Our setup has not the spatial resolution for such an investigation, and moreover, the aim of our project is not the identification of the dominant SHG source within the muscle sarcomeres. However, the similarity between the published images in Figure 7.12, and our images in Figure 7.9, 7.10 and 7.11, ensures the reliability and the potential of our inexpensive setup. The sectioning ability of our setup is verified, since its behavior is similar to the published data, i.e. at one optical section the muscles around the pharynx are clearly seen, and the body wall muscles are not (Figure 7.9), and at another optical section the opposite occurs (Figure 7.11).

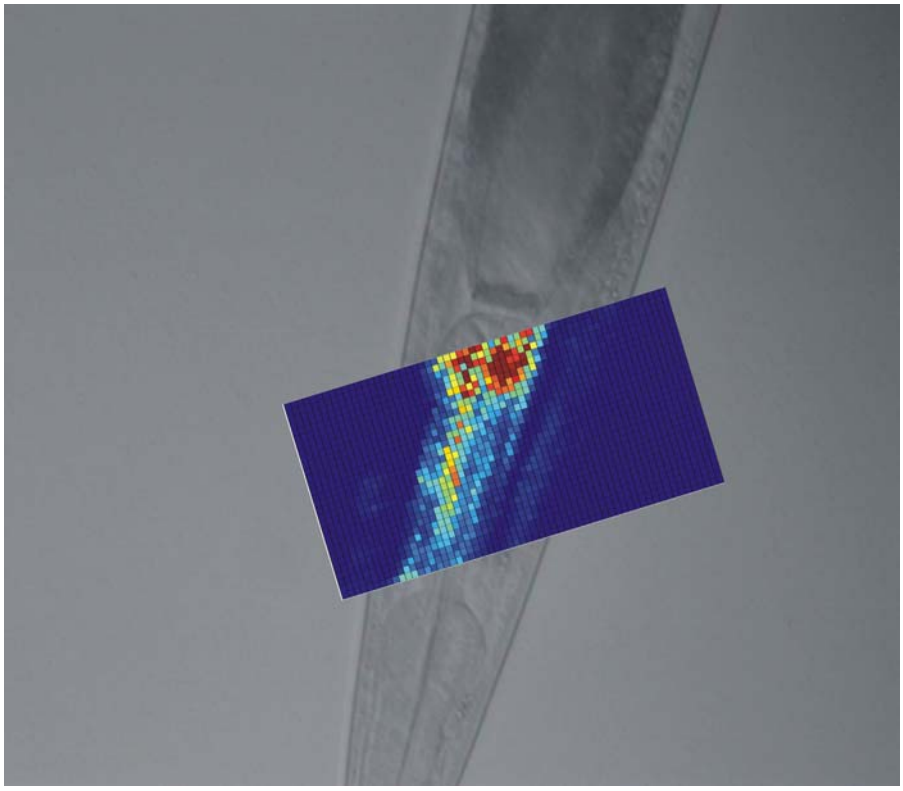

Figure 7.9 Endogenous SHG imaging of a living adult C. elegans nematode. The sarcomeres are seen in a large portion of the chewing mechanism. The scanned region has dimensions 60 x 120 μm^2.

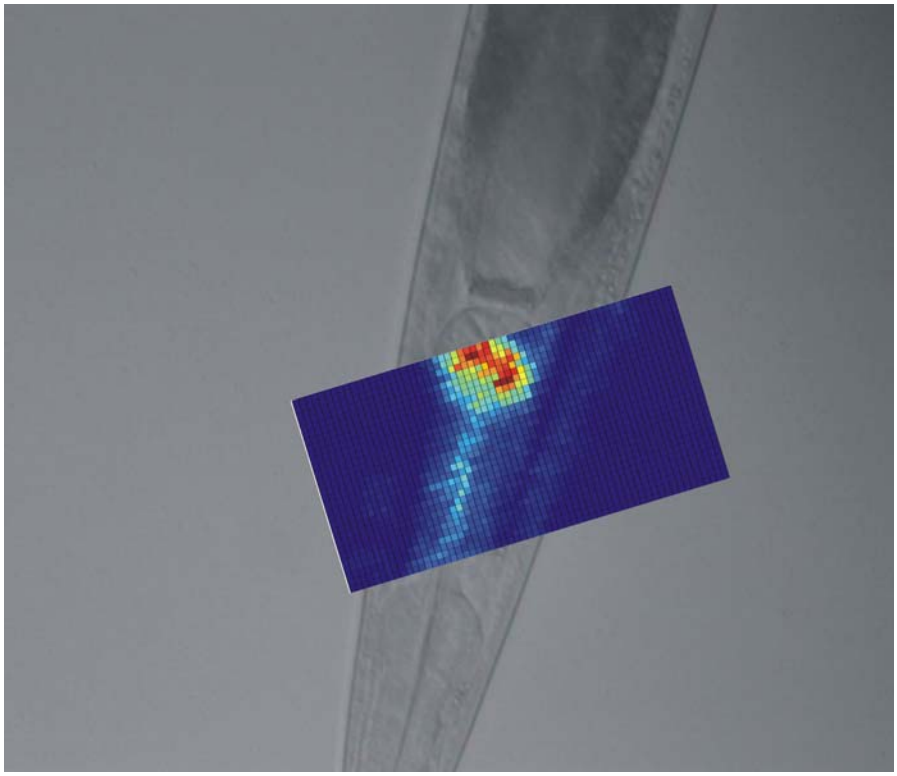

Figure 7.10 An optical section 10 μm further into the same animal. The sarcomeres are seen in a smaller portion of the chewing mechanism, but are discernible in the body wall muscles at the edges of the animal.

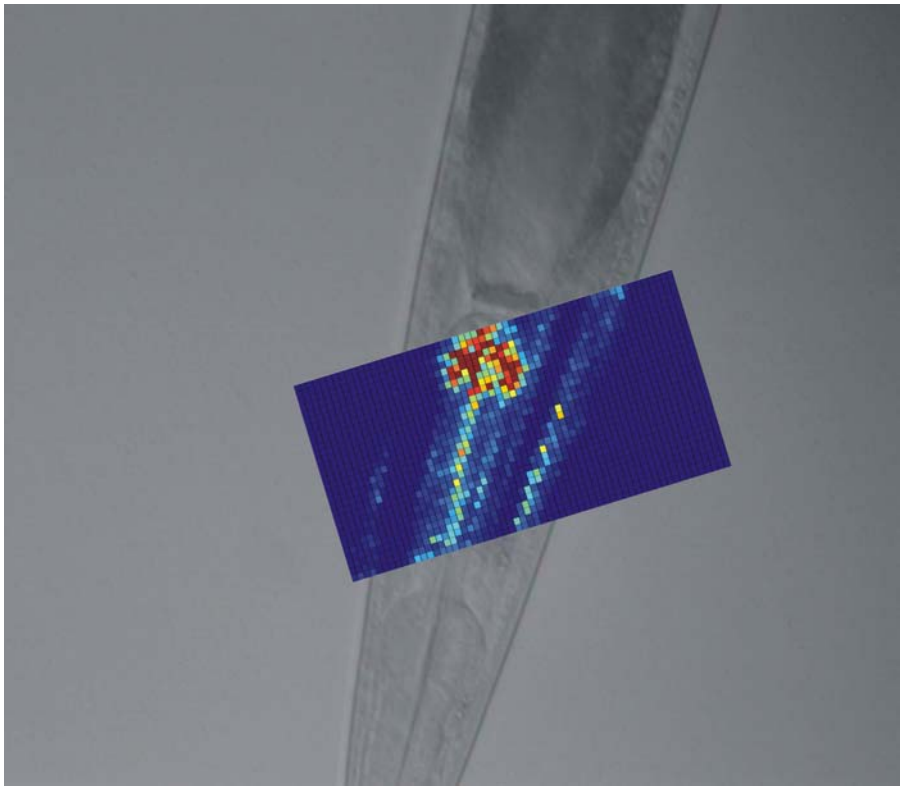

Figure 7.11 A third optical section of the same animal another 10 μm further into the same animal, 20 μm from the initial z position. The sarcomeres of the body wall muscles at the edges of the animal are clearly seen now. The same stands for the muscles of the chewing mechanism around the pharynx of the animal. The dimensions of the scanned regions are the same in all the three images.

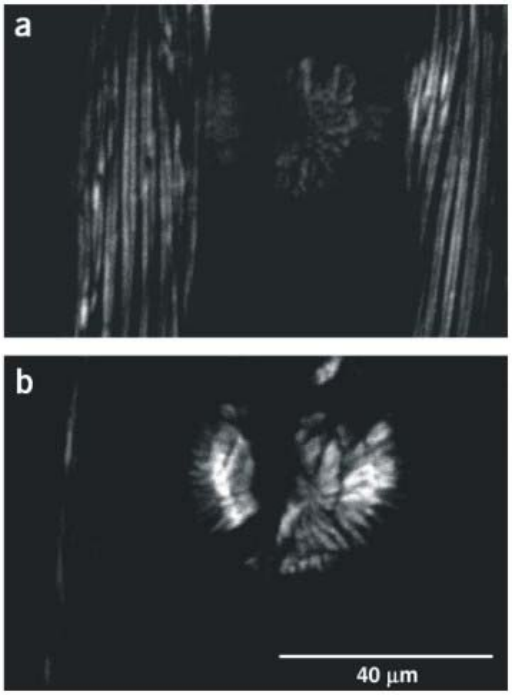

Figure 7.12 Endogenous SHG imaging of a living adult C. elegans nematode, showing two distinct optical sections. Pictures taken from [106]: *Nature Biotechnology*, vol.21, November 2003.

In order to assure that the resultant images are SHG images indeed, we performed a spectral analysis of the signal. We focused the laser beam onto the muscles around the pharynx, and we found a position that produced a strong signal. Regulating the monochromator, we analyzed spectrally the detected signal. The resultant spectrum is depicted in **Figure 7.13**.

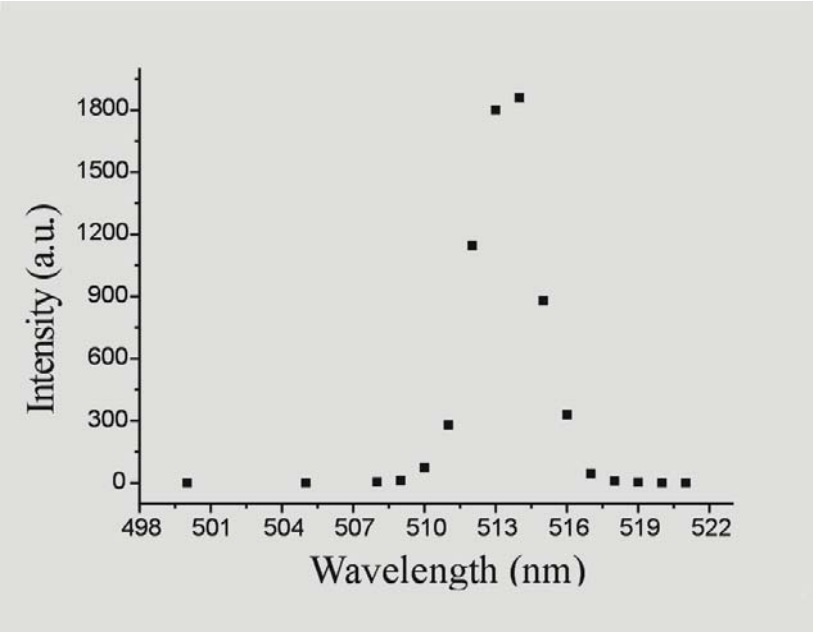

Figure 7.13 Spectral analysis of the signal originating from the muscles around the pharynx of wild type worms. The spectral distribution indicates that it is SHG signal. The peak wavelength is 514 nm, and FWHM is about 4 nm.

This spectrum clearly indicates that the detected signal is SHG signal indeed. The peak wavelength is 514 nm, which is exactly half the peak wavelength of the fundamental laser beam (1028 nm). The spectral width, characterized by the FWHM is about 4 nm, which is lower by a factor of $1/\sqrt{2}$ from the measured FWHM of the fundamental laser beam (~6 nm). That is consistent with the theoretical analysis described in Box 3.5, in *chapter 3*. Thus, there can be no doubt that the images, presented previously, are obtained by endogenous SHG signal.

In the following experiments, presented in this paragraph, the strain IS[*pmyo-2::pes-10::GFP*] was used. It has already been mentioned, that the GFP molecules are expressed in great concentrations inside the pharynx, so that their total TPEF signal is very strong. This signal can be detected in the backward direction (Figure 7.8), but can be also detected in the forward direction, although the monochromator is interjected. In order to be sure that the detected signal is TPEF indeed, and not SHG, we regulate the monochromator to have central wavelength 525 nm. As we can see in Figure 7.13, the SHG spectral distribution does not

extend further than $520\,nm$. Thus, the detected signal at $525\,nm$ can be attributed only to TPEF.

The monochromator has $1\,nm$ spectral resolution. If we assume that the TPEF is spectrally extended in about $100\,nm$ with a relatively smooth dependence on the emission wavelength, we conclude that the detected TPEF power in the forward direction is about 2 orders of magnitude lower than the detected TPEF power in the backward direction. That stands because in the backward direction, the total TPEF power extended in its total spectrum, is detected, whereas in the forward direction only a thin spectral slice around $525\,nm$ is finally detected. If we further consider that the collection efficiency and the alignment is better in the backward direction, the reduction of the signal level by a factor of 100 seems to be reasonable.

However, the imaging of the anterior body part of the specific strain was feasible with our setup, as it is depicted in **Figure 7.14** and **Figure 7.16**. The same region with dimensions 34 x $66\,\mu m^2$ was scanned in two optical sections, $10\,\mu m$ away from each other. The initial optical section was chosen by maximizing the TPEF signal.

The same scannings, in the same two optical sections were performed with the monochromator regulated at $514\,nm$. The resultant SHG images are depicted in **Figure 7.15** and **Figure 7.17**. We note that Figure 7.14 and Figure 7.15 correspond to exactly the same scanned region (in the z-direction, as well). The same stands for Figure 7.16 and Figure 7.17.

Comparing the two above pair of images, we come to the same conclusions. The TPEF signal is strong from the inner part of the pharynx, where the GFP molecules are expressed in great quantities. The corresponding SHG signal from the inner part of the pharynx is extremely weak, because the random oriented GFP molecules do not possess SHG efficiency. On the contrary, the SHG signal from the muscles that surround the pharynx is strong. In this way, in the SHG imaging, the pharynx of the nematode is outlined. Moreover, the whole body of the nematode is outlined, due to the body wall muscles, at the edges of the nematode.

Collagen very likely participates in the outline of the nematode, since it is one of the basic ingredients of the hypodermis, and has great SHG efficiency. Although we did not investigate any further the possible participation of the collagen in the resultant SHG signal from the edges of *C. elegans*, its efficiency in SHG, as it was described in *chapter 3*, assures this participation . Unfortunately, the transversal resolution of our setup was not enough for the discrimination between the SHG signal arising from the collagen and the SHG signal arising from the body wall muscles.

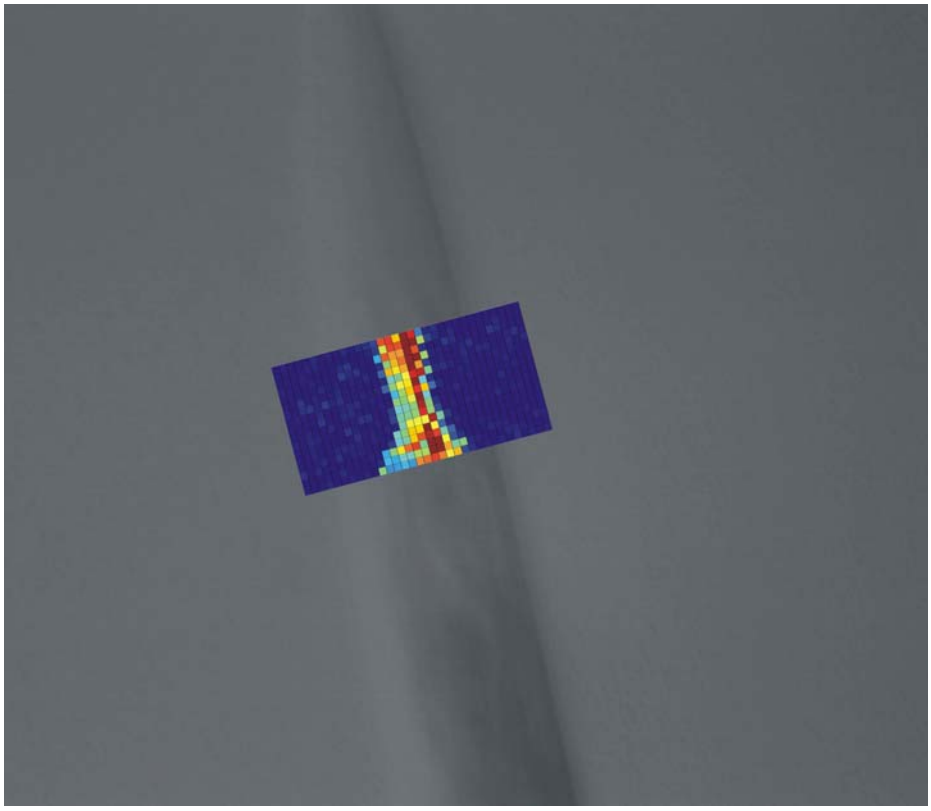

Figure 7.14 TPEF imaging of the strain IS[*pmyo-2::Pes-10::GFP*]. Detection in the forward direction with the monochromator set at 525 nm. The scanned region has dimensions 34 x 66 μm^2. The inner part of the pharynx, where the GFP molecules are expressed, is clearly shown.

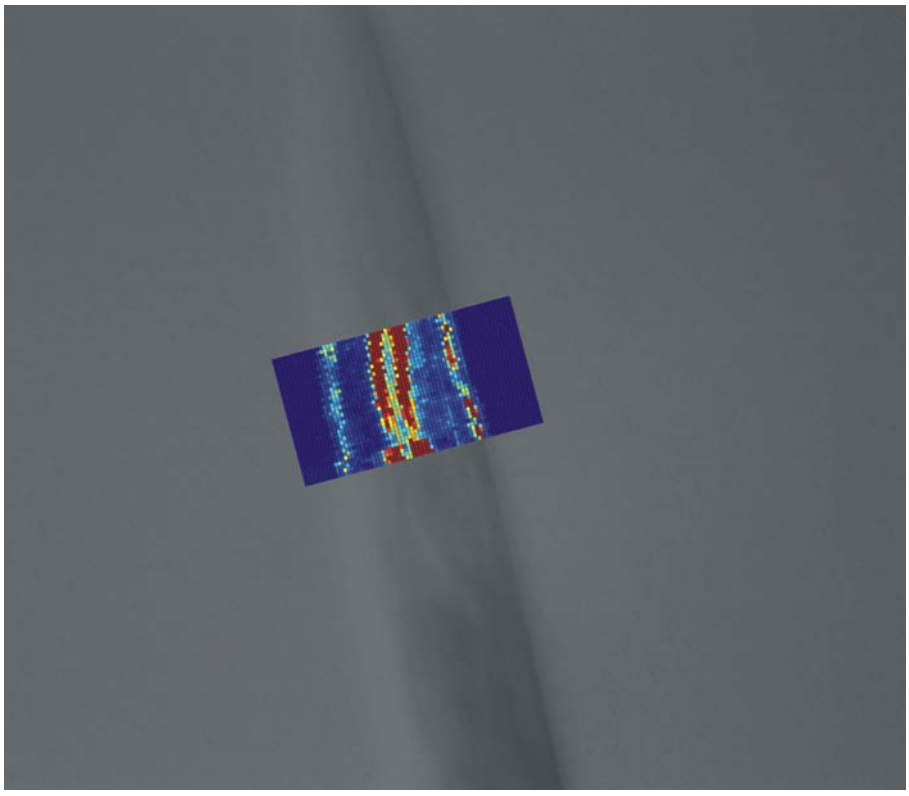

Figure 7.15 Corresponding SHG imaging of the same region, at the same optical section. The monochromator was set at 514 nm. The pharynx and the edges of the nematode are outlined.

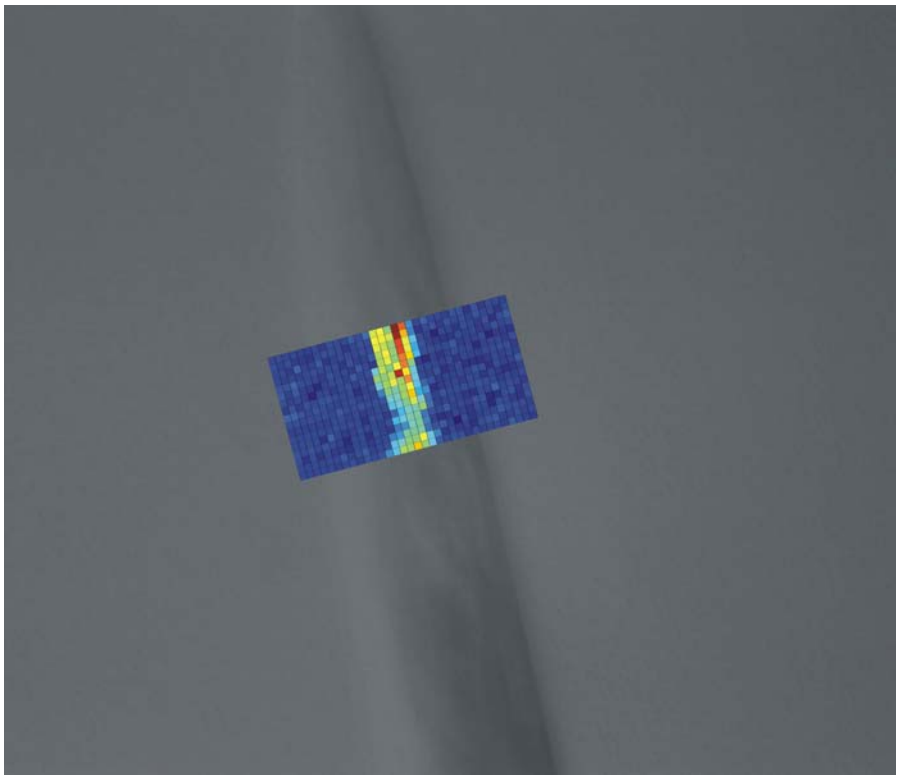

Figure 7.16 TPEF imaging of the strain IS[*pmyo-2::Pes-10::GFP*]. Detection in the forward direction with the monochromator set at 525 nm. The scanned region is the same with that in Figure 7.14 and 7.15, but the optical section is 10 μm further in the nematode. The inner part of the pharynx, is clearly shown, again.

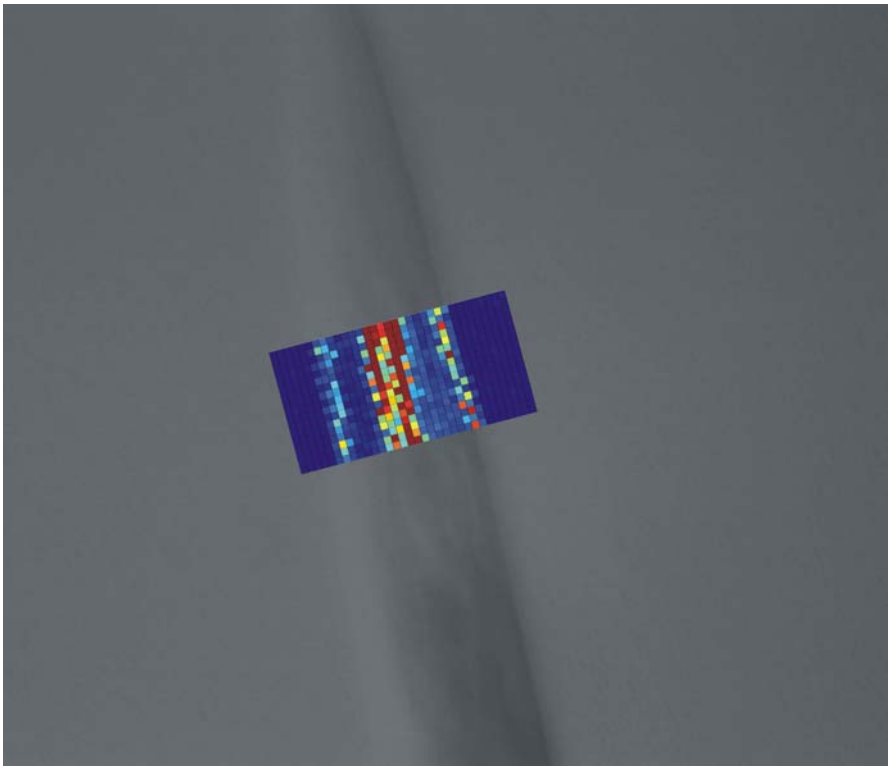

Figure 7.17 Corresponding SHG imaging of the same region, at the same optical section, as in Figure 7.16. The monochromator was set at 514 nm. The pharynx and the edges of the nematode are outlined, again.

In order to investigate the TPEF participation in the detected signal at 514 *nm* , we performed a spectral analysis of the forward detected signal. We focused the laser beam onto a point at the edge of the pharynx. Due to the limited spatial resolution of our setup, both the TPEF of the GFP at the inner part, and the SHG from the muscles, at the outer part of the pharynx, contributed to the detected signal. The spectrum of the forward detected signal is depicted in **Figure 7.18**. The spectral distribution has the characteristics of SHG signal with the FWHM being again ~ 4 *nm* .

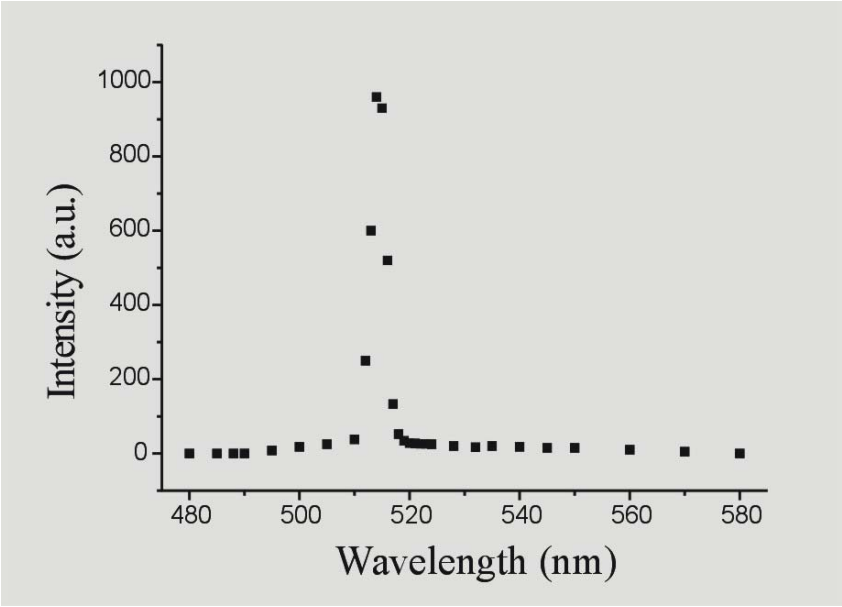

Figure 7.18 Spectral analysis of the forward detected signal. The beam was focused on the edge of the pharynx of the strain IS[*pmyo-2::Pes-10::GFP*]. The signal comprises both TPEF from the GFP molecules at the inner part of the pharynx, and SHG produced from the sarcomeres at the outer part of the pharynx.

However, if we zoom-in the diagram, the presence of TPEF is obvious. In **Figure 7.19**, a zoom-in of the resultant spectrum is depicted. Whereas the reduction of the signal is relatively abrupt at the shorter wavelengths, the reduction is smoother at the longer wavelengths. The characteristic curve of the fluorescence is present, and the signal vanishes at wavelengths longer than 580 *nm* . These characteristics were absent in the spectrum of the signal, originating from wild type worms (Figure 7.13).

Looking carefully the two diagrams we come to the following conclusions: First, the detected signal comprise both SHG and TPEF, indeed. Second, at 514 *nm* , the signal also comprises both SHG and TPEF, but SHG signal is at least 30-50 times larger than the "spectral slice" of the TPEF at this wavelength. *Thus, the contribution of the latter can be considered insignificant, and in any case does not affect essentially the SHG scanning image*. Third, the TPEF from the GFP, when it is excited by our laser, is extended till 580-590 *nm* . However, its

detection in wavelengths longer than $540\,nm$ becomes even more difficult. A proper choice is the $525\,nm$, a wavelength where the fluorescence emission is high, and simultaneously the SHG signal has been essentially nullified.

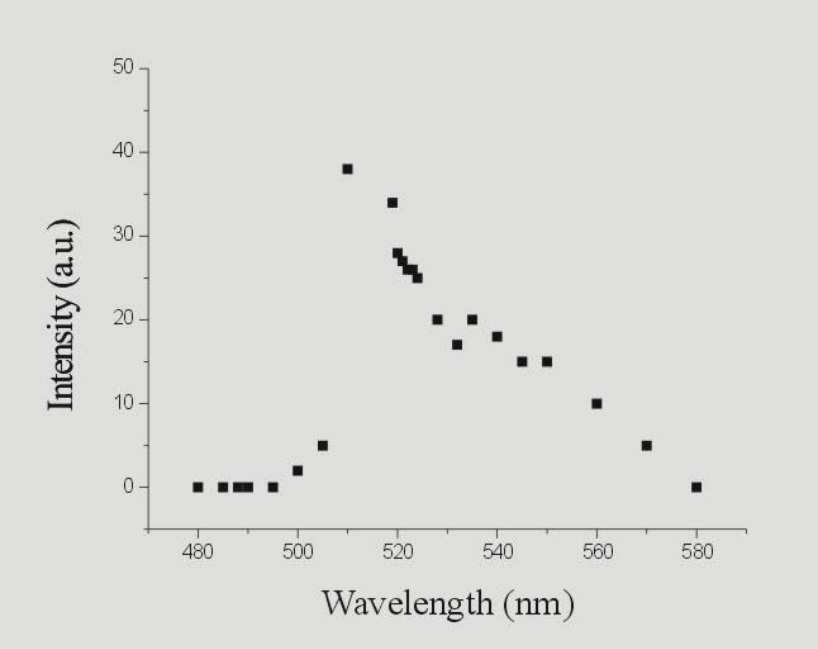

Figure 7.19 Zoom-in of the spectrum, depicted in Figure 7.18. The signal curve is abruptly reduced at the shorter wavelengths, but is smoother at the longer wavelengths, due to the fluorescence emission of the GFP molecules. Comparing the two diagrams, we conclude that the contribution of TPEF at 514 nm is insignificant, relative to the SHG.

4. MAPPING OF THE POSTERIOR PART OF *C. ELEGANS*

Our experiments continued with the investigation and the nonlinear mapping of the posterior part of *C. elegans*. In *chapter 6* we mentioned that in this body part of the nematode, two of the six touch receptor neurons are located, namely PLML and PLMR. The first goal of our investigations was the localization of these neurons by means of TPEF imaging. GFP molecules can be expressed at these neurons, either in the cytoplasm, or bound to transmembrane proteins. In the first case, the concentration of the expressed GFP molecules is quite large, but in any case smaller than the concentration of GFP molecules in the pharynx of the strain IS[pmyo-2::PES-10::GFP], we used in the previous experiments. In the second case, the concentration of the expressed GFP molecules is really small, the TPEF signal of these molecules is poor, and its detection is a difficult task.

According to the up to now dominant aspect, there are not structures in the posterior part of *C. elegans*, that are significantly efficient in SHG. The body wall muscles in the posterior part are considered to be much thinner and weaker than the body wall muscles in the anterior part, which proved to give a sufficiently high SHG signal. Inside the worm there is not a structure similar to the chewing mechanism we examined in the anterior part, hence, we expected that the SHG signal would be extremely low at the posterior part. That was also the reason, we chose the specific two touch receptor neurons to investigate. The idea was that the desired exogenous SHG signal from the globally oriented GFP molecules, could be easily distinguished from the low level endogenous SHG signal.

We started our investigations in the posterior part, using strains that express GFP fused in the cytoplasm of PLM neurons. The GFP molecules can not produce SHG signal, due to their random orientation inside the cytoplasm. The successful localization of the neurons, by TPEF microscopy, would be another proof of the reliability of our setup.

4.1 Investigation of strains with fused GFP molecules in touch receptor neurons

The names of the strain, used in this line of experiments, is: N2, IS[pmec-4 GFP]. It is a strain, where the [pmec-4::GFP;lin-15(+)] array is integrated in the 4^{th} and the 1^{st} chromosome respectively. It was obtained from the *Caenorhabditis elegans Genetic Center* (CGC). With simple words, in this strain, the mec-4 promoter drives the expression of the fused GFP in the six touch receptor neurons (cell specific promoter). This promoter normally expresses the mec-4 gene in these cells, but by performing molecular engineering techniques

it now expresses the GFP molecule. The molecules, due to the lack of any signal that would transfer them in the membrane, are finally expressed in the cytoplasm of the six touch receptor neurons in large quantities and yield fluorescence, when properly excited. Their orientation is random, thus their SHG efficiency is nullified. In **Figure 7.20** a confocal image of the fluorescent strain N2, IS[pmec-4 GFP] is shown. The image was provided by Dr. N. Tavernarakis and G. Vogglis.

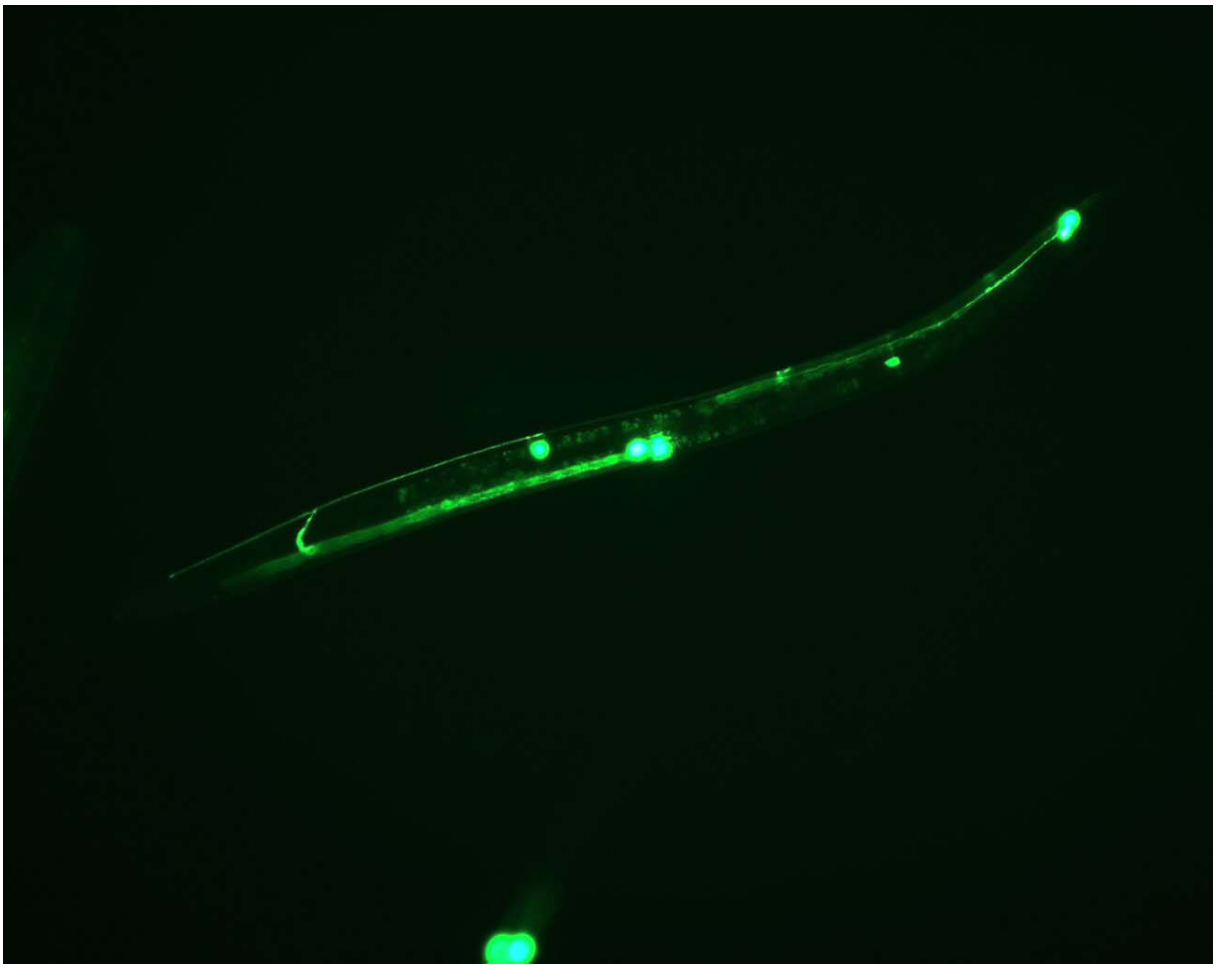

Figure 7.20 Confocal image of the N2, IS[pmec-4 GFP] strain. GFP molecules have been expressed in the cytoplasm of the six touch receptor neurons. The two luminous spots on the upper right corner represent fluorescence, yielded from the two PLM neurons in the posterior part of the worm.

In Figure 7.20, six luminous spots can be distinguished on the worm, representing the fluorescence yielded from the GFP molecules. The GFP molecules are expressed in the six touch receptor neurons. The luminous spots at the upper right corner of the image originate from the soma of the two PLM neurons in the posterior body part of the worm. The large intensity of the fluorescence is an indication that the expression of the GFP molecules is very efficient. However, we note that the conditions of the confocal microscope are ideal, as far as both one-photon fluorescence excitation (Argon Ion laser - $488\,nm$) and detection are

concerned. Aim of our experiment was the localization of these PLM neurons by means of TPEF, excited by our laser. The soma of these neurons is about 2-3 μm width , while the axon is less than 1 μm width, below our resolution limit. For these experiments, the setup depicted in Figure 7.4 was used. We used the Nikon (50x, NA 0.8) objective lens. In **Figure 7.21**, the TPEF imaging of the posterior part of the strain N2, IS[pmec-4 GFP] is depicted.

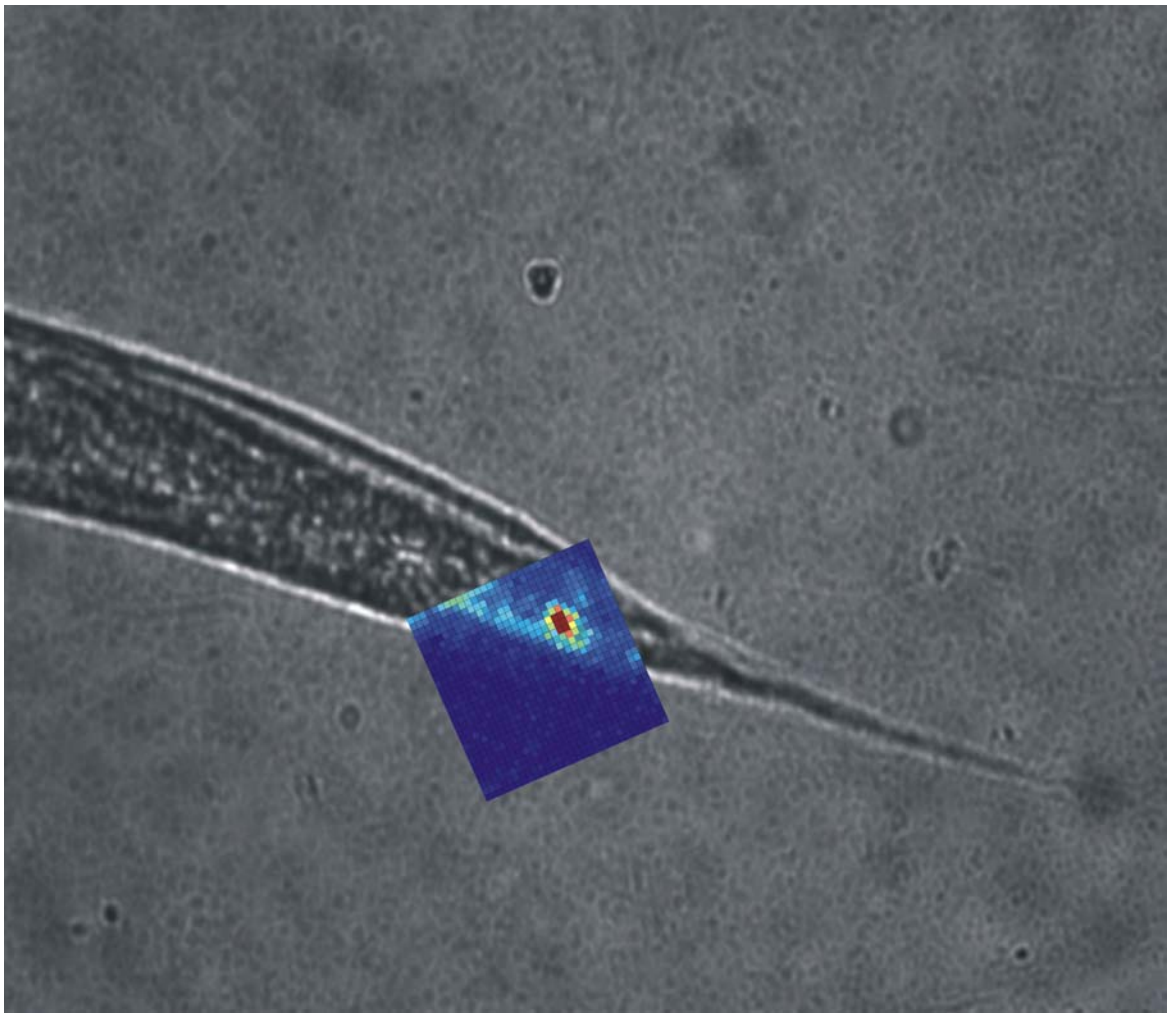

Figure 7.21 TPEF imaging of the posterior body part of the N2, IS[pmec-4 GFP] strain. The soma and the axon of a PLM neuron can be distinguished. The TPEF signal was detected in the backward direction. The scanned region has dimensions 30 x 30 μm^2.

The TPEF signal was detected in the backward direction, thus spectral information was not available. Firstly, we approached the points of maximum signal, we optimized the focusing by moving the z-step motor, and afterwards we performed a scanning of an extended region (30 x 30 μm^2). The soma of the neuron appears in our image as an orthogonal parallelogram with dimensions 2 x 3 μm^2, which is close to reality. Moreover, the axon of the neuron can be distinguished, as it fades away. Although its real width is in the submicron scale, it seems to have a width of about 2 μm, which is the transverse resolution of our setup.

The position of the neuron, as it is pointed in the image, is consistent with our knowledge and experience about the possible position of the PLM neurons. The reader may wonder, why only one PLM neuron is shown in the image, although the other one is expected to be located in the same region. The answer is found in the intrinsic optical sectioning of TPEF imaging. The second PLM neuron is located at another optical section of the scanned region, further than the longitudinal resolution of our setup.

In the next experiment, presented in this paragraph, we took advantage of the strong TPEF signal emerging from the PLM neurons of the specific strain. Due to its strength, the TPEF signal was detectable in the forward direction at $525\,nm$. The detection was not so trivial as in the case of the TPEF, emerging from the pharynx of the IS[pmyo-2::PES-10::GFP] strain, but in any case was feasible. We performed the same scanning at the same optical section, detecting the first time the TPEF signal in the posterior part of C. elegans, and the second time the SHG signal at $525\,nm$. In **Figure 7.22** the TPEF image is depicted, and in **Figure 7.23** the corresponding SHG image is presented. The optical section was chosen in a way that the TPEF signal was maximized.

The TPEF image at $525\,nm$ looks like as it was expected. The neuron is depicted unambiguously, with its soma and a part of its axon to be clearly describable. No SHG signal can be detected at this wavelength, hence the edges of the worm are not apparent.

The SHG image also looks like, more or less, as it was expected. The outline of the worm appears, due to the body wall muscles at the edges of the worm. The participation of the collagen fibers is very possible. Between the edges of the nematode, the SHG signal remains low, indicating that there are not any thick muscle structures in the posterior part, similar to the chewing mechanism in the anterior part. The PLM neurons are not depicted, since they do not possess SHG efficiency, due to the random orientation of the GFP molecules. However, the TPEF at $514\,nm$ does exist. Two are the possible reasons that this signal is ambiguous in the SHG image at $514\,nm$. First, the SHG signal level from the body wall muscles is much higher than the TPEF signal level of the GFP molecules, and second, there is a spatial overlap between the muscles at the left edge of the nematode, and the PLM neuron. This overlap occurs due to the limited transverse resolution of our setup.

Looking carefully the two pictures, we should differentiate quite a lot the aspect we had for the difficulty of our goal to study the SHG signal, produced by GFP molecules in the PLM neurons of adequate strains. This goal now seems quite difficult. First, because these neurons, in most cases are localized close to the edges of the nematode, at a distance that may be equal or at least comparable with the resolution of our imaging setup.

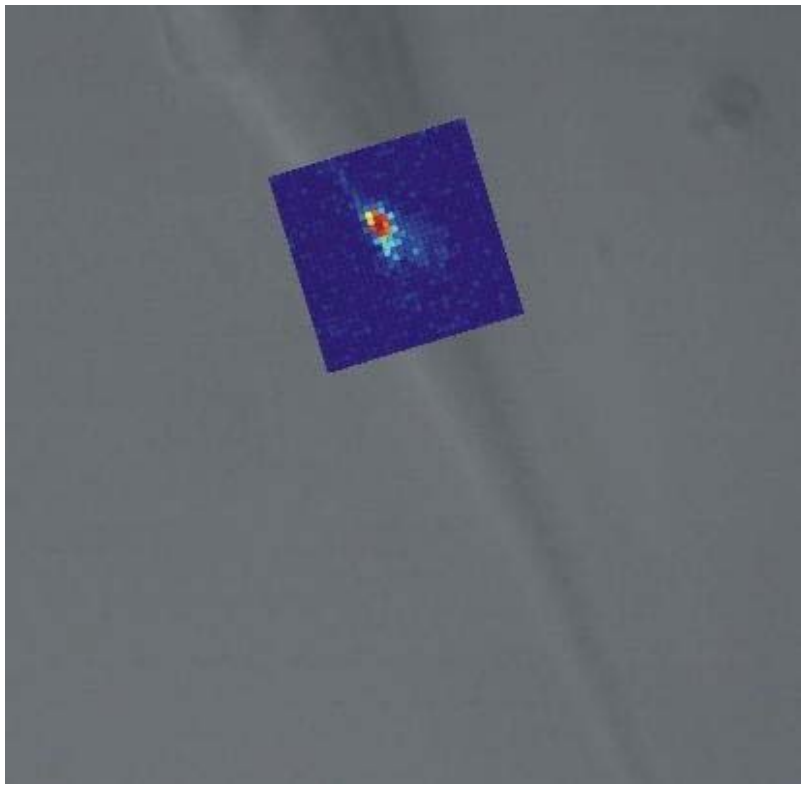

Figure 7.22 TPEF imaging of the posterior part of the N2, IS[pmec-4 GFP] strain.. The soma and part of the axon of a PLM neuron can be distinguished. The TPEF signal was detected in the forward direction, with the monochromator set at 525 nm. The scanned region has dimensions 30 x 30 μm^2.

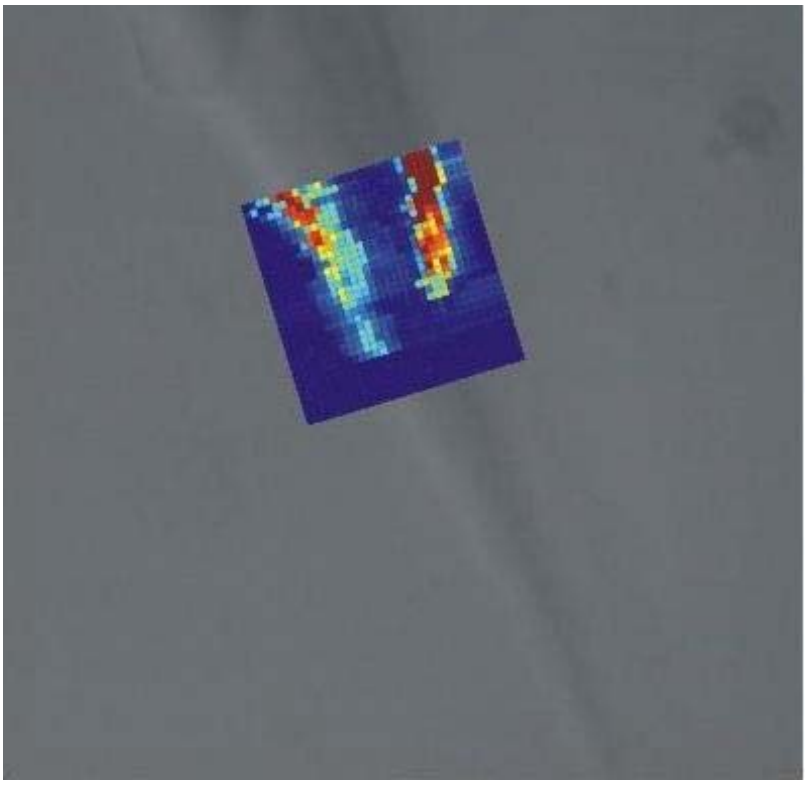

Figure 7.23 SHG imaging of the same region. The nematode is outlined, due to the endogenous SHG, arising from the body wall muscles of the worm, at both its edges. The neurons are not recognizable.

Second, looking the second picture and its data file, we realize that the SHG signal, arising from the body wall muscles is quite strong, comparable with the corresponding signal in the anterior part of the nematode. That is something we did not expect, and is not described in the literature. The standing aspect is that the body wall muscles in the posterior part are very thin and weak, thus they produce a correspondingly weak SHG signal. This aspect now seems to change, and this is the major contribution of this experiment to the whole project. *The detailed mapping of the posterior part of C. elegans by means of SHG imaging, helped us to be ready for the difficulty of the task, to separate and detect solely the exogenous SHG from the endogenous SHG signal.* This task becomes even more difficult, because we are not aware of the signal level of the exogenous SHG we should expect. Unfortunately, we do not have any idea if the exogenous SHG, arising from the GFP molecules, is weaker, comparable, or stronger than the endogenous SHG at the body edges of the nematode.

4.2 Investigation of transgenic lines with MEC-4 bound GFP molecules in touch receptor neurons

The next step in our experiments was the investigation of strains where the GFP molecules are expressed in the PLM neurons, but not with a random orientation. They are expressed in an organized way, so that they have a global orientation and thus, they have SHG efficiency. In *chapter 5*, we have already described the way in which the GFP molecules can be linked with transmembrane proteins, so that they are aligned relative to the cellular membrane. In the example of *chapter 5*, a GFP molecule was attached to the DES-2 transmembrane protein in the PVD cells of *C. elegans* [12]. In the same paper, another experiment is described. GFP molecules were attached to MEC-2 protein which is expressed in touch receptor neurons, and the SHG signal from the globally aligned GFP molecules was monitored.

For our experiments we used the transgenic line with the name N2 ex[pRF4;MEC-4::GFP]. It has been produced by the transformation of wild type animals with a plasmid construct in which the GFP molecule (S65C) is fused with the MEC-4 gene. MEC-4 is a transmembrane protein, which plays a significant role in the formation of the ion channels along the membrane of the touch receptor cells. It is actually one of the proteins which form the "funnel" of the ion channel (Figure 5.2), and for this reason is referred to as ion channel subunit. Each ion channel contains two MEC-4 proteins. The GFP molecules are attached to the MEC-4 proteins by a MEC-4 intracellular linker domain, and are oriented relative to the membrane plane. In **Figure 7.24**, the diagrammatic representation of a hypothetical

orientation of the GFP molecule is depicted. MEC-4 protein has its both ends in the cytoplasm, and penetrates twice the cellular membrane of the neuron. The GFP molecule is attached to the protein by means of an intracellular linker domain, whose length is crucial for the alignment of the GFP relative to the membrane plane. This alignment is unidentified, but the hydrophilic and the hydrophobic regions of the β barrel surface of the GFP cylinder play likely a significant role in this alignment. Even in the reported experiments [12], with the GFP attached to the DES-2 protein of the PVD cells, its alignment is ambiguous, and much more ambiguous is the corresponding alignment of GFP, when it is attached to the MEC-2 protein of the touch receptor cells [12]. However, we strongly believe that a global alignment of GFP molecules does exist in the transgenic line we use, thus giving the MEC-4 attached GFP molecules the potential for SHG.

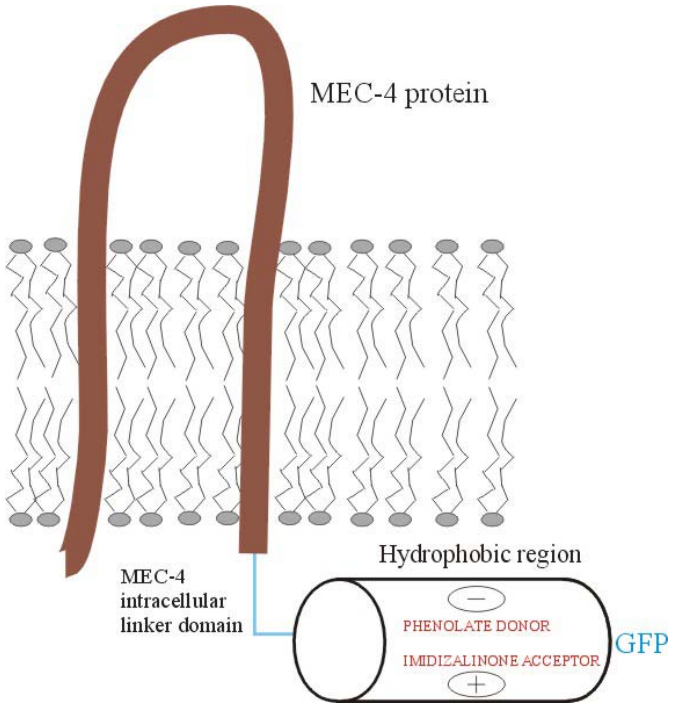

Figure 7.24 Diagrammatic representation of a hypothetical orientation of the GFP molecule attached to the ion channel subunit MEC-4. The GFP molecule is localized in the intracellular domain.

The ion channels are not isolated along the cellular membrane, but they rather form organized groups. Every group may contain about 100 ion channels, thus about 200 GFP molecules may be concentrated in a small submicron area. Therefore, we expect that the distribution of the GFP molecules is not continuous along the cellular membrane, but rather discrete, forming fluorescent “beads”.

As a consequence of the discrete distribution of the GFP molecules, and their low average concentration in the touch receptor neurons, the fluorescence signal of these neurons in the N2 ex[pRF4;MEC-4::GFP] strains is significantly lower than the corresponding fluorescence in the zdIS5 IV strains of the previous paragraph. In **Figure 7.25** a confocal image of a N2 ex[pRF4;MEC-4::GFP] is shown. The posterior part of the nematode has been imaged, and the two PLM neurons can be recognized. However, the fluorescence signal emerging from the GFP at these neurons is extremely weak. A comparison with the confocal image of Figure 7.20 is characteristic of the decrease of the fluorescence signal.

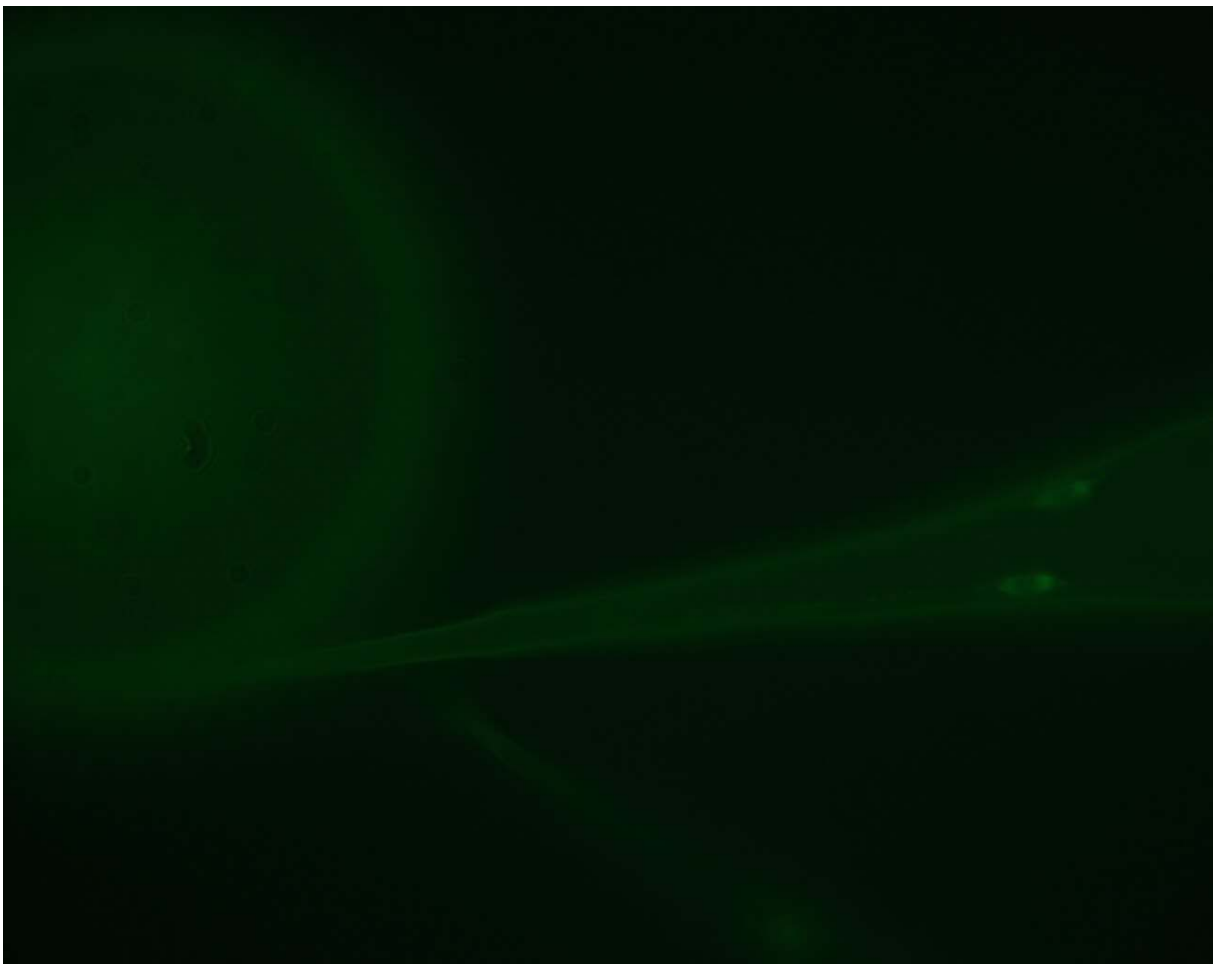

Figure 7.25 Confocal image of a N2 ex[pRF4;MEC-4::GFP] strain. GFP molecules (S65C) are fused with the MEC-4 genes in the touch receptor cells of *C. elegans*. The two PLM neurons are visible at the posterior part. Their fluorescence signal is extremely weak.

In the experiments with the specific strain, our first goal was the localization of the PLM neurons, using TPEF microscopy. Due to the weak TPEF signal we expected from the neurons of the strain, the detection of the TPEF signal was meaningful only in the backward direction. If the first goal was fulfilled, the second goal would be the investigation of the existence and the strength of the SHG signal, produced by the GFP molecules in the PLM

neurons. Unfortunately, due to the low signal levels, the localization of the neurons was not feasible with the use of our standard objective lens (Nikon, 50x, NA 0.8). Many efforts were made, but the result was always negative. We abandoned the use of this lens, and we adopted the idea to use the Edmund Scientific objective lens (100x, NA 1.25). Its use was preferable, due to its larger magnification and tighter focusing. The transverse resolution of our setup was not upgraded (1 μm in both cases), while the longitudinal was upgraded quite a lot (from 2 to 1.1 μm - see Box 7.1). The optical observation of the sample was much better, due to the larger magnification. Moreover, the nonlinear efficiency was increased due to the tighter focusing. Making a rough calculation, the fundamental beam at the focal plane decreases its diameter ($2w_\rho$) by a factor of two. That equals to an enhancement of the light intensity by a factor of four, if we accept that the losses of the fundamental beam during its propagation through the two objectives are more or less the same. The latter was confirmed experimentally (incident power on the sample 9-10 mW for both objectives). Taking now into consideration that the produced TPEF and SHG powers are proportional to the square of the intensity of the incident fundamental beam, as eq. (2.19) and eq. (3.6) indicate, we conclude that the produced TPEF and SHG signals are 16 times enhanced, compared to those when the Nikon objective is used.

Making this change in our setup, the imaging of the neuron in the posterior part of *C. elegans* was achieved. In **Figure 7.26** and **Figure 7.27** two TPEF images of the posterior part are presented. In both images the outline of the worm is recognizable, due to the autofluorescence of the worm.

In Figure 7.26, a region with dimensions 30 x 70 μm^2 has been scanned. The scanning was performed in a specific z plane, where the TPEF signal emerging from the PLM neuron was maximum. Apart from the neuron at the upper right part of the scanned region, the outline of the intestine is recognizable. The main contribution in the high level signal emerging from the inner part of the intestine, originates from the lipids (lipofuscin). The signal was detected in the backward direction, thus spectral analysis of the TPEF signal was not available. The spectral bandwidth of the intestine's fluorescence could not be investigated.

In Figure 7.27, a region with the same dimensions 30 x 70 μm^2 has been scanned. The intestine this time is not so obvious. The position of the high signal pixels is very likely to describe the fluorescence from the GFP molecules, attached to the membrane of the PLM neuron.

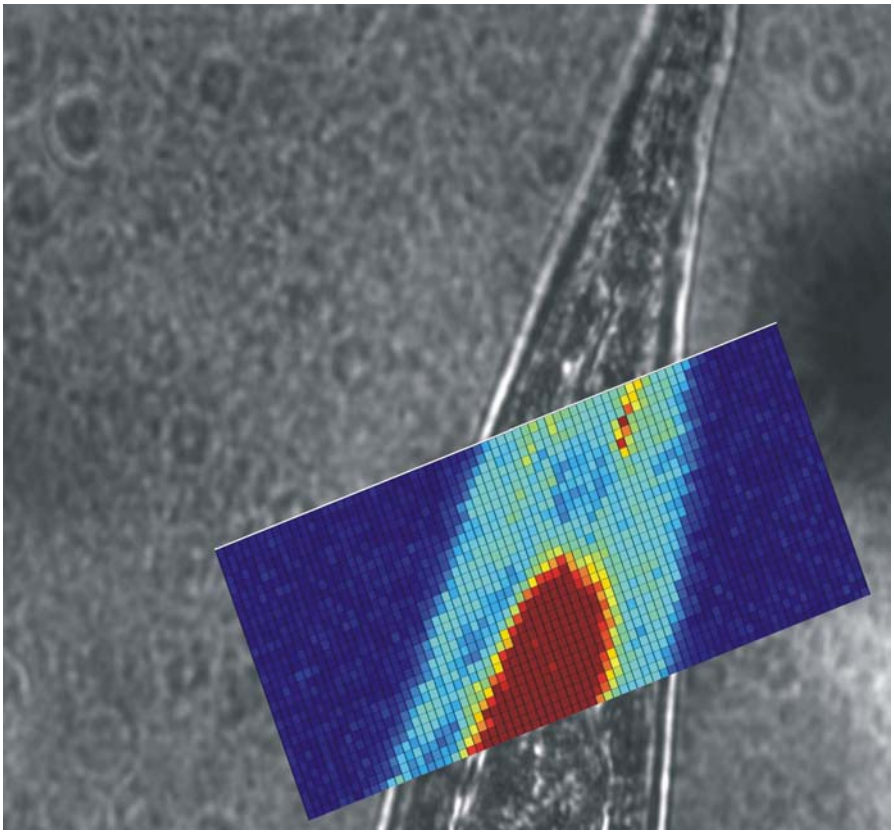

Figure 7.26 TPEF imaging of the posterior part of a N2 ex[pRF4;MEC-4::GFP] strain. The intestine of the nematode is outlined, due to the fluorescence of its lipofuscin. The PLM neuron is recognizable on the upper right corner of the scanned region. The latter has dimensions 30 x 70 μm^2.

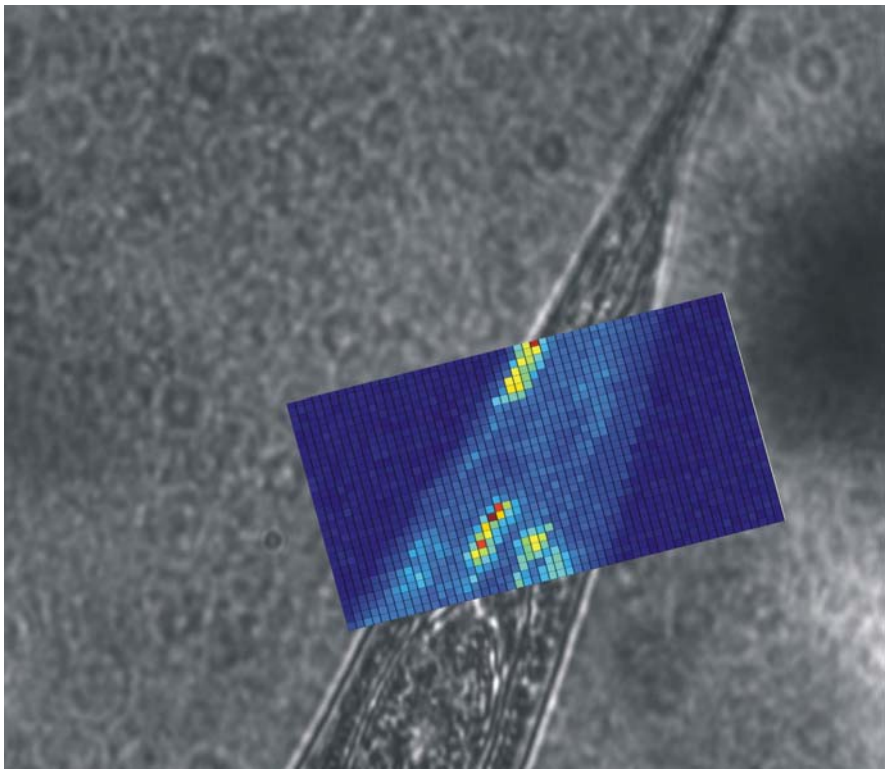

Figure 7.27 Another TPEF imaging of the posterior part of a N2 ex[pRF4;MEC-4::GFP] strain. The intestine of the nematode is not easily recognizable. The PLM neuron probably corresponds to the high intensity pixels of the image on the upper part of the scanned region. The latter has dimensions 30 x 50 μm^2.

As it has been mentioned, almost 90% of the SHG signal is lost when the Edmund Scientific (100x, NA 1.25) objective is used, in combination with the condenser lens of our microscope (NA 0.9). Hence, it was not feasible to procceed with exogenous SHG measurements, although the PLM neurons were localized.

At this point, our investigations seemed to have reached a dead-end. We investigated a *C. elegans* strain, which expresses GFP molecules at its PLM neurons in such a way that they very likely produce SHG signal. However, we have achieved to localize these neurons by TPEF, only by using an objective lens, which is totally inadequate for detection of SHG signal. On the other hand, when using the objective which is adequate for the detection of the SHG signal, the localization of the neurons by TPEF was impossible.

In the following paragraph, we present some experiments with a new developed *C. elegans* strain. The development of this strain tried to break through this problem.

4.3 Investigation of N2 ex[pRF4; pmec-7:: pat-3::GFP] strains

In order to overcome the difficulties that were described in the previous paragraph, a new strain was developed. This strain has the name N2 ex[pRF4; pmec-7:: pat-3::GFP], and the idea behind its development is the following: The GFP molecules are expressed in the touch receptor neurons, and their expression is associated with the expression of a transmembrane protein. However, this time, the expression of GFP is not driven from the mec-4 promoter, but from another touch cell specific promoter, the mec-7 promoter. MEC-7 protein is a β-tubulin, highly expressed in the touch neurons. Moreover the signal peptide of the PAT-3 membrane protein was used, in order to transfer the GFP molecules in the membrane. This chimerical molecule produces membrane bound GFP molecules, which in contrast to the MEC-4 bound GFPs, are expressed in higher levels. The MEC-7 transmembrane protein is not connected with the formation of the ion channels exclusively, and its expression is much stronger than the expression of MEC-4. In *chapter 2*, it has been already described that the TPEF signal is proportional to the number N of the fluorescent molecules, located inside the area of focus. Hence, a more dense positioning of the GFP molecules can be advantageous, in the sense that the TPEF signal will be much stronger, and thus detectable even if the fundamental beam is focused by the Nikon (50x, NA 0.8) objective lens. Preliminary investigations of this new strain, using the confocal microscope, showed indeed, that the one-photon fluorescence emerging from this strain, is much stronger than the fluorescence emerging from the N2 ex[pRF4;MEC-4::GFP] strain. Moreover, they showed that the fluorescence from this new

developed strain is not more than an order of magnitude weaker than the fluorescence from the zdIS5 IV strain, where the GFP molecules were intracellular. These preliminary investigations were positive, and confirmed us that the detection of the TPEF fluorescence from the GFP molecules at the PLM neurons will be feasible.

However, a major question arises relative to the capability of the GFP molecules in the specific strain to produce SHG signal. In order to achieve SHG, the GFP molecules should be globally oriented. Describing the arrangement shown at Figure 7.24, we already mentioned that the length of the protein intracellular linker domain, connecting the MEC-4 protein with the GFP molecule, is crucial for the proper alignment of the latter relative to the membrane plane. Regions on the GFP surface which are more hydrophobic, or have a propensity for specific charges determine the orientation of the molecule. However, when the linker is too long, the GFP molecule is placed far away from the membrane plane, and the interaction of the membrane with the GFP molecule is weak. Hence, the GFP molecules can not be globally rotated and aligned.

In the developed strain N2 ex[pRF4; pmec-7:: pat-3::GFP], the intracellular linker domain is expected to be quite longer than the corresponding linker domain in the N2 ex[pRF4;MEC-4::GFP] strain. Hence, the efficiency of the GFP for SHG at these neurons is doubtful and remains under investigation.

A lot of experiments using this strain took place, without reaching a clear conclusion. For these experiments, the presented setup with the Nikon objective lens was used. Extended regions of the posterior part of the nematode were scanned, trying to localize maxima of TPEF. The TPEF signal was detected in the backward direction, because its detection in the forward direction was not feasible. In many scannings, intensive maxima of TPEF were localized, at positions very possible for the PLM neurons to be located. The corresponding SHG signal from these pixels seemed to be negligible, when this signal was detected in the forward direction. It seemed that the PLM neuron could be localized, but the GFP molecules attached to the PAT-3 transmembrane domain, were not globally oriented, and thus, insufficient for SHG. The investigations will continue for the verification of the inability for SHG. In the 8th and last chapter of this thesis, the results we got are discussed, and the plans for the future work are presented.

1. EVALUATION OF THE DETERMINED GOALS

In *chapter 6* we determined the goals of this work. We adjusted the work plan, and we followed it in order to fulfill as many as possible of these goals. Relative to this determination we can evaluate the results of our work:

1. We succeeded in developing a reliable scanning imaging system, using the nonlinear phenomena of TPEF and SHG. The main inhibitory reason for the extended application of this innovative technique is that the the commercial nonlinear microscopes are very expensive. In the present work, a compact, reliable, flexible and inexpensive system, excluding the laser system, was developed. Although nonlinear imaging has been a laboratory standard for some labs in Europe and USA, the development of such a system is not trivial. The grade of difficulty was high, due to the lack of previous experience and know-how. We mention emphatically, that it is the first time that such a system is developed and used experimentally in an institute of Greece.
2. The reliability of the system was tested mainly by investigating various strains of the nematode *C. elegans*. We succeeded in mapping in considerable detail the anterior part of the nematode. Images that approach the state of the art in *C. elegans* nonlinear imaging were obtained. Our data agree with recently published data that support the aspect that the main SHG contribution in the anterior part arises from the actomyosin complexes of the sarcomeres of the chewing mechanism and the body wall muscles. These images confirm the high reliability of our setup.
3. The posterior part of the nematode was also successfully imaged using SHG imaging. We discovered that strong SHG signal arises also from the posterior part of the nematode, despite the lack of relative references in the known literature. The signal mainly arises from the body wall muscles, thus the nematode is outlined at its SHG imaging. Using a 3D reconstruction of sequential images at different optical sections, the posterior part of the nematode would emerge as an empty cone. The contribution of the collagen fibrils of the epidermis in the resultant SHG signal is suspected, but no further investigation for the confirmation of this suspicion was done. The high level of the SHG signal from the edges of the nematode at the posterior part, was an unpleasant surprise, because two of the six touch receptor cells, are located at this body part, in close proximity to the edges of the nematode. We found out that the endogenous SHG may overlap spatially the exogenous SHG from the GFP at these neurons, and moreover that the signal levels of the endogenous SHG are very high. Thus, the

isolation and the identification of the desirable SHG signal produced by the GFP molecules, attached to transmembrane proteins of the touch neurons, may be a very difficult task.

4. We investigated strains that express GFP molecules at the touch receptor neurons. Some of these express GFP molecules diffused inside the cytoplasm of these neurons, and some of them GFP molecules attached to specific transmembrane proteins. In all the cases, the localization of the touch neurons in the posterior part (PLM neurons) was feasible by means of TPEF scannings, even if the expression of the GFP molecules is relatively weak. However, in some cases, this localization was feasible only when using an objective lens with high NA. The use of this objective lens is incompatible with the SHG detection system in the forward direction, due to the limited NA of the standard condenser lens of our microscope.

5. We did not managed to isolate and identify SHG signal, produced by the GFP molecules, in none of the strains. For some strains that was impossible in any case. For example the GFP molecules, diffused in the touch receptor neurons cannot produce SHG signal, due to their random orientation. For the N2 ex[pRF4;MEC-4::GFP] strain, where the GFP is fused together with the MEC-4 protein, the detection system was not adequate for the collection and the detection of the SHG signal, i.e. the condenser lens has lower NA than the objective lens, hence, about 90% of the SHG signal is not detectable. Finally, for the newly developed strain N2 ex[pRF4; pmec-7:: pat-3::GFP], where the GFP is expressed under the mec-7 promoter, we found indications that the GFP molecules cannot produce SHG signal, due to the lack of a global orientation. However, more investigations should be made to ensure the inefficiency or prove the efficiency of this specific strain for exogenous SHG.

We remark that four of the goals we have set at the beginning of this work have been fulfilled. For the fulfillment of the fifth goal a new work plan should be applied.

2. FUTURE PLANS

The long-term goals of the project include the isolation of the SHG signal from the GFP molecules, attached to transmembrane proteins. This attachment is a way for the alignment of the GFP molecules, and their positioning in close proximity to the cellular membrane of the PLM neurons. The SHG signal should have a critical dependence on the membrane potential of these neurons, and thus can be a monitor of the grade of their depolarization, when mechanical stimuli apply to the nematode. In this line of investigation, the scanning of extended regions has not much to offer further. It has offered a lot till this point, because it

has revealed a great amount of information about the endogenous structures of the nematode *C. elegans*. However, the next step should be the evolution of a quick and reliable way to localize the PLM neurons in the posterior part of the nematode, to isolate and identify the SHG signal from the GFP molecules, if it is produced, and to monitor the changes of this signal, when the nematode is mechanically stimulated. The localization of the neurons only by means of TPEF scannings, seems to be time-consuming, and generally inadequate for the realization of the long-term goals.

At the present time, an effort to establish such a localization system, compatible with our microscope is on the way. A lamp and a set of filters (referred to as "UV lamp") providing blue light, that excites one-photon fluorescence from GFP molecules, is matched on our microscope. Setting adequate filters in the backward direction, the fluorescent points of the sample could be optically seen on a color CCD camera. The fundamental beam could be focused on these points directly. Small adjustments would be necessary mainly in the longitudinal z direction, and even smaller in the x-y plane, in order to reach exactly the location of the GFP molecules, and to record the maximum nonlinear signal (TPEF and if possible SHG signal). This process seems to be more quick and generally more efficient than the localization process via the TPEF signal, detected either in the backward or the forward direction. This is the only serious alteration that should be done in our setup.

Beyond this alteration, a steady effort for the development of new strains is active by Dr. N. Tavernarakis and G. Vogglis. The effort aims the development of strains that express as strongly as possible GFP molecules attached to transmembrane proteins, so that their one-photon fluorescence and TPEF is maximum. At the same time, the intracellular linker domain should be as short as possible, so that the interaction between the GFP molecules and the membrane is intense, and their global alignment feasible. Only in this case the GFP molecules can produce SHG.

Finally, a way for the mechanical stimulation of the nematodes should be established. The suggested way is the use of an optical tweezer, since experience on this technique is available in our group [107]. Using the optical tweezer, polystyrenium spheres could be trapped, brought to close proximity to the nematode, and kick it in its posterior part, stimulating it. However, the upgrading of the present setup, so that optical trapping is possible, is not trivial. An additional laser at the NIR region is necessary, and probably objective lens with high NA for the tight focusing of the trapping laser beam. The Nikon objective lens (50x, NA 0.8) is probably inefficient for optical trapping. However, the use of objective lens with high NA

demands a condenser lens with even higher NA, as it has been explained, and that can be an additional problem.

In our experiments and investigations the role of the fundamental light polarization has been excluded, although we described in the theoretical part of this thesis that it plays a significant role in both TPEF and SHG. The polarization of the fundamental beam has not been optimized, because the nonlinear signal was enough for TPEF and SHG imaging of our biological specimen. In the future, investigations of the dependence of the produced TPEF and SHG signal on the polarization of the incident light should be done. These investigations may reveal a significant enhancement of the nonlinear signals, or may provide unique information about the local organization and orientation of endogenous structures inside the tissues of the nematode. The alterations in the setup are limited only in the addition of polarizers and waveplates in the propagation path of the laser beam.

Finally, a lot of theoretical work has to be done in order to model the biological system we work on. That would help us to have a better sense of the distribution of the expressed GFP molecules at the neurons under investigation. It would also help us to be able to predict and to find the optimum conditions (intensity, polarization, illumination direction) for the stimulation and the detection of the nonlinear response of the specific biological sample.

A lot of work has left to be done for the fulfillment of the long-term goals of this project. However, the development of a reliable nonlinear imaging setup is a fact that opens the way for this fulfillment. Simultaneously, it opens parallel ways for other applications and for a more general contribution in the field of medicine, biophysics and physics.

3. OTHER APPLICATIONS

A new facility has been established in the *Institute of Electronic Structure and Laser* at FO.R.T.H. with a lot of possible applications.

At the present time, the developed nonlinear microscope is employed in two more projects. The first concerns the investigation of the SHG efficiency of collagen fibers from ox tendon. The aim of the project is the study of the temperature dependence of the destruction of its triple polypeptide helix structure, which is considered to be responsible for its high SHG efficiency. SHG and TPEF measurements of the samples will be taken by means of the developed setup, and the results will be compared with previous results obtained using a laser providing nanosecond pulses [71].

The second project concerns the photosensitizers, used in photodynamic therapy (PDT), and the specification of the locations where these photosensitizers are bound in the membrane or the cytoplasm of cancer cells. In *Appendix 2* we present our first results that show the ability of our setup to specify these locations.

Many more applications wait to be invented for the complete utilization of the developed nonlinear microscope. An new imaging system has been established, and can be proved a very helpful and powerful tool.

1. DESCRIPTION OF THE LABVIEW PROGRAM

The software we developed, is written in Labview 6.1. Its purpose is the proper motion of the three step motors, and the proper storage of the data, coming from the Lock-In Amplifier. In **Figure A.1** the front panel of the Labview program is shown.

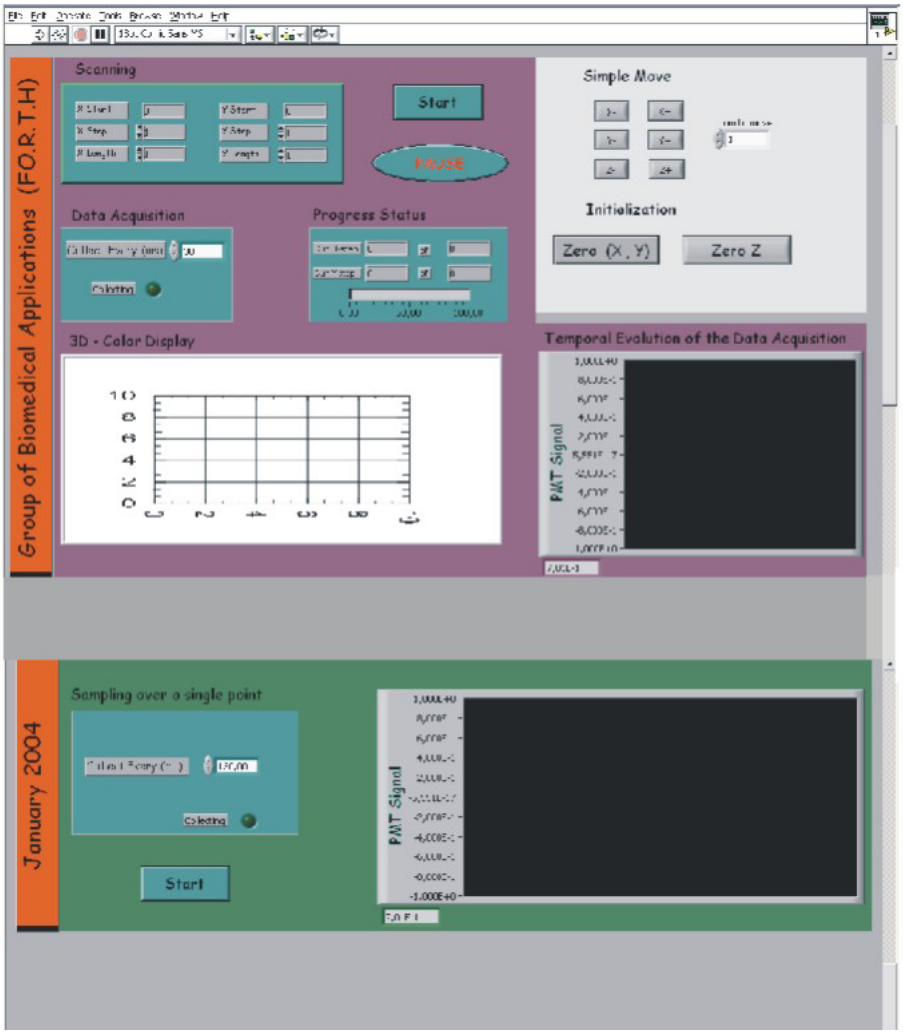

Figure A.1 Front panel of the Labview 6.1 program, developed for the step motors motion and data acquisition from the Lock-in amplifier.

The motors can work in two separate modes. They can either be simply moved independently, or they can configure with their combined motion a scanning scheme. Their simple move is necessary, for the localization of the target and the right focusing of the sample. This mode is given in the upper right part of the panel. The operator gives the distance (in μm), and he pushes the button describing the direction of the desired motion. The minimum step (or distance) is 1 μm.

If the step motors have been moved a lot, and the operator wants to have a steady spatial reference, the program gives him this opportunity. The buttons “Zero X Y” and “Zero Z” initialize the position of the stages to a pre-defined position.

If, now, the operator has focused the beam onto the desired z-plane, and wants to perform a scanning in this plane, he has to use the upper-left mode (Scanning). The scanning is performed in the x-y plane, but the program can be easily converted to include the z-axis in the scanning procedure. The operator has to give the dimensions of the area that should be scanned (X-length, Y-length). He has also to give the step-length in the two directions (X-step, Y-step). For a detailed scanning with the highest possible resolution, the step should be minimum ($1\,\mu m$). However, in many cases, we need a quick scanning of an extended area, and the step in the two directions can be set larger.

The scanning process starts when the operator pushes the “Start” button, and can be paused when he pushes the “Pause” button. In this case, a dialog box appears, and the operator can either proceed further with the scanning, or abandon it permantly.

The program is built in such a way that the x and y step motors perform a “zig-zag” scanning. Every time a stage makes a step, waits in its temporary position for a pre-defined accumulation time (“Collect every” button). The program reads the value that the Lock-in amplifier outputs at the GPIB port, and attributes this value of light intensity to the specific position of the scanned region. The stage is now free to perform the next step.

The “Progress Status” box gives information about the progress of the scanning process and the percentage of the pre-defined area that has already been scanned.

In the “Temporal Evolution of Data Acquisition” graph, the values that are received from the Lock-in amplifier, representing light intensity, appear online on the screen.

After the end of the scanning process, the resultant image is reconstructed and appear in the “3D-Color Display” graph. This is the final nonlinear image, provided by the scanning process. Each different coloring in this diagram represents a different level of values, received by the Lock-in amplifier. It is noted that the values, provided by the Lock-in amplifier, are proportional to the light intensity incident on either the PMTs. The data are stored in a file having three columns. The first column contains the x values of the scanning points, the second the y values, and the third contains the corresponding values, received from the Lock-in amplifier. The data can be further proccessed by other programs (i.e. Matlab).

A final option was added in the program. The stages can remain unmoved and the fundamental beam can be focused onto a specific point of the sample. The temporal evolution of the resultant signal can be recorded. The temporal distance of the received values is pre-

defined and regulated by setting a value in the “Collect every” box on the lower left part of the panel. The measurement starts by pushing the “Start” button. In the graph on the lower right part of the front panel, the signal is shown online, during the measurement. This option will be useful in the continue of the project for recording the SHG signal, produced by GFP molecules, bound on the membrane of touch receptor neurons in *C.elegans*. The desired alterations of this signal, when the nematode is mechanically stimulated, can be recorded in this way, providing the necessary data.

1. PHOTODYNAMIC THERAPY

Photodynamic therapy (PDT) is a technique for treating a variety of malignant and nonmalignant conditions based on the use of light-activated drugs (photosensitizers). Typically, the photosensitizer is administrated either systematically (intravenously or orally) or topically to the tissue to be treated. After allowing time for uptake of the photosensitizer to the target tissues or tissue structures, light of an appropriate wavelength to activate the drug is applied. This results in the photoproduction of one or more cytotoxic agents, leading to the intended cellular or tissue effects. For most photosensitizers used or under investigation clinically, it is likely that the main photophysical pathway is the production of singlet oxygen $^1O_2$. Singlet oxygen is an excited form of oxygen that is highly reactive with biomolecules, leading typically to oxidative damage.

The success of the PDT is based on the selective binding of the photosensitizer in the cancer cells, which leads to the destruction of these cells, leaving the healthy ones unaffected. The photosensitizer is bound to the membrane of the cancer cells, but in some cases it can penetrate into the intracellular domain. The localization of the different photosensitizers inside the cell by means of an imaging technique, can provide useful informations about their action and their effectivity. Moreover, it can be helpful in the design of more selective photosensitizers. In this line of investigation we used the developed nonlinear microscope for the localization of the photosensitizer in a specific cell line, and we compared our results with corresponding images, obtained with the confocal microscope.

2. RESULTS

The sample under investigation was the HL-60 cell line. It is a promyolocytic cell line, derived from a patient with acute promyolocytic leukimia. We used two chromophores as photosensitizers, namely merocyanine540 (MC-540) and hypericin (HP). The literature is not very clear, about the location of these photosensitizers in the cancer cells after their binding. Merocyanine540 is supposed to remain membrane bound with no potential to penetrate into the intracellular domain, whereas hypericin is supposed to have the efficiency to penetrate and be bound in other structures in the intracellular domain.

We performed TPEF scanning imaging in cells, stained both with merocyanine540 and hypericin. For these experiments the Nikon (50x, NA 0.8) objective lens was used, and the TPEF signal was detected in the backward direction. Comparative imaging by means of the

one-photon confocal microscope (facilitated to us by Dr. N. Tavernarakis and G. Vogglis) was performed, and the results were similar, proving once more the reliability of our nonlinear microscope. In **Figure A.2** and **Figure A.3**, cells stained with merocyanine540, have been imaged by means of TPEF and one-photon confocal microscope, correspondingly. Similarly, in **Figure A.4** and **Figure A.5**, cells stained with hypericin have been also comparetively imaged.

Examining Figure A.2 and Figure A.3, we note the similarity between the two images. The concentration of merocyanine540 is large in the intracellular domain, despite the established opinion that the photosensitizer does not penetrate inside the cell.

Additionally, the similarity between the images depicted in Figure A.4 and Figure A.5 is obvious. Hypericin has penetrated the cellular membrane, but two extended regions in the intracellular domain have been unstained. The interpretation of the results is not trivial. However, to our interest is the significant similarity of the images obtained with different techniques, proving the potential of our setup for reliable nonlinear imaging.

Apart from the TPEF imaging of the HL-60 cells stained with merocyanine540, SHG imaging was tried, but not achieved. The fusee for this study was the known ability of merocyanine540 for SHG when its molecules have a global orientation [108]. The failure of the SHG imaging forced us to consider two possible explanations: First, the photosensitizer penetrates the cellular membrane (as TPEF imaging indicates as well), thus having a small concentration of molecules bound on the membrane. Due to the small concentration, the SHG signal, produced by the merocyanine540 molecules, is not detectable. Second, it is very likely that the molecules that remain bound to the cellular membrane lack a global orientation, and therefore their SHG signal is negligible and not detectable.

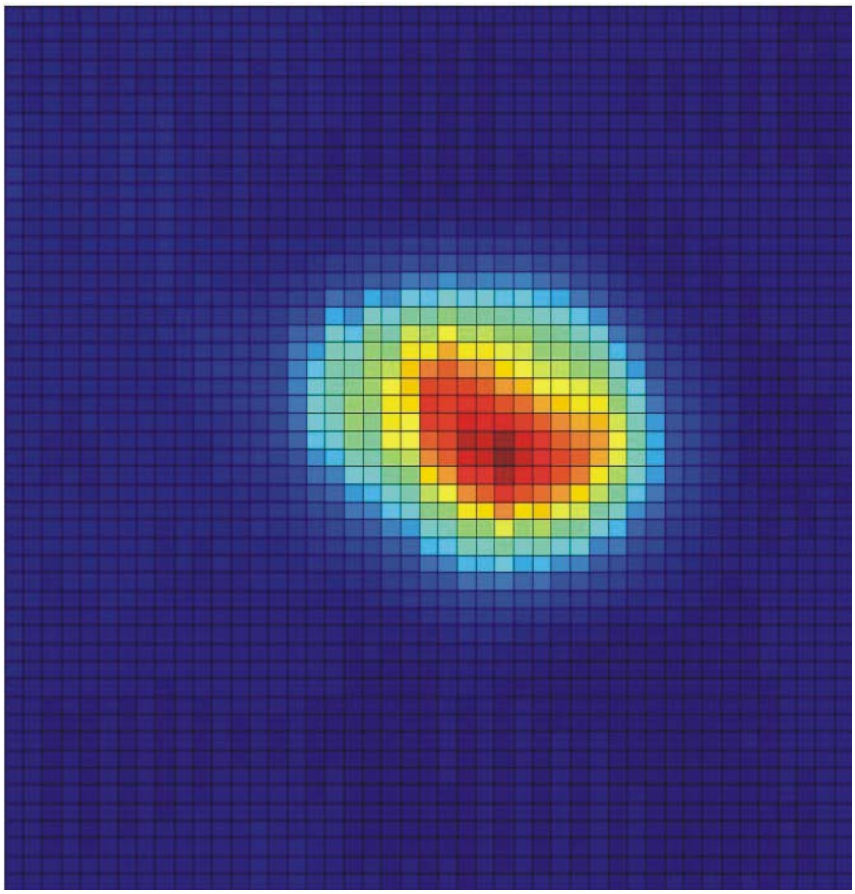

Figure A.2 TPEF scanning image of a HL-60 cell, stained with merocyanine540. The chromophore molecules penetrate the cellular membrane and are localized inside the intracellular domain. The scanning region has dimensions 50 x 45 μm^2.

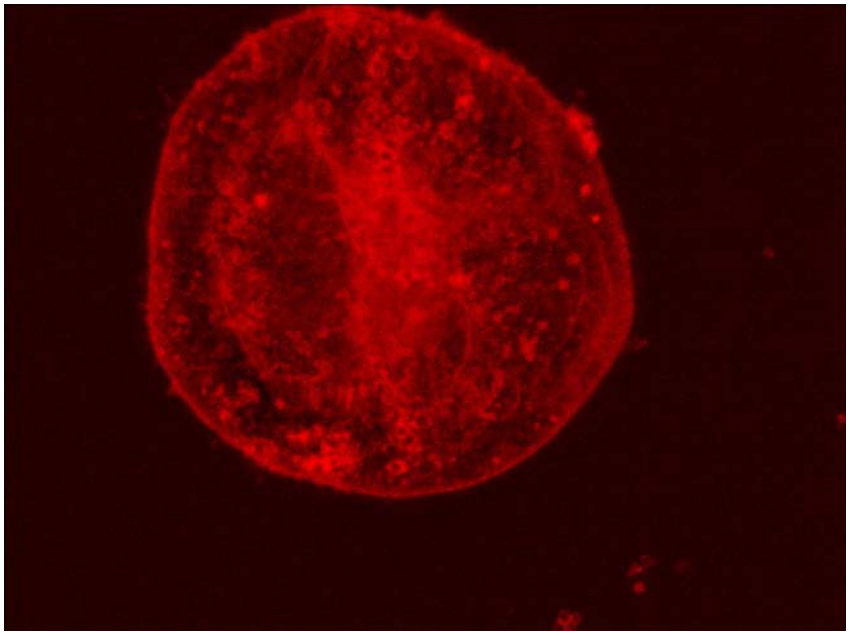

Figure A.3 One-photon confocal image of a similar cell. The characteristics of the confocal image are the same as in the TPEF image depicted in Figure A.2 (Cell diameter ~15 μm).

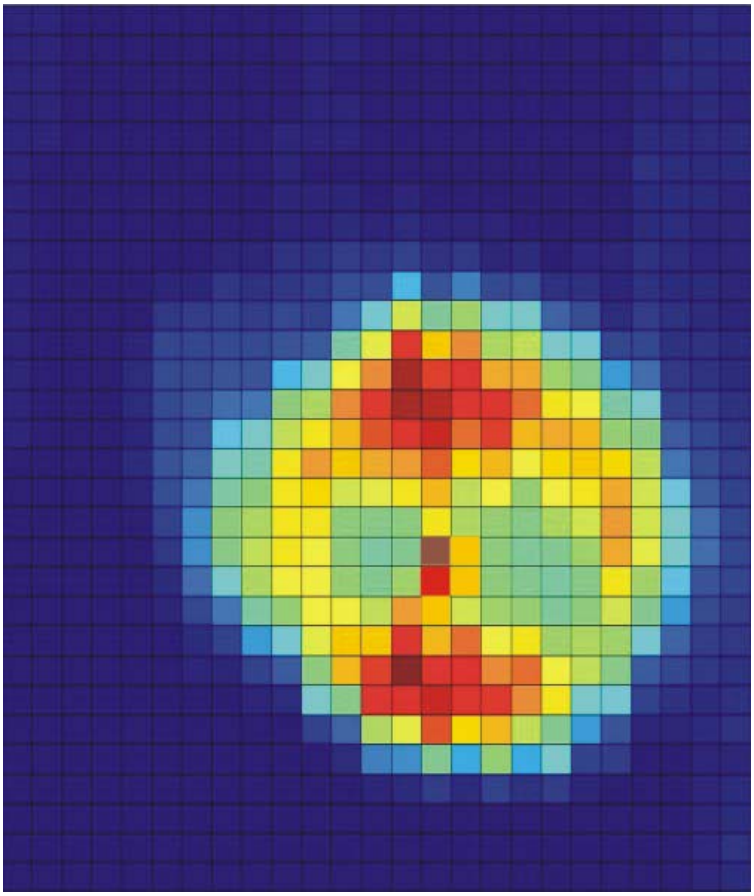

Figure A.4 TPEF scanning image of a HL-60 cell, stained with hypericin. The hypericin molecules penetrate the cellular membrane and are localized inside the intracellular domain, leaving two extended regions unstained. The scanning region has dimensions 30 x 25 μm^2.

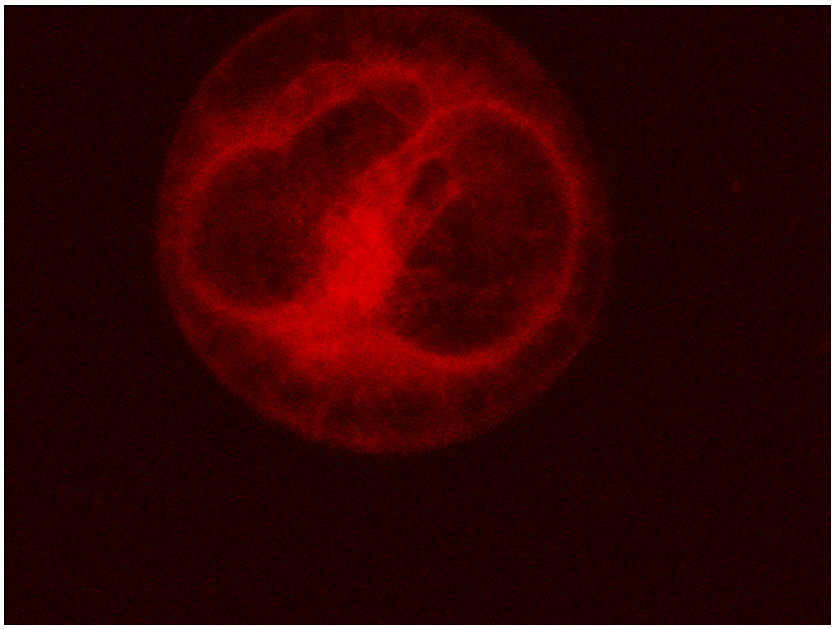

Figure A.5 One-photon confocal image of a similar cell. The characteristics of the confocal image are the same as in the TPEF image depicted in Figure A.4 (Cell diameter ~15 μm).

REFERENCES

1. W. Denk, J. H. Strickler, and W. W. Webb, "Two-photon laser scanning fluorescence microscopy", *Science* 248, **73**, (1990).

2. N. Bloembergen, "Nonlinear Optics", World Scientific, (1965).

3. Y. R. Shen, "Surface properties probed by second-harmonic and sum-frequency generation", *Nature*, **337**, 519-525, (1989).

4. Y. Huang, A. Lewis, and L.M. Lewis, "Non-linear optical properties of potential sensitive styryl dyes", *Biophys. J.*, **53**, 665-670, (1988).

5. O. Bouevitch, A. Lewis, I. Ben-Oren, J. Wuskell, and L. Loew, "Probing membrane potential with nonlinear optics", *Biophys. J.*, **65**, 672-679, (1993).

6. Ilan Ben-Oren, Gadi Peleg, Aaron Lewis, Baruch Minke, and Leslie Loew, "Infrared Nonlinear Optical Measurements of Membrane Potential in Photoreceptor Cells", *Biophysical Journal*, **71**, 1616-1620, (1996).

7. Gadi Peleg, Aaron Lewis, Michal Linial, and Leslie M. Loew, "Nonlinear optical measurement of membrane potential around single molecules at selected cellular sites", *Proc. Natl. Acad. Sci. USA*, **96**, 6700-6704, (1999).

8. Aaron Lewis, Artium Khatchatouriants, Millet Treinin, Zhongping Chen, Gadi Peleg, Noga Friedman, Oleg Bouevitch, Zvi Rothman, Leslie Loew, Mordechai Sheres, "Second-harmonic generation of biological interfaces: probing the membrane protein bacteriorhodopsin and imaging membrane potential around GFP molecules at specific sites in neuronal cells of *C. elegans*", *Chemical Physics*, **245**, 133-144, (1999).

9. Paul J. Campagnola, Mei-de Wei, Aaron Lewis, and Leslie M. Loew, "High Resolution Nonlinear Optical Imaging of Live Cells by Second Harmonic Generation", *Biophysical Journal*, **77**, 3341-3349, (1999).

10. L. Moreaux and T. Pons, V. Dambrin and M. Blanchard-Desce, J. Mertz, "Electro-optic response of second-harmonic generation membrane potential sensors", *Optics Letters*, **28**, 625-627, (2003).

11. Andrew C. Millard and Lei Jin, Aaron Lewis, Leslie M. Loew, "Direct measurement of the voltage sensitivity of second-harmonic generation from a membrane dye in patch-clamped cells", *Optics Letters*, **28**, 1221-1223, (2003).

12. Artium Khatchatouriants, Aaron Lewis, Zvi Rothman, Leslie Loew, and Millet Treinin, "GFP Is a Selective Non-Linear Optical Sensor of Electrophysiological Processes in Caenorhabditis elegans", *Biophysical Journal*, **79**, 2345-2352, (2000).

13. The *C. elegans* Sequencing Consortium, "Genome sequence of the nematode *C. elegans*: a platform for investigating biology", *Science*, 282, 2012-2018, (1998).

14. J.G. White, E. Southgate, J.N. Thomson, S. Brenner, "The structure of the nervous system of Caenorhabditis elegans", *R. Soc. London B: Biol. Sci.*, **314,** 1–340, (1996).

15. M. B. Goodman, D. H. Hall, L. Avery, and S. R. Lockery, "Active currents regulate sensitivity and dynamic range in C. elegans neurons", *Neuron.*, **20**, 763-772, (1998).

16. J. R. Lakowicz, "Principles of Fluorescence Spectroscopy", New York: Plenum Press, (1985).

17. I. D. Campbell, R. A. Dwek, "Biological Spectroscopy", Menlo Park, CA: Benjamin Cummings, (1984).

18. B. R. Masters, B. Chance In: WT Mason, ed. "Fluorescnt and Luminescent Probes for Biological Activity", London: Academic Press, (1993).

19. D. Fujimoto, *Biochem. Biophys. Res. Commun*., **76**, 1124-1129, (1977).

20. J. Blomfield, J. F. Farrar, *Cardiovasc Res*., **3**, 161-170, (1969).

21. D. P. Thornhill, *Biochem. J*., **147**, 215-219, (1975)

22. D. Eyre, M. Paz, *Annu. Rev. Biochem*., **53**, 717-748, (1984).

23. A. J. Bailey, R. G. Paul, L. Knott, "Mechanisms of maturation and ageing of collagen", *Mech. Ageing Dev*., **106**, 1-56, (1998).

24. Michael Perry, "High-Order Multiphoton Ionization of the Noble Gases", Ph.D Thesis, Lawrence Livermore National Laboratory-University of Calofornia, (1987).

25. Chris Xu and Watt W. Webb, "Measurement of two-photon excitation cross-sections of molecular fluorophores with data from 690 to 1050 nm", *J. Opt. Soc. Am. B*, **13**, 481-491, (1996).

26. J. Burris, T. J. McIlrath, "Theoretical study relating the two-photon absorption cross-section to the susceptibility controlling four-wave mixing", *J. Opt. Soc. Am. B*, **2**, 1313-1317, (1985).

27. C. C. Wang, *Phys. Rev*., **152**, 146, (1966).

28. J. Burris, Ph. D., dissertation (Department of Physics, University of Maryland, College Park, Md., 1982)

29. Y. R. Shen, "The Priciples of Nonlinear Optics", New York: John Wiley and Sons, (1984).

30. P. R. Monson and W. M. McClain, "Polarization Dependence of the Two-Photon Absorption of Tumbling Molecules with Application to Liquid 1-Chloronapthalene and Benzene", *The Journal of Chemical Physics*, **53**, 29-37, (1970).

31. W. M. McClain, "Excited State Symmetry Assignment Through Polarized Two-Photon Absorption Studies of Fluids", *The Journal of Chemical Physics*, **55**, 2789-2796, (1971).

32. Nicholas Billinton and Andrew W. Knight, ”Seeing the Wood through the Trees: A Review of Techniques for Distinguishing Green Fluorrescent Protein from Endogenous Autofluorescence”, *Analytical Biochemistry*, **291**, 175-197, (2001).

33. R. Swaminathan, C. P. Hoang and A. S. Verkman, *Biophys. J.*, **72**, 1900-1907, (1997).

34. P. F. Curley, A. I. Ferguson, J. G. White and W. B. Amos, “Application of a femtosecond self-sustaining mode-locked Ti:sapphire laser to the field of laser scanning confocal microscopy”, *Opt. Quantum Electr*., **24**, 851-859, (1992).

35. L. Parma and N. Omenetto, “Fluorescence behavior of 7-hydroxycoumarine excited by one-photon and two-photonabsorption by means of a tunable laser”, *Chem. Phys. Lett*., **54**, 544-546, (1978).

36. M. Minsky, Microscopy Apparatus, USA, (1961).

37. B. R. Masters, “Selected papers on confocal microscopy”, Bellingham: SPIE, (1996).

38. Mohler W. A. , Simske J. S., Williams-Masson E. M., Hardin J. D., and White J. G., “Dynamics and ultrastructure of developmental cell fusions in the Caenorhabditis elegans hypodermis”, *Cur. Biol*., **8**, 1087-1090, (1998).

39. W. A. Mohler, J. G. White, “Stereo-4-D reconstruction and animation from living fluorescent specimens”, *Biotechniques*, **24**, 1006-1010, (1998).

40. D. R. Sandison, R. M. Williams, K. S. Wells, J. Strickler, W. W. Webb, “Quantitative fluorescence confocal laser scanning microscopy”, In: HBCM, 39-53, (1995).

41. S. M. Keyse, R. M. Tyrell, “Induction of the heme oxygenase gene in human skin fibroblasts by hydrogen peroxide and UVA (365 nm) radiation: evidence for the involvement of the hydroxyl radical”, *Carcinogenesis*, **11**, 787-791, (1990).

42. R. M. Tyrell, S. M. Keyse, “New trends in photobiology. The interaction of UVA radiation with cultured cells”, *J. Photochem. Photobiol. B*, **4**, 349-361, (1990).

43. Philip E. Hockberger, Timothy A. Skimina, Victoria E. Centonze, Colleen Lavin, Su Chu, Soheil Dadras, Janardan K. Reddy, and John G. White, “Activation of flavin-containing oxidases underlies light-induced production of H_2O_2 in mammalian cells”, *Proc. Natl. Acad. Sci. USA*, **96**, 6255-6260, (1999).

44. B. Kiedraszuk, H. Malak, I. Gryczynski, P. Callis, J. R. Lakowicz, “Fluorescence of reduced nicotinamides using one- and two-photon excitation”, *Biophys. Chem*., **62**, 1-13, (1996).

45. R. Yuste, W. Denk, “Dentritic spines as basic functional units of neuronal integration”, *Nature*, **375**, 682-684, (1995).

46. K. Svoboda, D. W. Denk, W. Denk, “Direct measurement of coupling between dendritic spines and shafts”, *Science*, **272**, 716-719, (1996).

47. M. Maletic-Savatic, R. Malinow, K. Svoboda, ”Rapid dendritic morphogenesis in CA 1 hippocampal dendrites induced by synaptic activity”, *Science*, **283**, 1923-1927, (1999).

48. F. Engert, T. Bonhoeffer, “Dendritic spine changes associated with hippocampal long-term synaptic plasticity”, *Nature*, **399**, 66-70, (1999).

49. David Kleinfeld, Partha P. Mitra, Fritjof Helmchen, and Winfried Denk, “Fluctuations and stimulus-induced changes in blood flow observed in individual capillaries in layers 2 through 4 of rat neocortex”, *Proc. Natl. Acad. Sci. USA*, **95**, 15741-15746, (1998).

50. R. H. Christie, B. J. Bacskai, W. R. Zipfel, R. M. Williams, S. T. Kajdasz, W. W. Webb, and B. T. Hyman, “Growth arrest of individual senile plaques in a model of Alzheimer’s disease observed by in vivo multiphoton microscopy”, *J. Neurosci*., **21**, 858-864, (2001).

51. B. J. Bacskai, S. T. Kajdasz, R. H. Christie, C. Carter, D. Games, P. Seubert, D. Schenk, B. T. Hyman, “Imaging of amyloid-beta deposits in brains of living mice permits direct observation of clearance of plaques with immunotherapy”, *Nat. Med*., **7**, 369-372, (2001).

52. D. A. Kleinman, “Nonlinear dielectric polarization in optical media”, *Phys. Rev.*, **126**, 1977-1979, (1962).

53. R. Hellwarth, and P. Christensen, “Nonlinear optical microscopic examination of structure in polycrystalline ZnSe”, *Opt. Comm.*, **12**, 318-322, (1974).

54. S. Roth, and I. Freund, “Second-harmonic generation in collagen”, *J. Chem. Phys*., **70**, 1637-1643, (1979).

55. L. Moreaux, O. Sandre, M. Blanchard-Desce, and J. Mertz, “Membrane imaging by simultaneous second-harmonic generation and two-photon microscopy”, *Opt. Lett*., **25**, 320-322, (2000).

56. P. N. Butcher and D. Cotter, “The elements of nonlinear optics”, 9: Cambridge University Press, (1990).

57. M. Born and E. Wolf, “Principles of Optics”, 6th ed: Cambridge University Press, (1980).

58. W. Liptay, “Excited States”, 1, N.Y.: Academic Press, (1974).

59. L. Moreaux, O. Sandre, J. Mertz, “Membrane imaging by second-harmonic generation microscopy”, *J. Opt. Soc. Am. B*., **17**, 1685-1694, (2000).

60. J. I. Dadap, Shan, K. B. Eisenthal, and T. F. Heinz, “Second-harmonic Rayleigh scattering from a sphere of centrosymmetric material”, *Phys. Rev. Lett*., **83**, 4045-4048, (1999).

61. J. D. Krauss, “Antennas”, New York: McGraw Hill, (1950).

62. R. Gauderon, P. B. Lukins, C.J.R. Sheppard, “Optimization of second-harmonic generation microscopy”, *Micron*, **32**, 691-700, (2001).

63. M. Born and E. Wolf, “Principles of Optics”, 6th ed.: Pergamon, Oxford, (1993).

64. B.-M. Kim, J. Eichler, and L. B. Da Silva, “Frequency doubling of ultrashort laser pulses in biological tissue”, *Appl. Opt*., **38**, 7145-7150, (1999).

65. J. L. Oudar, “Optical nonlinearities of conjugated molecules. Stilbene derivatives and highly polar aromatic compounds”, *J. Chem. Phys*., **67**, 446-457, (1977).

66. M. Blanchard-Desce, “Two-form two-state analysis of polarizabilities of push-pull molecules”, *J. Opt. Soc. Am. B*, **15**, 302-307, (1998).

67. J.-L. Oudar and D. S. Chemla, “Hyperpolarizabilities of the nitroanilines and their relations to the excited state dipole moment”, *J. Chem. Phys*., **66**, 2664-2668 , (1977).

68. D. S. Chemla and J. Zyss, “Nonlinear Optical Properties of Organic Molecules and Crystalls”, 1, New York: Academic Press, (1984).

69. J. Mertz, “Second harmonic generation microscopy”, in: Multi-photon laser scanning microscopy, Ed. A. Dixon, BIOS Press, Oxford, in press.

70. J. Mertz, L. Moreaux, “Second-harmonic generation by focused excitation of inhomogeneously distributed scatterers”, *Optics Comm*., **196**, 325-330, (2001).

71. E. Georgiou, T. Theodossiou, V. Hovhannisva, K. Politopoulos, G. S. Rapti, D. Yova, “Second and third optical harmonic generation in type I collagen, by nanosecond laser irradiation, over a broad spectral region”, *Opt. Commun.*, **176**, 253-260, (2000).

72. S. Roth, I. Freund, “Optical second-harmonic scattering in rat-tail tendon”, *Biopolymers*, **20**, 1271-1290, (1981).

73. Guy Cox, Eleanor Kable, Allan Jones, Ian Fraser, Frank Maconi, and Mark D. Gorrel, “3-Dimensional imaging of collagen using second harmonic generation”, *J. of Struct. Biol*., **141**, 53-62, (2003).

74. William Mohler, Andrew C. Millard, and J. Campagnola, “Second harmonic generation imaging of endogenous structural proteins”, *Methods*, **29**, 97-109, (2003).

75. Paul J. Campagnola, Andrew C. Millard, Mark Terasaki, Pamela E. Hoppe, Christian J. Malone, and William A. Mohler, “Three-Dimensional High-Resolution Second-Harmonic Generation Imaging of Endogenous Structural Proteins in Biological Tissues”, *Biophys. J.*, **81**, 493-508, (2002).

76. L. Cassimeris, S. Inoue, E. D. Salmon, Cell Motil, “Microtubule dynamics in the chromosomal spindle fiber: analysis by fluorescence and high resolution polarization microscopy”, *Cell Motil, Cytoskeleton*, **10**, 185-196, (1988).

77. Y. Guo, P. P. Ho, H. Savage, D. Harris, P. Sacks, S. Schantz, F. Liu, N. Zhadin, and R. R. Alfano, “Second-harmonic tomography of tissues, *Opt. Lett*., **22**, 1323-1325, (1997).

78. Edward Brown, Trevor Mckee, Emmanuelle diTomaso, Alain Pluen, Brian Seed, Yves Boucher, and Rakesh K. Jain, “Dynamic imaging of collagen and its modulation in tumors in vivo using second-harmonic generation”, *Nature Medicine*, **9**, 796-801, (2003).

79. A. Srivastava and K. B. Eisenthal, "Kinetics of molecular transport across a liposome bilayer", *Chem. Phys. Lett*., **292**, 345-351, (1998).

80. L. Moreaux, O. Sandre, S. Charpak, M. Blanchard-Desce, and J. Mertz, "Coherent Scattering in Multi-Harmonic Light Microscopy", *Biophys. J*., **80**, 1568-1574, (2001).

81. O. Shimomura, F. H. Johnson, Y.Saiga, "Extraction, purification and properties of aequorin, a bioluminescent protein from the luminous hydromedusan, Aequorea", *J. Cell Comp. Physiol.*, **59**, 223-239, (1962).

82. Y. P. Wu, E. McMahon, M. R. Kraine, R. Tisch, A. Meyers, J. Frelinger, G.K. Matsushima, K. Suzuki, " Distribution and characterization of GFP(+) donor hematogenous cells in Twitcher mice after bone marrow transplantation", *Am. J. Pathol*., **156**, 1849-1854, (2000).

83. B. M. Tam, O. L. Moritz, L. B. Hurd, D. S. Papermaster, "Identification of an outer segment targeting signal in the COOH terminus of rhodopsin using transgenic Xenopus laevis", *J. Cell. Biol*., **151**, 1369-1380, (2000).

84. A. Amsterdam, S. Lin, N. Hopkins, "The Aequorea victoria green fluorescent protein can be used as a reporter in live zebrafish embryos", *Dev. Biol*., **171**, 123-129, (1995).

85. R. Rizzuto, M. Brini, P. Pizzo, M. Murgia, T. Pozzan, "Chimeric green fluorescent protein as a tool for visualizing subcellular organelles in living cells", *Curr. Biol*., **5**, 635-642, (1995).

86. M. Chalfie, Y. Tu, G. Euskirchen, W. W. Ward, D. C. Prasher, "Green fluorescent protein as a marker for gene expression", *Science*, **263**, 802-805, (1994).

87. J. M. Mullaney, R. B. Thompson, Z. Gryczynski, L. W. Black, "Green fluorescent protein as a probe of rotational mobility within bacteriophage T4", *J. Virol. Meth*., **88**, 35-40, (2000).

88. J. Chen, Y. Watanabe, N. Sako, K. Ohshima, Y. Okada, "Complete nucleotide sequence and synthesis of infectious in vitro transcripts from a full-length cDNA clone of a rakkyo strain of tobacco mosaic virus", *Arch. Virol*., **141**, 885-900, (1996).

89. C. M. Coburn, C. I. Bargmann, "A putative cyclic nucleotide-gated channel is required for sensory development and function in C. elegans", *Neuron*, **17**, 695-706, (1996).

90. D. C. Prasher, V. K. Eckenrode, W. W.Ward, F. G. Prendergast, M. J. Cormier, "Primary structure of the *Aequorea victoria* green fluorescent protein", *Gene*, **111**, 229-233, (1992).

91. M. Chalfie, *Photochem. Photobiol*. **62**, 651-656, (1995).

92. F. Yang, L. G. Moss, G. N. Jr. Phillips, *Nature Biotech*., **14**, 1246-1251, (1996).

93. Mats Ormö, Andrew B. Cubitt, Karen Kallio, Larry A. Gross, Roger Y. Tsien, and S. James Remington, *Science*, **273**, 1392-1395, (1996).

94. Roger Y. Tsien, "The Green Fluorescent Protein", *Annu. Rev. Biochem*., **67**, 509-544, (1998).

95. P. R. Dragsten, and W. W. Webb, “Mechanism of the membrane potential sensitivity of the fluorescent membrane probe merocyanine 540”, *Biochemistry*, **17**, 5228-5240, (1978).

96. P. J. Sims, A. S. Waggoner, C.-H. Wang, and J. F. Hoffman, “Studies on the mechanism by which cyanine dyes measure membrane potential in red blood cells and phosphatidylcholinevesicles”, *Biochemistry*, **13**, 3315-3330, (1974).

97. E. F. Fluhler, V. G. Burnham, and L. M. Loew, “Spectra, membrane binding, and potentiometric responses of new charge shift probes”, *Biochemistry*, **24**, 5749-5755, (1985).

98. L. M. Loew, G. W. Bonneville, and J. Surow, “Charge-shift optical probes of membrane potential. Theory”, *Biochemistry*, **17**, 4065-4071, (1978).

99. D. S. Chemla, and J. Zyss, “Nonlinear Optical Properties of Organic Molecules and Crystals”, **1**, New York: Academic Press, (1984).

100. J. L. Oudar, “Optical nonlinearities of conjugated molecules. Stilbene derivatives and highly polar aromatic compounds”, *J. Chem. Phys*., **67**, 446-457, (1977).

101. J.E. Sulston, E. Schierenberg, J.G. White, J.N. Thomson, “The embryonic cell lineage of the nematode Caenorhabditis elegans”, *Dev. Biol*., **100,** 64–119, (1983).

102. A. Fire, S. Xu, M. K. Montgomery, S. A. Kostas, S. E. Driver, C. Mello, “Potent and specific genetic interference by double-stranded RNA in Caenorhabditis elegans”, *Nature,* **391**, 806–811, (1998).

103. C.C. Mello, J.M. Kramer, D. Stinchcomb, V. Ambros, “Efficient gene transfer in C. elegans: extrachromosomal maintenance and integration of transforming sequences”, *EMBO J*., **10**, 3959–3970, (1991).

104. J. Mertz, “Molecular photodynamics involved in multi-photon excitation fluorescence microscopy”, *Eur. Phys. J. D*, **3**, 53-66, (1998).

105. S. Brenner, “The genetics of Caenorhabditis elegans”, *Genetics,* **77**, 71-94, (1974).

106. Paul J. Campagnola and Leslie M. Loew, “Second-harmonic imaging microscopy for visualizing biomolecular arrays in cells, tissues and organisms”, *Nature Biotechnology*, **21**, 1356-1360, (2003).

107. Βασιλάκης Γεώργιος, “Οπτική Παγίδευση σωματιδίων και βιολογικού υλικού και φασματοσκοπία φθορισμού με LASER”, Διπλωματική εργασία, Πανεπιστήμιο Κρήτης-Τμήμα Φυσικής, (2000).

108. Yoshiaki Uesu, Ryuhei Nakai, Noritaka Kato, Carole Menoret, Jean-Michel Kiat, Mitsuru Itoh, Miho Narahashi and Toru Kyomen, “SHG Microscopic Studies on Low Temperature Phase Transitions of $SrTi_{16}O_3$ and $SrTi_{18}O_3$”, *Ferroelectrics*, **285**, 19-26, (2003).